Stochastic Resilience-Oriented Smart Power Distribution System Planning and Operation Against Natural Disasters

by

Wenlong Shi

A thesis submitted in partial fulfillment of the requirements for the degree of

Doctor of Philosophy
in
Energy Systems

Department of Electrical & Computer Engineering

University of Alberta

Abstract

Climate change has become an urgent global concern in the 21st century. Such environmental variation has led to an increasing occurrence of natural disasters. For example, the continuing rises in global temperatures can bring about severe storms and wildfires. Consequently, electrical infrastructures can be damaged, inducing large-scale blackouts and considerable economic losses. Therefore, power grid resilience against natural disasters has become a hot topic in both industry and academia. Benefiting from smart power distribution systems (PDSs), advanced techniques such as distributed generation and distributed automation can enhance power grid resilience effectively. However, one of the greatest challenges is how to efficiently utilize the emerging smart devices in a resilience-oriented manner considering the randomness of natural disasters. Therefore, in this thesis, the stochastic resilience-oriented smart PDS planning and operation against natural disasters is investigated. Four main research topics are studied.

Firstly, the stochastic planning for PDS resilience enhancement against earthquakes is investigated. Specifically, the portfolio of resilient measures including hardening distribution lines (DLs), and investing in Mobile Emergency Generators (MEGs) and Mobile Energy Storage Systems (MESSs) are studied in a stochastic environment. A spatial seismic damage model is developed to geographically characterize the random damages of earthquakes. The stochastic PDS planning problem is formulated as a risk-averse two-stage stochastic bi-level programming problem. The upper-level minimizes the total investment cost and the expected interruption cost. The lower-level minimizes the expected loss of load through MEG and MESS coordination, including co-allocation and energy exchange. To solve this problem, a

decomposition method is proposed to break up the problem into two separate subproblems to speed up the computation. Case studies based on IEEE 37-Node and 123-Node Test Feeders demonstrate that the co-optimization of DL hardening and MEG and MESS investment considering MEG and MESS coordination including co-allocation and energy exchange is necessary. It can enhance the PDS resilience against earthquakes in a cost-effective manner.

Some types of natural disasters can impose destructive impact over a period of time, resulting in post-restoration failures. In the second work, the resilient restoration against uncertain multi-shocks of earthquakes and post-restoration failures is investigated. A data-driven PDS resilience enhancement strategy is proposed against multi-shocks of earthquakes considering the underlying uncertainties. A resistibility index (RI) is developed based on hierarchical hidden Markov models (HHMMs) for stochastic resilience evaluation. The historical earthquake data are incorporated into the HHMM as observed information of multi-shocks of earthquakes. Based on the RI metric, the problems of pre-positioning and reallocation of MEGs are formulated as mixed-integer programming problems. The problem of repair scheduling is formulated as an adaptive two-stage multi-period stochastic programming problem, for which a revision period is introduced to allow the decisions to adapt to the underlying uncertainties after the revision. Also, to reduce the computational complexity, an iterative algorithm is presented based on linear relaxation. Case studies based on the modified IEEE 123-Node Test Feeder and historical earthquake data of the 1994 Northridge earthquake demonstrate the efficiency of the proposed strategy.

The existing MG formation approaches based on the Distflow model always demand MG roots and their corresponding topologies. This can result in an increased number of variables and constraints in the optimization problem. In the third work, the dynamic microgrid (MG) formation considering large-scale deployment of mobile energy resources (MERs) is studied. Specifically, an adaptive linearized Distflow model is proposed based on the single commodity flow model in graph theory. The active and reactive powers are represented as commodities, which are sent from one node to each of its adjacent nodes in a graph. Accordingly, the power flow and nodal voltage calculation based on the commodity flow only requires adjacent node information of the original topology rather than various MG topologies caused by the dynamic deployment of MERs. Moreover, the dynamic MG formation problem is formulated as a mixed-integer nonlinear programming problem by incorporating the adaptive LinDistflow model as constraints. A linearization technique is proposed based on propositional logic constraints. The effectiveness of the proposed dynamic MG formation approach is evaluated based on the IEEE 37-Node, IEEE 123-Node and IEEE 8500-Node Test Feeders. The evaluation results also indicate that the large-scale MER deployment can lead to a lower average total load shed.

Modern power systems are undergoing a paradigm shift from traditional grids towards smart grids. New challenges arise in terms of grid resilience, because natural disasters can cause damages to both cyber and physical systems. In the forth work, we propose a stochastic sequential restoration scheme for cyber-physical power distribution systems (CPDSs) considering resilience. The sequential restoration problem is formulated as an uncertain Markov decision process (UMDP) with hurricanes incorporated as natural disasters. Different wind velocities and directions are considered as hurricane scenarios, which are used to obtain the fragility of DLs. The fragility functions are further used for the derivation of uncertain state transition functions of the UMDP. The minimax regret optimization considering the sample weights of UMDP is presented. The robust sequential actions are determined, such that the loads can be restored in a timely manner. To improve computational efficiency, a minimax regret policy iteration algorithm is presented based on the regret Bellman equation. Case studies are conducted based on the IEEE 123-Node Test Feeder and historical data of Hurricane Bonnie to demonstrate the effectiveness of the proposed scheme.

Preface

The material presented in this thesis is based on original works by Wenlong Shi. As detailed in the following, material from some chapters of this thesis has been published as journal articles under the supervision of Dr. Hao Liang in concept formation and by providing comments and corrections to the article manuscript.

Chapter 2 includes the results published in the following paper:

- W. Shi, H. Liang, and M. Bittner, "Stochastic planning for power distribution system resilience enhancement against earthquakes considering mobile energy resources," *IEEE Transactions on Sustainable Energy*, vol. 15, no. 1, pp. 414-428, Jan. 2024.

Chapter 3 includes the results published in the following paper:

- W. Shi, H. Liang, and M. Bittner, "Data-driven resilience enhancement for power distribution systems against multishocks of earthquakes," *IEEE Transactions on Industrial Informatics*, 2024, to appear, DOI: 10.1109/TII.2024.3359437.

Chapter 4 includes the results published in the following paper:

- W. Shi, H. Liang, and M. Bittner, "Dynamic microgrid formation for resilient distribution systems considering large-scale deployment of mobile energy resources," *Applied Energy*, 2024, to appear, DOI: 10.1016/j.apenergy.2024.122978.

Chapter 5 includes the results in the following paper that has been submitted:

- W. Shi, H. Liang, and M. Bittner, "Stochastic sequential restoration for resilient cyber-physical power distribution systems," submitted to *IEEE Transactions on Industrial Informatics*, 2024, under 2^{nd} round review.

Acknowledgments

I extend my deepest gratitude to my supervisor, *Prof. Hao Liang* for his unwavering support, invaluable guidance, and boundless patience throughout my research at the University of Alberta. His expertise, encouragement, and constructive criticism have been instrumental in shaping my ideas and pushing me to strive for excellence.

I would like to express my sincere gratitude to the members of my doctoral committee for their insightful feedback and comments at various stages of my research. Their rigorous examination have undoubtedly strengthened the quality of this thesis. I am immensely grateful to my colleagues and friends at the Intelligent Energy Systems Lab. The collaborative atmosphere and stimulating discussions within our research group have helped me a lot during my PhD journey.

In addition, I would like to express my great gratitude to my wife and my daughter for their constant encouragement and support that have sustained me during moments of doubt and difficulty.

Table of Contents

List of Tables

List of Figures

List of Acronyms

AMI Advanced Metering Infrastructure

CL Critical Load

CPDS Cyber-Physical Distribution System

DER Distributed Energy Resource

DG Distributed Generator

DL Distribution Line

ESS Energy Storage System

HHMM Hierarchical Hidden Markov Model

IED Intelligent Electronic Device

MDP Markov Decision Process

MEG Mobile Emergency Generator

MER Mobile Energy Resource

MESS Mobile Energy Storage System

MG Microgrid

MILP Mixed Integer Linear Programming

OPGW Optical Fiber Composite Overhead Ground Wire

PDS Power Distribution System

PGA Peak Ground Acceleration

RCS Remotely Controlled Switch

SOC State of charge

UMDP Uncertain Markov Decision Process

Nomenclature

Chapter 2

$\Delta S_n^{pt}(\omega)$ Active load shed of node n at time t.

η^{ch} Charging efficiency of MESSs.

η^{dis} Discharging efficiency of MESSs.

ψ_{sd}^{ω} Binary, 1 if the d_{th} type of MESS is selected to be the s_{th} MESS, 0 otherwise.

$\boldsymbol{c}_e$ Vectors of various types of MESSs cost.

$\boldsymbol{c}_g$ Vectors of various types of MEGs cost.

c_h Cost of unit length of hardened DLs.

c_s Load shed cost per kWh.

D_n^{pt} Active load demand of node n at t.

D_n^{qt} Reactive load demand of node n at t.

$E_e^{pt\omega}$ Total MESS injected or consumed power at MESS connection node e.

$\hat{E}_{se}^{pt\omega}$ Discharging power of the s_{th} MESS at node e under scenario ω at time t.

$\check{E}_{se}^{pt\omega}$ Charging power of the s_{th} MESS at node e under scenario ω at time t.

$\widetilde{E}_s^{t\omega}$ State of charge of the s_{th} MESS.

$G_{n\omega}^{pt}$ Active power generated at node n under scenario ω at time t.

$G_{n\omega}^{qt}$ Reactive power generated at node n under scenario ω at time t.

n_t Number of DLs in the distribution system.

N_m^e Maximum numbers of MESS that a connection node can accommodate.

N_m^g Maximum numbers of MEG that a connection node can accommodate.

p_n Load weight of node n.

r_{mn} Resistance of DL (m, n).

$rp_{mn}^{t\omega}$ Binary parameter, 1 if damaged line (m, n) is repaired at time t under scenario ω, 0 otherwise.

x_{mn} Reactance of DL (m, n).

$v_{nk}^{t\omega}$ Binary, 1 if node n joins the microgrid whose root node is at MEG connection node k.

Chapter 3

σ_z Standard deviation of PGA of PDSs under damage state z.

$\mathcal{T}(n)$ The subtree rooted at scenario node n.

Ω_t Set of nodes in period t.

c_e The cost of the e_{th} type of MEG that can be invested.

d_{cg}^n Binary, 1 if path from g to c is damaged in scenario node n.

F_{ig}^p Real in-flow power of node i powered by MEG candidate location g.

F_{ig}^q Reactive in-flow power of node i powered by MEG candidate location g.

N_c Total number of CLs.

N_D The number of collapsed restoration paths.

$N_{\mathcal{P}}^c$ Initial number of restoration path of CL c.

p_{cg} Binary, 1 if restoration path from MEG location g to CL c path is selected.

P_M^e Real capacity of e_{th} candidate MEG.

P_i Real power demand at node i.

Q_M^e Reactive capacity of e_{th} candidate MEG.

Q_i Reactive power demand at node i.

r_{ij} Resistance of DL (i, j).

s_e Binary, 1 if the e_{th} type of MEG is invested.

$s(n)$ Set of nodes from the root to scenario node n.

v_{ge} Binary, 1 if the e_{th} type of MEG is selected to be deployed at MEG candidate location g.

V_{ig} Nodal voltage w.r.t MEG candidate location g.

x_{ij} Reactance of DL (i, j).

$\overline{Y}_z$ Median of peak ground acceleration (PGA) of PDSs under damage state z.

Chapter 4

α_n^z Binary, 1 if slave MER z is deployed at node n, 0 otherwise.

γ_n Binary, 0 if load switch at node n is open and the load is shed, 1 otherwise.

θ_n^k Binary, 1 if master MER k is deployed at node n, 0 otherwise.

ξ_{nm}^p Line damage indicator, 1 if line (n, m) is damaged, 0 otherwise.

ξ_n^s Binary, 1 if faults happen on the secondary network of node n, 0 otherwise.

c^{ls} Load shed cost \$/kWh.

c^{ms} Master MER operational cost \$/kWh.

c^{sl} Slave MER operational cost \$/kWh.

k Index of available master MERs.

n, m Index of node in the distribution system.

$\overline{P}_k^{ms}$ Active generation capacity of master MER k.

$\overline{P}_z^{sl}$ Active generation capacity of slave MER z.

$\overline{Q}_k^{ms}$ Reactive generation capacity of master MER k.

$\overline{Q}_z^{sl}$ Reactive generation capacity of slave MER z.

r_{nm} Resistance of line (n, m).

s_{nm} Binary, 1 if RCS on line (n, m) is connected, 0 otherwise.

u_n^k Binary, 1 if node n is energized by the MG established by master MER k.

V_n^c Voltage of node n with respect to node c.

x_{nm} Reactance of line (n, m).

z Index of available slave MERs.

Chapter 5

β_ω Sample weight of uncertain MDP.

λ_v Voltage penalty factor.

λ_p Active generation capacity penalty factor.

λ_q Reactive generation capacity penalty factor.

c_s Cost of load shed.

D^p_m Active load demand of node m.

D^q_m Reactive load demand of node m.

F^p_{mg} Active power flow into node m with respect to DG located at node g.

F^q_{mg} Reactive power flow into node m with respect to DG located at node g.

g Index of node where DGs are located.

$\overline{P}_g$ The upper bound for the active capacity of DG located at node g.

$\overline{Q}_g$ The upper bound for the reactive capacity of DG located at node g.

r_{mh} Resistance of line (m, h).

u_{mg} Binary, 1 if node m is restored by DG located at node g, otherwise 0.

v_{mg} Voltage of node m w.r.t DG located at node g.

$\overline{v}$ The upper bound for nodal voltages.

$\underline{v}$ The lower bound for nodal voltages.

x_{mh} Reactance of line (m, h).

$\mathbb{C}_{mh}$ Set of conductors on line (m, h).

$\mathbb{L}_i$ Set of distribution lines in node cell i.

$\mathbb{N}_{ch}(m)$ Set of child nodes of node m.

$\mathbb{P}_{mh}$ Set of poles supporting line (m, h).

$\mathbb{T}_d$ Set of trees beside conductor d.

$\mathcal{C}(s)$ The immediate cost function of state s.

$\mathcal{P}(s)$ The penalty function of real generation capacity of state s.

$\mathcal{Q}(s)$ The penalty function of reactive generation capacity of state s.

$\mathcal{S}(s)$ The total load shed function of state s.

$\mathcal{V}(s)$ The voltage penalty function of state s.

Chapter 1

Introduction

In this thesis, the stochastic resilience-oriented smart power distribution system (PDS) planning and operation against natural disasters are investigated. The main focus is on the development of resilient planning and operation strategies to enhance PDS resilience against the stochastic impact of natural disasters.

1.1 Background

Natural disasters which are characterized as high-impact low-probability extreme events can pose negative impacts on electrical infrastructures [1]. For example, in 2010, an 8.8 Richter scale earthquake hit the central part of Chile, damaging the Chilean Central Interconnected System, which provides electricity to over 93% of the Chilean population [2]. In 2017, hurricane Harvey made a landfall on the Texas Gulf Coast. Consequently, a total of six generators and dozens of substations are flooded in Southeast Texas and Louisiana, USA, with a total of 2,285 MW in capacity impacted [3]. In 2021, winter storm Uri struck Texas, USA. It is recorded that more than 4.5 million households are left without electricity, some for several days [4]. The statistics in Fig. 1.1 show the number of major blackouts caused by extreme events in the USA between 1986 and 2006, with greater than 50,000 customers affected [5]. It can be seen that the area of bars under the dotted line, representing the number of blackouts associated with natural disasters, such as earthquakes, extreme winds, wildfires and cold weather, occupies a large portion of the total area. This highlights the importance of investigating features of natural

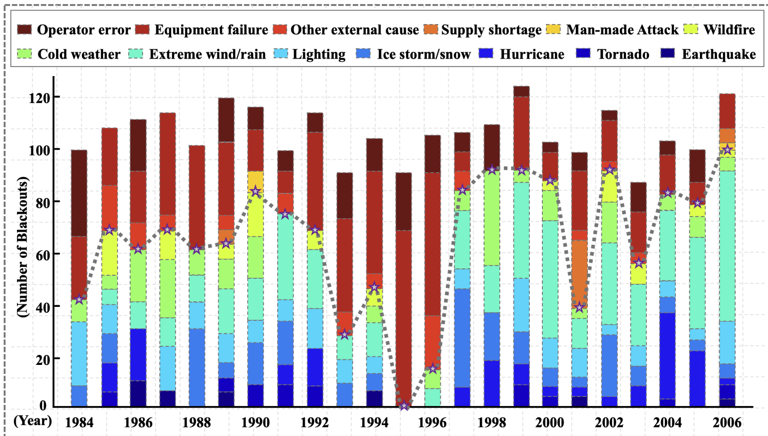

Figure 1.1: Outages induced by extreme events between 1984 and 2006 in U.S.A.

disasters and resilient strategies to reduce the risks of outages.

Smart PDSs, integrated with intelligent decision support, provides an opportunity to address the above challenges. Compared with traditional PDSs, smart PDSs are equipped with advanced techniques such as distributed generation, sensing, communication, and computing, which can effectively enhance PDS resilience [6, 7]. An illustration of the smart PDS architecture with resilience-oriented coutnermeasures is shown in Fig. 1.2. It contains three layers, which are electric power systems, communication systems, and decision support systems [8]. Between two adjacent layers, there are two-way data flow to transfer the grid information upwards and the resilient operation decisions downwards. Moreover, each layer of smart PDS has its own countermeasures in terms of resilience enhancement. The electric power system improves the smart PDS resilience from the perspective of advanced electrical techniques and components, such as hardened distribution lines (DLs), distributed energy resources (DERs) and intelligent electronic devices (IEDs) [1]. For the communication system, the resilience can be achieved through architectural communication frameworks such as Resilience and Survivability for Future Networking (ResumeNet) [9], Resilient Communication Services Protecting End-user Applications from Disaster-based Failures (RECODIS) [10], and Resilient and Survivable Networks (ResiliNets) [11]. Moreover, the decision support system enhance the resilience through resilience-oriented decision-making [12]. Specifically, the

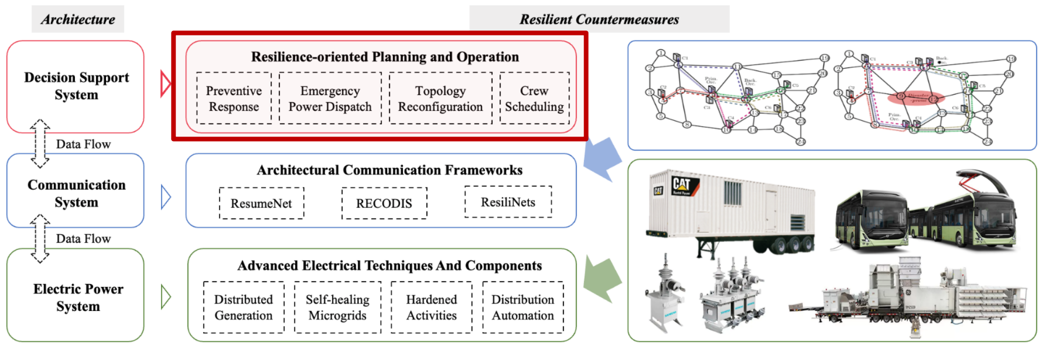

Figure 1.2: Smart PDS architecture with resilience-oriented countermeasures.

data collected from the electric power system layer are forwarded into the simulator, where the stochastic impact of natural disasters can be evaluated by assessment tools. Then, the resilient decisions can be optimized by using resilience enhancement strategies.

The resilience-oriented strategies for smart PDSs against natural disasters can be categorized into two stages: pre-disaster preventive planning and post-disaster emergency operation. The pre-disaster planning stage investigates resilient investment portfolio of electrical components including hardening design and placement of IEDs and DERs with benefit-cost analysis. Specifically, the hardening design of electrical components such as DLs and substations refers to a structural boost of their robustness to the external strike [13]. In comparison, IEDs and DERs play fundamental roles in restoration through distribution automation and distributed generation, respectively [14]. For example, IEDs such as remotely controlled switches (RCSs) can facilitate the topology reconfiguration of PDSs and make it more flexible [15]. In particular, when coordinating DERs with IEDs, dynamic microgrids (MGs) can be established for emergency restoration. Also, the utilization of DERs can be more efficiency, when being mounted on trucks and becoming mobile energy resources (MERs). By contrast, the post-disaster operation stage determines the restoration scheme using the existing electrical components and the repair scheduling of the damages. The restoration and repair decisions can be obtained by optimization problems with resilience-oriented objectives, such as the shortest outage duration, the largest amount of restored load and the most resilient restoration networks. Then, the optimal restoration scheme can be worked out, which can be used as guidelines for system operators to restore interrupted customers step-by-step.

Based on the above discussion, it is obvious that the advanced techniques and components in the electric power system layer of smart PDSs are significant critical in resilience enhancement. Hence, commercial products are launching in this domain, such as CAT Mobile Generator [16], GENERAC Mobile Generator [17], TECLOMAN Mobile Energy [18], ConEdison Transportable Energy [19], Volvo Electric Bus [20], ALUMERO Mobile Solar Container [21], and UPRISE ENERGY Portable Wind Turbine [22]. Some of them have been adopted by utility companies. For instance, Portland General Electric in the U.S. has started a transmission and distribution network hardening project since 2017. It aims to maintain a higher seismic preparedness to the nearby Cascadia Subduction Seismic Zone [23]. Also, Nippon Telegraph and Telephone in Japan built MGs by mobile emergency generators (MEGs) and energy storage systems (ESSs) after the 2011 Tohoku earthquake to supply emergency power [24, 25]. However, the well-utilization of these advanced techniques and components requires systematic research especially when considering the stochastic nature of natural disasters. Moreover, some types of natural disasters can impose destructive impact over a period of time. For example, the restored power services after the main shock of Great East Japan Earthquake in 2011 were interrupted once again by aftershocks, resulting in post-restoration failures [26]. It indicates that even with extensive pre-disaster planning and post-disaster operation, future uncertain damages may still interrupt the restoration. Hence, it is necessary to investigate resilience enhancement strategies for PDSs against post-restoration failures considering underlying uncertainties. Furthermore, the interdependence between the physical layer and the cyber layer of smart PDS brings about additional issues, because the malfunctions of one layer may affect the other. Accordingly, two cyber-physical interdependent impacts arise: 1) Uncertain damages: For natural disaster induced outages, the damage information can be uncertain to the system operator. The reason is that the bulk system is very likely to collapse during outages, such that grid power cannot be delivered to the cyber-physical distribution systems (CPDSs). Without power delivery indicates no available voltage and current data can be recorded by IEDs, even though some IEDs are equipped with backup batteries [27]. Then, fault location algorithms cannot be applied, since these algorithms require, at a minimum, real-time measured voltage and current of DLs; 2) Communication interruption: Some of the communication can be interrupted by natural disasters, such that RCSs cannot be controlled remotely. In practice, the communication links within a smart grid can be classified into wired and wireless links [28]. The control center connects to the base stations through optical fibers, which are typically integrated with the overhead power lines to form the optical fiber composite overhead ground wire (OPGW). Then, the base stations communicate with the RCSs through wireless links. However, when natural disasters strike, the OPGW can also be damaged. The control center may lose connection with the base station, and the RCSs that are within the range of this base station cannot be reached. Therefore, when investigating resilient power restoration strategies for CPDSs, it is essential to consider the cyber-physical interdependent impacts including uncertain damages and communication interruption.

In summary, the research regarding stochastic resilience-oriented planning and operation for smart PDSs against natural disasters still needs further investigation. In particular, the following four research topics are studied in this thesis:

1. Stochastic planning for PDS resilience enhancement;
2. Resilient operation against uncertain post-restoration failures;
3. Microgrid formation for large-scale deployment of MERs;
4. Sequential restoration considering cyber-physical interdependent impacts.

1.2 General Terms and Definitions

In this section, the important terms used in this thesis are defined to clearly identify the scope of work done in this research.

1.2.1 Power System Resilience

Power system resilience is defined as the ability to robustly withstand destructive strikes and rapidly recover from post-contingency states [29]. It can be chronologically categorized into two stages: pre-disaster resilient planning and post-disaster emergency operation stages [30]. The first stage aims to boost power system robustness against natural disasters. For example, hardening overhead power lines, elevating substations, installing switches, and purchasing distributed generators are all effective resilient planning approaches. The second stage focuses on corrective and responsive actions, such as demand side management, emergency power dispatch, and defensive islanding. Its aim is to take operational measures based on vulnerability analysis to alleviate the negative impacts of natural disasters. Compared with power system reliability, which is evaluated under high-probability and low-impact events, power system resilience is considered based on low-probability and high-impact events. The high-probability and low-impact events are often caused by one single fault without stochastic features, e.g., accidental equipment failures. While, the low-probability and high-impact events can impose multiple damages with randomness, which are more difficult to deal with in terms of power restoration.

1.2.2 Load Restoration

Load restoration in the context of PDS resilience refers to the process of restoring power services to consumers during an outage. This process is particularly crucial for maintaining the functionality of critical loads, such as hospitals, emergency services, communication networks, and other essential infrastructures. When conducting load restoration, a resilience-oriented strategy is necessary to restore loads as fast as possible considering voltage and frequency regulation. In other words, a rapid and efficient restoration of electrical power is desired while maintaining stable frequency and voltage levels. To this end, the restoration strategy determines a control sequence of DER starting up and RCS switching, which can be used as guidelines for system operators to restore interrupted customers step-by-step [31]. Similar to the bottom-up approaches in power systems where the generation units are capable of self-starting (i.e., black-start), in a restoration-based microgrid at least one DER should be able to start up by itself, with functionality of maintaining voltage and frequency stability [32].

1.2.3 Cyber-physical Power Systems

The existing power systems are undergoing a paradigm shift from traditional power grids toward smart grids [33]. By employing electrical and information technologies, such as distributed generation, advanced metering infrastructures (AMIs), and IEDs with remote monitoring and control functions, power systems are evolving into a complex cyber-physical system [34]. For example, as defined by the U.S. Department of Energy (DOE), smart grid is an intelligent electricity grid integrating digital communication technology [35]. This evolution can effectively enhance power system resilience, as well as reliability, efficiency and functionality. The reason is that in traditional power systems, physical components such as generators, transformers, and power lines are operating independently. However, in a cyber-physical power system, these components in the physical layer are interconnected through a cyber layer network of sensors, actuators, and communication systems, allowing for real-time monitoring, control, and optimization. In summary, cyber-physical power systems represent the next generation of power syst ems, offering advanced monitoring, control, and optimization capabilities to meet the evolving demands of modern society.

1.2.4 Mixed Integer Programming

Mixed Integer Programming (MIP) is a mathematical optimization technique used to solve optimization problems, where some of the decision variables are integers while others are continuous. In MIP, the objective function and constraints can be either linear or nonlinear, and the decision variables are subject to the constraints. The objective function is a mathematical expression that defines the objective of the optimization problem. The constraints are employed to impose limitations on the decision variables, defining the feasible region of the optimization problem. MIP problems are commonly used to model and solve a wide range of decision-making problems across various fields, including operations research, logistics, scheduling, finance, and engineering. The solutions to MIP problems are specialized optimization algorithms, such as branch-and-bound, branch-and-cut, or branch-and-price methods. These algorithms systematically explore the solution space to identify the best feasible solution within a reasonable amount of computational time. There are several commercial solvers available for solving MIP problems efficiently, such as CPLEX, Gurobi, MOSEK, and SCIP. These commercial solvers offer robust and efficient algorithms for solving MIP problems of various sizes and complexities. They are widely used in academia, industry, and research institutions for addressing real-world optimization challenges across different domains.

1.2.5 Two-stage Stochastic Programming

Two-stage stochastic programming is a mathematical optimization technique used to address decision-making problems under uncertainty that unfold over multiple time periods or stages. This approach is commonly used in various fields, including operations research, finance, energy, and supply chain management, to make robust decisions in the face of uncertain future events. Specifically, the decision-making process is divided into two stages: the first stage represents decisions made before uncertainty is revealed, and the second stage represents decisions made after the realization of uncertain events. Accordingly, the decision variables are also defined for both stages. The first-stage decision variables are typically deterministic, representing decisions made before uncertainty is realized. The second-stage decision variables are stochastic, depending on the realization of uncertain events. The uncertainties are characterized through a scenario set which includes possible outcomes that can occur in the future. Each scenario is associated with a probability, which represents the likelihood of occurrence. The objective of two-stage stochastic programming problem is to minimize or maximize the expected value of a certain criterion, such as cost, profit, or risk. Since a large number of decision variables and scenarios are often involved, solving two-stage stochastic programming problems can be challenging. In this respect, the solution approaches such as decomposition methods, scenario reduction techniques, or stochastic approximation methods can be adopted to reduce the computational complexity effectively.

1.2.6 Hidden Markow Model

A Hidden Markov Model (HMM) is a statistical model used to model sequences of observations or data that are assumed to arise from a hidden or unobservable process. An HMM consists of a finite set of hidden states, which represent the underlying or unobservable processes that generate the observed data. Each state is associated with a probability distribution over possible observations. At each time step, the HMM emits an observation based on the current hidden state. The relationship between states and observations is probabilistic, meaning that each state emits observations with certain probabilities. HMMs model the transitions between hidden states using transition probabilities. These probabilities represent the likelihood of transitioning from one state to another at each time step. HMMs are characterized by the Markov property, which states that the probability distribution of future states depends only on the current state and not on the previous states. This property simplifies the modeling and inference process, making HMMs a powerful tool for analyzing sequential data with hidden structure.

1.2.7 Markov Decision Process

Markov Decision Processes (MDPs) provide a mathematical framework for modeling decision-making problems under uncertainty. It is a specific category within stochastic dynamic programmings, where the underlying stochastic process is an extension of Markov chains. While, the difference is that the outcomes of an MDP is dependent on both the inherent Markov property and the decisions made by a decision maker. MDPs serve as valuable models for random processes in stochastic dynamic programming and reinforcement learning, with wide-ranging applications in disciplines like automatic control, economics, and manufacturing. At each time step, the MDP is in a specific state, and the decision maker may choose any feasible action in this state. Then, the MDP will transit into a new state following a random process with defined transition probabilities, and receive a reward according to the defined immediate reward function at the next time step. The decision maker aims to optimize a long-term objective, such as maximizing cumulative rewards or minimizing costs, by selecting the optimal actions in each state of the system.

1.3 Research Definition and Literature Review

In this section, the research problems will be defined for the aforementioned four research topics. Also, the existing research works in literature will be discussed.

1.3.1 Stochastic Planning for Resilient PDSs

In this research, we study the stochastic planning of resilient PDSs. The portfolio of resilient countermeasures including hardening DLs and investing new MEGs and mobile energy storage systems (MESSs) are investigated with stochastic analysis. The objective is to obtain the optimal portfolio to minimize the investment and the expected interruption cost.

In literature, there are several planning strategies are developed for resilient PDS against earthquakes. For examples, authors in [36] proposed a planning model for system planners to obtain the optimal solution for DL hardening and distributed generator (DG) placement. It demonstrates microgrids together with infrastructure hardening can reduce the total loss of load compared with the situation in which only hardening measures are adopted. Also, authors in [37] presented a resilience-driven framework to determine the optimal location of ESSs in PDSs against earthquakes. A resilience metric is defined based on seismic vulnerability assessment to determine the optimal size of ESSs. Also, the effectiveness of deploying ESSs in PDSs for seismic preparedness is proven. Moreover, in [38], MESSs with optimized capacity are utilized to improve PDS seismic resilience. It shows MESSs can outperform ESSs despite with lower capacity due to their mobility. Nevertheless, the methods in [36–38] are deterministic in nature without considering the stochastic impact of earthquakes. By contrast, authors in [39–44] employ stochastic analysis in the resilient PDS planning strategy to mitigate the random impact of other disasters such as hurricanes. For examples, in [39, 40], the DL hardening and DG placement problems are formulated as tri-level robust optimization problems. The first level determines the resilient planning solution, the second level models the worst-case damage through an uncertainty set, and the third level executes emergency restoration. Also, authors in [41–43] employ two-stage stochastic programming to solve the same problem. The randomness of natural disasters are included by a scenario set. The objective is to determine the planning solution that can minimize the investment cost and the expected load shed cost over all scenarios. In [44], an information gap decision theory based DG allocation and hardening scheme is proposed to address the uncertain damages of natural disasters. However, these works mainly focus on the planning of DGs, while the utilization of ESSs still needs to be investigated. In addition, how to consider and integrate the unique impact of earthquakes on PDS resilience in the stochastic optimization tools still requires extensive research.

Some recent research have shown that ESSs are of significant importance in load restoration after natural disasters [45, 46]. They can provide localized ancillary services, such as load leveling, peak shaving, and voltage regulation. Especially, when mounted on a truck and becoming MESSs, fast deployment during extreme events can be achieved because of their mobility [47]. Also, coordinating MESSs with DGs and MEGs can further improve restoration capability. In this respect, the resilient response strategies are well studied. For example, in [48, 49], MESSs are dynamically scheduled in coordination with the dispatch of DGs in post-disaster restoration. It shows that the transportable and chargeable features of MESSs can enable energy exchange between different MGs, leading to a lower curtailment. Also, in [50–52], the operation of MEGs and MESSs are co-optimized over a multi-time scale, where the advantages of the co-optimization in resilience enhancement is proven. However, strategies in [48–52] are developed for post-disaster emergency response instead of pre-disaster long-term investment planning. How to optimize the planning solution for resilient PDSs against earthquakes considering the coordination of MEGs and MESSs is still an open issue.

1.3.2 Resilient Opertation Against Post-Restoration Failures

In this research, we investigate the PDS resilience enhancement strategy considering post-restoration failures. The objective is to establish emergency restoration using the most resilient networks and schedule repair process against future uncertain damages.

In literature, the planning and placement of energy resources such as energy storage systems and distributed generators against earthquakes are studied in [36, 37]. The fragility curves are developed to characterize seismic impact and to determine the failure probabilities of electrical components. These two studies demonstrate that it is important to pre-position energy resources in PDSs against earthquakes, especially in active seismic zones. Also, to further achieve flexibility in post-earthquake restoration, MEGs are utilized in [38, 50]. It is shown in these research works that MEG reallocation, which is adaptive to the realized seismic damages, can result in an obvious reduction in load shedding. Yet, literature [36–38, 50] focus on improving restoration capability after one shock of earthquakes without considering post-restoration failures that may arise from future shocks. Thus, PDS resilience enhancement strategies considering post-restoration failures in the context of multi-shocks of earthquakes need further investigation. In [53–55], the real-time allocation of MEGs is investigated based on a temporal-spatial status model. The logic of MEG transitions between parking and travelling is optimized to improve PDS resilience. In [56], the planning and reallocation problem of MEGs is coordinated in a two-stage framework against hurricanes and extreme weather events. The transition routes of MEGs are optimized for the fastest restoration. In [43], a three-stage model is proposed against hurricanes, which contains a long-term MEG investment stage, a pre-disaster pre-positioning stage, and a post-disaster reallocation stage. In [57], the investment problem of MEGs is studied to achieve a trade-off between normal conditions and emergency conditions under hurricanes. However, the post-restoration failures are still not considered in [43, 53–57]. Hence, specifically for multi-shocks of earthquakes, the restoration schemes by [43, 53–57] may not be resilient against future uncertain damages that may cause post-restoration failures.

To address the challenge arising from post-restoration failures, restoration paths are adopted to deal with future natural disasters in [58–60]. In [58], the restoration paths are defined as “the electric circuit that can deliver power from the source node to one critical load (CL)". Accordingly, each restoration path consists of a group of connected DLs. It aims to restore CLs using distributed generators following the restoration path with the highest resilience, which can at maximum reduce the risk of post-restoration failure. Yet, since the resilience is evaluated based on the number of lines forming the restoration path, the difference in length of lines can deteriorate its performance. To address this issue, the line length is included in the resilience evaluation in [59, 60]. Specifically, the restoration paths are considered as microgrids. Then, the objective can be transformed into deploying MEGs to minimize the weighted number of lines in microgrids. Even though post-restoration failures are considered in [58–60], their approaches are deterministic in nature without stochastic analysis of multi-shocks of earthquakes. Therefore, the PDS resilience enhancement strategy incorporating the uncertainties of multi-shocks of earthquakes to deal with post-restoration failures is still an open issue.

Moreover, the repair process is not included in [58–60], which further degrades their performance, especially for multi-shocks of earthquakes. The reason is that the available restoration paths can be monotonically reduced with the occurrence of multi-shocks of earthquakes, if no repair process is conducted. Some other works investigate the repair process under natural disasters. For example, in [50, 61], it is demonstrated that the restoration performance can be improved by incorporating the repair process. However, how to optimize the repair schedule is not studied. In [52, 62], the repair scheduling is investigated to obtain the optimal repair decisions that can maximize the restored load. The advantage of the optimal repair scheduling on resilience enhancement is demonstrated. In [53, 63], the repair crew teams are dispatched considering the shortest traveling time. Nevertheless, the research works [50,52,53,61–63] have one common issue that the repair process is scheduled based on known damages without considering future uncertain damages that may cause post-restoration failures. Therefore, in terms of multi-shocks of earthquakes, their performance can be deteriorated.

1.3.3 Microgrid Formation for Large-Scale MER Allocation

In this research, we investigate the dynamic MG formation approach for resilient load restoration considering large-scale MER deployment. The objective is to determine the optimal MG formation solution including MER deployment decisions and RCS on/off decisions to minimize the total weighted load shed after outages.

In literature, there are several research works contributing to this research area. For example, heuristic approaches are presented in [64, 65]. These approaches decompose the problem into two stages, which are MG formation and performance evaluation. The two stages will be conducted iteratively until some pre-specified requirements are satisfied. Specifically, in [64], the MGs are established by clustering nodes around DERs according to *k-means* algorithm. In [65], the MG networks are obtained based on graph theory and particle swarm optimization. Moreover, in [66, 67], deep reinforcement learning is employed for resilient microgrid formation. The problem is formulated as a Markov decision process (MDP), and a reinforcement learning framework is designed for topology reconfiguration. The advantages of heuristic and reinforcement learning approaches exist in the reduction in the computational time. Nevertheless, the optimal solution cannot be guaranteed. Also, the research works in [64–67] only consider DERs, while the utilization of MERs still needs investigation.

In [43, 68–80], the optimal solutions of the MG formation problems are optimized by formulating the problems into mixed-integer linear programming (MILP) problems. In [68, 70, 71], MG formation approaches are proposed for load restoration after natural disasters based on the parent-child relationship of network topology. Specifically, multiple MGs are formed on the top of the original distribution network. The RCSs are operated to form MG boundaries, and the DERs are dispatched to restore loads. In [43,69,72,73], the approaches in [68,70,71] are extended to load restoration which involves MERs as power sources. The flexibility of MERs compared to DERs in load restoration are demonstrated. Moreover, to improve computational efficiency, the commodity flow in graph theory is applied in [74–78]. In particular, the distribution network is represented by a graph, which is partitioned into several sub-graphs for MG formation. Since the graph has the same topology as the distribution network, the commodity flow conditions can ensure the MGs operated radially. Furthermore, a combined parent-child relationship and commodity flow MG formation approach is proposed in [79, 80]. It aims to shrink the feasible solution region by utilizing both the advantages of parent-child based and graph theory based approaches. In [81], the approaches based on the commodity flow in graph theory is also modified to deal with the mutual support of AC and DC feeders. Flexible stations with AC/DC/AC converters are utilized to interconnect AC and DC feeders with multiple voltage levels. A voltage support coordination strategy based on flexible stations is proposed for a flexible restoration considering spatial-temporal regulation. However, the MG power flow calculation of the approaches in [43, 68–80] are all based on the linearized Distflow (LinDistflow) model, and the approach in [81] is based on the Distflow model. They always demand the MG root and its corresponding topology [82]. If the MG root changes, the power flow must be calculated by equations based on the new topology [68]. This can lead to an increased number of variables and constraints in the optimization problem, and deteriorate their computational performance. Especially when MERs are involved and served as the MG root, the dynamic deployment of MERs can significantly complicate the solution space. Thus, the MG formation approaches in [43, 68–81] are efficient when small number of MER connection nodes are considered, but their applications in large-scale deployment of MERs in PDSs are limited.

1.3.4 Sequential Restoration in Cyber-Physical PDSs

In this research, we investigate the stochastic sequential CPDS restoration scheme considering cyber-physical interdependent impacts. The objective is to determine the optimal strategy to operate RCSs step by step, such that the loads can be restored by DGs as fast as possible.

In literature, resilient power restoration strategies are well-studied. In particular, smart grids featuring DGs, RCSs, and bidirectional communication links are commonly utilized in power system resilience enhancement. For example, in [58, 68, 83], power distribution networks are partitioned into multiple self-healing microgrids using MILP. All the MGs are powered by DGs and can be operated in parallel with dynamic boundaries formed by RCSs. However, these approaches can only produce a single-step solution to the final network configuration, which requires the system operator to have the complete damage information of the network. If some of the damages occur beyond the knowledge of the system operator, the solution becomes invalid. In [31, 62, 84, 85], multi-step sequential restoration strategies are developed based on MILP, which can provide the system operator with a sequence of RCS control actions without violating the voltage, frequency, and line capacity conditions at each step. However, the uncertain damages are still not considered, so that the occurrence of any unexpected damages can invalidate the deterministic sequential restoration decisions. For example, a closing operation of an RCS cannot be conducted as scheduled, as there exist damages beyond the damage information that the system operator can access. Otherwise, short circuits will happen if the RCS is closed. Accordingly, all the subsequent sequential actions are forced to suspend. The amount of restored loads is directly affected by how many steps that the system operator can take following the sequence of actions before a suspension.

To include damage uncertainties into the decision making, the utilization of stochastic programming and robust optimization are well studied. In [86], a microgrid-based restoration approach considering subsequent random contingencies is proposed. The problem is formulated as a hybrid stochastic-robust optimization model. The uncertain damages after restoration is addressed using a damage scenario set considering DL failure probabilities. Similarly, in [70], the subsequent contingencies are modeled through distributionally robust optimization. The expected restoration is maximized with respect to the worst-case distribution of uncertain damages. However, approaches in [70, 86] are focused on potential uncertain damages, thus the already occurred damages which can be uncertain to the system operator requires further investigation. In other words, approaches in [70, 86] are not state-based, hence they cannot be employed to guide the system operator to dynamically take actions along with the uncertainties being observed. To address the state-based sequential decision making problem, MDP is a powerful tool. By employing MDPs, the optimal actions at each step can be obtained, which can maximize the amount of restored loads in the long run in a stochastic environment. In [87], MDPs are utilized to model distribution network topology reconfiguration to enhance PDS resilience against hurricanes. It can produce a strategy that guides the system operator to take RCS operations considering network topology uncertainties resulting from hurricane damages. In [88], the sequential PDS restoration problem against earthquakes is formulated as an MDP. The system operator is expected to control RCSs one by one to restore power services provided by DGs. However, since the stochastic parameters of an MDP are often estimated from limited data or prediction models, in some applications, they cannot be specified accurately. For example, different wind velocities and directions of hurricanes can result in different fragilities, and thus uncertain transition functions of an MDP. Hence, approaches in [87, 88], which include damage uncertainties while disregarding MDP model uncertainties, may have deteriorated performances.

In addition, communication interruption is not considered in [31, 58, 62, 68, 70, 83–88]. In these research works, communication links are assumed to be constantly available, and RCSs can always be controlled remotely. Therefore, the malfunction of RCSs after natural disasters needs further investigation. In this sense, the dispatch of crew members to manually operate malfunctioning RCSs is studied in [89, 90]. In [91], drones installed with base stations are dispatched to establish emergency communication for RCSs. However, the approaches in [89–91] are deterministic, while the uncertain damages can degrade their applications.

1.4 Thesis Motivation and Contributions

Based on the above discussion, many new challenges are introduced to the strategies for resilient PDSs in the decision support system layer of smart PDSs. First of all, the random impact of natural disasters calls for PDS planning with stochastic analysis, making the problem interdisciplinary. In other words, the stochastic mathematical models of natural disasters should be included in the planning problem formulation, such that practical decisions can be obtained. Secondly, the extended events in the aftermath of a natural disaster, such as hurricane induced flooding and ensuing aftershocks of an earthquake, can strike again, interrupting the established restoration and causing post-restoration failures. It means that PDS resilience should be evaluated and maximized against uncertain extended events, when making restoration schemes to the outages. Thirdly, the mobility of MERs can improve restoration efficiency, however resulting in an increased computational complexity simultaneously. Especially, when it comes to large-scale deployment of MERs, it can consume considerable amounts of time to obtain the optimal MG formation scheme. Last but not least, the two-way data flow between the electric power system layer and the communication system layer makes smart PDSs cyber-physical interdependent. It means that the damages in the physical layer can interrupt the communication in the cyber layer, and the interruption of the communication in the cyber layer can result in out of connection with IEDs in the physical layer. For the first two challenges, we select earthquakes as natural disasters, since earthquakes are a very typical natural disaster, having both spatial and temporal features. For the third challenge, we consider damages caused by general natural disasters, and focus on developing MG formation approach for large-scale MER deployment. For the forth challenge, hurricanes are incorporated, as the area that hurricanes affect is enormous which can result in large-scale blackouts and cyber-physical interdependent impact. Note that the applications of the proposed research works are not limited to earthquakes and hurricanes. Instead, natural disasters with similar features can also be dealt with by modifying the mathematical model accordingly. The detailed contributions of this thesis are described as follows:

1.4.1 Stochastic Planning for PDS Resilience Enhancement Against Earthquakes

In this research, the stochastic planning of resilient PDSs against earthquakes is studied. Specifically, the portfolio of resilient countermeasures including hardening DLs and investing new MEGs and MESSs are investigated with stochastic analysis. The objective is to determine the optimal portfolio to minimize the investment and the expected interruption cost. During the decision-making, the MEG and MESS coordination including co-allocation and energy exchange is also considered. Then, the main contributions of this research are threefold:

1. A stochastic spatial seismic damage model is developed based on the stochastic seismic impact analysis of PDSs. It considers the seismic attenuation, and addresses the randomness of seismic damages geographically;

2. A stochastic resilient PDS planning problem (SRDSPP) with a bi-level structure is formulated. The upper-level determines the optimal portfolio to minimize the investment cost and the expected interruption cost, whereas the lower-level performs contingency post-disaster operation considering coordination between MEGs and MESSs;

3. A solution procedure is proposed, which includes the scenario aggregation to reduce the size of scenario set, and the endogenous uncertainty relaxation to address the DL hardening decision-dependent uncertainty. Then, the original problem with $\min\max$ form is reformulated into a $\min\min$ form, based on which a decomposition method is proposed to speed up the computation.

1.4.2 Data-Driven Resilience Enhancement for PDSs Against Multi-shocks of Earthquakes Under Uncertainties

In this research, a resistibility index (RI) is developed to stochastically evaluate the resilience of restoration paths based on hierarchical hidden Markov models (HHMMs). The historical earthquake data is incorporated as information of multi-shocks of earthquakes. Then, by using the RI metric, a data-driven PDS resilience enhancement strategy is proposed against multi-shocks of earthquakes. It includes the pre-disaster MEG investment and pre-positioning against multi-shocks, and the post-disaster MEG reallocation and repair scheduling against aftershocks. The main contributions of this research are fourfold:

1. A RI metric is developed based on HHMM and historical earthquake data to stochastically evaluate restoration path resilience;

2. A data-driven PDS resilience enhancement strategy is proposed. The resilient MEG investment, pre-positioning and reallocation, and repair scheduling of restoration paths are determined based on RI metric;

3. The repair scheduling problem is formulated as an adaptive multi-period two-stage stochastic programming problem. A revision period is introduced to obtain static repair decisions before the revision, which allowing the decisions to adapt to the uncertainties after the revision;

4. An iterative algorithm based on linear programming relaxation is proposed to reduce the computational complexity of the repair scheduling problem.

1.4.3 Efficient MG Formation for Resilient PDSs Considering Large-Scale Deployment of MERs

In this research, a dynamic MG formation approach for resilient load restoration is proposed considering large-scale MER deployment. Its objective is to determine the optimal MG formation solution including the MER deployment decisions and the RCS on/off decisions to minimize the total weighted load shed after outages. The main contributions of this research are fourfold:

1. An adaptive LinDistflow model is proposed based on the LinDistflow model and the single commodity flow in graph theory. The calculations of power flow and nodal voltages only require adjacent node information of the original topology rather than various MG topologies;

2. A dynamic MG formation problem is proposed considering large-scale deployment of MERs. The formulated problem demands no MG topologies, thus can result in a reduced number of variables and constraints;

3. A linearization technique based on the propositional logic constraints is proposed to address the problem nonlinearity resulted by the incorporation of adaptive LinDistflow model;

4. Computational complexity is analyzed, which shows that the proposed dynamic MG formation approach can improve the computational efficiency without loss of optimality.

1.4.4 Stochastic Sequential Restoration for Resilient Cyber-Physical PDSs Against Hurricanes

In this research, we investigate the stochastic sequential CPDS restoration scheme considering cyber-physical interdependent impacts. A sequential load restoration problem against hurricanes is formulated as an uncertain Markov decision process (UMDP). The cyber-physical interdependent impacts are considered through uncertain transition functions. The main contributions of this research are threefold:

1. The problem is formulated as a UMDP with uncertain state transition functions. The cyber-physical interdependent impacts are modeled by integrating the hurricane fragility of DLs and the stochastic RCS manual operation into transition probabilities.

2. To address model uncertainties of a UMDP resulted by variuous wind velocities and directions with respective occurrence, a minimax regret optimization considering sample weights is presented. The optimal minimax regret policy is obtained for robust RCS operations.

3. An approximate solution based on the regret Bellman equation and the minimax regret policy iteration algorithm is proposed to improve computational efficiency.

1.5 Thesis Outline

In this thesis, the stochastic resilience-oriented planning and operation for smart PDSs against natural disasters is studied. First of all, the stochastic planning of resilient PDSs considering uncertain impacts of earthquakes is investigated. The portfolio of resilient countermeasures including hardening DLs and investing new MERs including MEGs and MESSs are addressed through a two-stage stochastic programming problem. The MEG and MESS coordination including co-allocation and energy exchange is incorporated, so that the solution can be more resilient and cost-saving. Secondly, we extend our scope from one main shock to multi-shocks of earthquakes. Specifically, a data-driven PDS resilience enhancement strategy is proposed to deal with post-restoration failures. By employing HHMMs and historical earthquake data, the pre-disaster MEG investment and pre-positioning against multi-shocks, and the post-disaster MEG reallocation and repair scheduling against aftershocks are addressed. Thirdly, since MG formation is utilized in both the first two works, we further investigate efficient MG formation approach for large-scale MER deployment. By using the proposed adaptive LinDistflow model, the computational efficiency of MG formation is significantly improved. Last but not least, we further broaden our scope from physical systems to cyber-physical systems. The problem of sequential load restoration against hurricanes is investigated. By formulating the problem as a UMDP, the cyber-physical interdependent impacts caused by hurricanes is addressed. More specifically, this thesis consists of six chapters and is organized as follows:

- **Chapter 1: Introduction -** This chapter begins by providing an overview of the research background, emphasizing the significance of the study. Then, the general terms used throughout the thesis are described to highlight the research scope. Following this, the research problems are defined, and a comprehensive literature review is conducted to clarify the challenges associated with each research problem. Finally, the motivation and contributions of this thesis are presented.

- **Chapter 2: Stochastic Planning for PDS Resilience Enhancement Against Earthquakes -** This chapter investigates the stochastic planning of resilient PDSs against earthquakes. The problem is formulated as a risk-averse two-stage stochastic bi-level programming problem. The upper-level minimizes the total investment cost and the expected interruption cost. The lower-level minimizes the expected loss of load through MEG and MESS coordination, including co-allocation and energy exchange. To solve the problem, a scenario aggregation method and community detection is proposed to reduce the size of scenario set, and an endogenous uncertainty relaxation method is developed to address the DL hardening decision-dependent uncertainty. Then, the problem with $\min \max$ form is reformulated into a standard bi-level programming problem with $\min\min$ form. A decomposition method is also proposed to break up the problem into two separate sub-problems to speed up the computation. The effectiveness of the proposed PDS planning strategy against earthquakes is evaluated through case studies based on the IEEE 37-Node Test Feeder and the IEEE 123-Node Test Feeder.

- **Chapter 3: Data-Driven Resilience Enhancement for PDSs Against Multi-shocks of Earthquakes Under Uncertainties -** This chapter studies a data-driven PDS resilience enhancement strategy against multi-shocks of earthquakes. A resistibility index (RI) is developed based on HHMM for stochastic resilience evaluation. The historical earthquake data are incorporated into the HHMM as observed information of multi-shocks of earthquakes. Based on the RI, the problems of pre-positioning and reallocation of MEGs are formulated as mixed-integer programming problems. The problem of repair scheduling is formulated as an adaptive multi-period two-stage stochastic programming problem, for which a revision period is introduced to allow the decisions to adapt to the uncertainties after the revision. To reduce the computational complexity, an iterative algorithm is presented based on linear programming relaxation. The strategy is verified via case studies on the IEEE 123-Node Test Feeder and historical earthquake data.

- **Chapter 4: Efficient MG Formation for Resilient PDSs Considering Large-Scale Deployment of MERs -** In this chapter, an adaptive LinDistflow model is proposed based on the single commodity flow model in graph theory. We first show that active and reactive powers can be represented as commodities, which are sent from one node to each of its adjacent nodes in the graph. Then, the power flow and nodal voltage calculation based on the commodity flow only requires adjacent node information of the original topology rather than various MG topologies caused by the dynamic deployment of MERs. Furthermore, by incorporating the adaptive LinDistflow model as constraints, a dynamic MG formation approach is proposed for resilient load restoration considering large-scale MER deployment. The effectiveness of the proposed approach is demonstrated based on the IEEE 37-Node, 123-Node and 8500-Node Test Feeders.

- **Chapter 5: Stochastic Sequential Restoration for Resilient Cyber-Physical PDSs Against Hurricanes -** This chapter proposes a stochastic sequential restoration scheme for CPDSs. The sequential restoration problem is formulated as a UMDP with hurricanes incorporated as natural disasters. Different wind velocities and directions are considered as hurricane scenarios, which are used to obtain the fragility of distribution lines. The fragility functions are further used for the derivation of uncertain state transition functions of the UMDP. The minimax regret optimization considering the sample weights of UMDP is presented. The robust sequential actions are determined, such that the loads can be restored in a timely manner. To improve computational efficiency, a minimax regret policy iteration algorithm is presented based on the regret Bellman equation. Case studies are conducted based on the IEEE 123-Node Test Feeder and historical data of Hurricane Bonnie to demonstrate the effectiveness of the proposed scheme.

- **Chapter 6: Conclusions and Future Works -** The contribution of this research and the future works are summarized in this chapter.

Chapter 2

Stochastic Planning for PDS Resilience Enhancement Against Earthquakes

In this chapter, the stochastic planning of resilient PDSs against earthquakes is studied. Specifically, the portfolio of resilient measures including hardening DLs, and investing MEGs and MESSs are investigated in a stochastic environment. A stochastic spatial seismic damage model is developed to geographically characterize the randomness of earthquakes. Based on the model, the PDS planning problem is formulated as a risk-averse two-stage stochastic bi-level programming problem. The upper-level minimizes the total investment cost and the expected interruption cost. The lower-level minimizes the expected loss of load through MEG and MESS coordination, including co-allocation and energy exchange. To solve this problem, a scenario aggregation method based on graph theory and community detection is proposed to reduce the size of scenario set, and an endogenous uncertainty relaxation method is developed to address the DL hardening decision-dependent uncertainty. Then, the PDS planning problem with $\min \max$ form is reformulated into a standard bi-level programming problem with $\min \min$ form. A decomposition method is also proposed to break up the problem into two separate sub-problems to speed up the computation. The effectiveness of the proposed PDS planning strategy against earthquakes is evaluated through case studies based on the IEEE 37-Node and IEEE 123-Node Test Feeders.

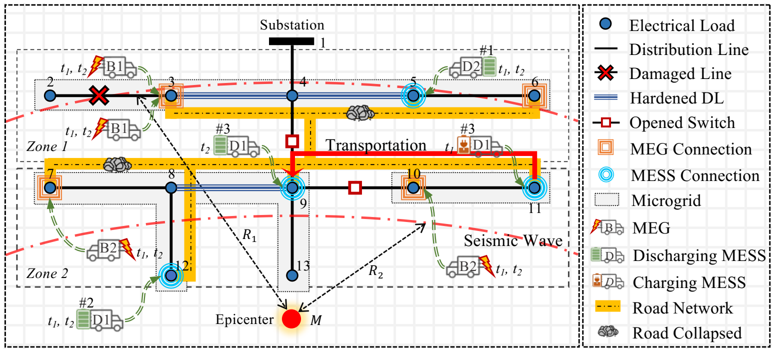

Figure 2.1: An illustration of the power distribution system model at time $t \in \mathbb{T} = \{t_1, t_2\}$ under one seismic damage scenario $\omega \in \Omega$.

2.1 System Model

In this section, the PDS model, the linearized Distflow model for MG formation, the stochastic spatial seismic damage model, and the stochastic repair model of damaged DLs are presented and discussed.

2.1.1 Power Distribution System Model

In this research, the PDS can be represented by an unweighted graph $\overline{\mathcal{G}} = (\mathbb{N}, \mathbb{L})$, where $\mathbb{N}$ is the set of electrical nodes, and $\mathbb{L}$ is the set of DLs. Two sets of nodes $\mathbb{K} \subset \mathbb{N}$ and $\mathbb{E} \subset \mathbb{N}$ are selected as MEG and MESS candidate connection nodes, respectively. Without loss of generality, we consider the IEEE 13-Node Test Feeder [92] as an example. As shown in Fig. 2.1, we have $\mathbb{N} = \{1, 2, 3, ...13\}$, $\mathbb{L} = \{(1,4), (2,3), ..., (9,13)\}$, $\mathbb{K} = \{3, 6, 7, 10\}$, and $\mathbb{E} = \{5, 9, 11, 12\}$. In addition, we use $\mathbb{B}$ and $\mathbb{D}$ to represent the set of different types of MEGs and MESSs which are available for investment, respectively. For resilient planning, the investment portfolio including the DL hardening decision h_{mn}, and the MEG and MESS investment decisions g_b and e_d are evaluated. Specifically, h_{mn} is a binary variable, equaling 1 if DL $(m, n) \in \mathbb{L}$ is hardened. And, g_b and e_d are non-negative integer variables, respectively, denoting the number of type b MEG ($b \in \mathbb{B}$), and the number of type d MESS ($d \in \mathbb{D}$) that are invested. For example, in Fig. 2.1, we have $\mathbb{B} = \{B1, B2\}$, $\mathbb{D} = \{D1, D2\}$, $h_{34} = h_{45} = h_{89} = 1$, $g_{B1} = 2$, $g_{B2} = 2$, and $e_{D1} = 2$, $e_{D2} = 1$.

Moreover, given one specific seismic damage scenario (ω), the load restoration is considered over a multi-time scale $(t \in \mathbb{T})$. Specifically, during the restoration, the microgrids will be established to provide emergency power. The nodes where MEGs are deployed will be served as the root nodes and provide the reference voltage V_0. To this end, the location of MEGs will remain the same throughout the multi-time scale. Also, the MESSs will be transported to some nodes, discharging or charging in coordination with MEGs. For this coordination, the allocations of MESSs can be dynamic. For example, as shown in Fig. 2.1, MESS #3 is charging at MESS connection node 11 at time t_1, and then transported to node 9 for discharging at time t_2. In addition, MESS transportation can be affected by road distances and road conditions between two MESS connection nodes. We use $t_{e'e}$ to denote the lag time of MESS transportation from MESS connection node e' to node e under normal road condition. We use $\zeta_{e'e}^{t\omega}$ to denote the status of road condition between MESS connection node e' and e. When $\zeta_{e'e}^{t\omega} = 0$, it means that the road between node e' and e during time t is collapsed, and no MESS can be transported on this road. For examples, in Fig. 2.1, we have $\zeta_{9,5}^{t_2\omega} = 0$, since the road from MESS connection node 9 to 5 is collapsed at time t_2. Furthermore, the MEG deployment variable θ_{kb}^{ω}, the MESS allocation variable $\gamma_{se}^{t\omega}$, the line switch status variable $\chi_{mn}^{\omega t}$, and the MESS discharging and charging decision variable β_e^t should be determined. In particular, θ_{kb}^{ω} is a non-negative integer variable, denoting the number of type b MEG that are deployed at MEG connection node k. And, $\gamma_{se}^{t\omega}$, $\chi_{mn}^{\omega t}$, and β_e^t are binary variables, equaling 1 if the s_{th} MESS transits to MESS connection node e at time t, the line switch on DL (m, n) is opened at time t, and the MESSs at MESS connection node e are discharging at time t, respectively. For example, as shown in Fig. 2.1, three microgrids are established with nodes 3, 7, and 10 being the root nodes, respectively. Accordingly, we have $\theta_{\{3,B1\}}^{\omega} = 2$, $\theta_{\{7,B2\}}^{\omega} = \theta_{\{10,B2\}}^{\omega} = 1$, and $\gamma_{\{\#1,5\}}^{\omega\{t_1,t_2\}} = \gamma_{\{\#2,12\}}^{\omega\{t_1,t_2\}} = \gamma_{\{\#3,11\}}^{\omega t_1} = \gamma_{\{\#3,9\}}^{\omega t_2} = 1$, and $\chi_{4,9}^{\omega} = \chi_{9,10}^{\omega} = 0$. Also, since MESS #1 (D2) and MESS #2 (D1) are discharging at time t_1, we have $\beta_5^{t_1} = \beta_{12}^{t_1} = 1$, and since MESS #3 (D1) is charging, we have $\beta_{11}^{t_1} = 0$.

2.1.2 Linearized Distflow Model for Microgrid Formation

The Distflow model is widely used in power flow analysis in radial distribution networks. Compared to the bus injection model, the Distflow model is much more numerically stable [82]. Also, the Distflow model is equivalent to the branch flow model when the phases of voltage and current are ignored [93]. Moreover, when the power losses along DLs are much smaller than the power flow, the nonlinear power losses term can be dropped [94]. Then, the Distflow model can be simplified to the linearized Distflow model, which has simple analytical solutions. Because resilient PDSs require a fast response to the outages by natural disasters [95], the computational advantage and the acceptable approximation of the linearized Distflow model make it more efficient and applicable in radial distribution networks. Hence, the linearized Distflow model is often employed in microgrid formation for resilient PDSs [68, 74]. In this research, following the work in [68], the linearized DistFlow model for MG formation can be stated as

$$\begin{aligned}\textstyle\sum_{h|(n,h)\in\mathbb{L}} P_{nhk}^{t\omega} = P_{mnk}^{t\omega} - D_n^{pt} + G_n^{pt\omega} + E_n^{pt\omega} \\ + \Delta S_n^{pt}(\omega) + \delta_{nk}^{pt\omega}, \forall m \in \mathbb{N}, n \in \mathbb{N}_{ch}(m), k \in \mathbb{K},\end{aligned} \tag{2.1}$$

$$\begin{aligned}\textstyle\sum_{h|(n,h)\in\mathbb{L}} Q_{nhk}^{t\omega} = Q_{mnk}^{t\omega} - D_n^{qt} + G_n^{qt\omega} + E_n^{qt\omega} \\ + \Delta S_n^{qt}(\omega) + \delta_{nk}^{qt\omega}, \forall m \in \mathbb{N}, n \in \mathbb{N}_{ch}(m), k \in \mathbb{K},\end{aligned} \tag{2.2}$$

$$V_{mk}^{t\omega} - V_{nk}^{t\omega} = (r_{mn}P_{mnk}^{t\omega} + x_{mn}Q_{mnk}^{t\omega})/V_0 + \delta_{nk}^{Vt\omega}, \tag{2.3}$$

where $P_{mnk}^{t\omega}$, $Q_{mnk}^{t\omega}$, $V_{nk}^{t\omega}$ are the active and reactive power flows on DL (m, n), and the voltage at node n with respect to MEG connection node k at time t under seismic scenario ω, respectively. Note that when MEGs are deployed at one MEG connection node k, a microgrid rooted at node k is established.

2.1.3 Stochastic Spatial Seismic Damage Model

1) Seismic Impact on PDSs: In seismology, ground-motion can be modeled as a seismic hazard curve. It is a function of magnitude M which can be represented by Richter magnitude scale, and distance R from the epicenter to the site of interest with uncertainty ε [96], given by

$$\ln Y = f(M, R) + \varepsilon, \tag{2.4}$$

where Y representing peak ground acceleration (PGA) is used to describe ground-motion. Also, the uncertainty ε can be modeled as a normally distributed random variable. Accordingly, Y follows a log-normal distribution with median value $\overline{Y} = 0.0159 \exp(0.868M)[R + 0.0606 \exp(0.7M)]^{-1.09}$, and standard deviation $\sigma = 1.45\overline{Y}$ [97]. Then, given a certain PGA (Y), the seismic fragility curves of a PDS can be developed to estimate the probability of a PDS reaching or exceeding a damage state $z \in \mathbb{Z} = \{Z_1, ...Z_n\}$, given by [98]

$$P(Z \geq z|Y) = \Phi\left[(1/\sigma_z) \ln\left(Y/\overline{Y}_z\right)\right], \tag{2.5}$$

where $\Phi[\cdot]$ denotes the standard normal cumulative distribution function. Then, the probability mass function of damage state given a certain PGA can be obtained by

$$P(z|Y) = P(Z \geq z|Y) - P(Z \geq z + 1|Y). \tag{2.6}$$

Also, the damage states are defined with respect to the percentage of damaged DLs out of all DLs, denoted by W_z [98]. Hence, the expected number of damaged DLs can be stated as $n_d = n_t \sum_{z \in \mathbb{Z}} P[z|Y] W_z$. Moreover, the probability of sampling a damaged DL (m, n) with a certain length l_{mn} is given in [60], which can be stated as $l_{mn} / \sum_{(m',n') \in \mathbb{L}} l_{m'n'}$.

2) Spatial Seismic Damage Scenario Generation: Earthquakes are one of the devastating natural disasters which start at the epicenter, and spread out in the form of seismic waves [99]. Related research show that the destruction of an earthquake decreases as the distance increases [100]. In this research, we present a stochastic spatial seismic damage model for PDSs to address the randomness of seismic damages geographically. Firstly, we partition the PDS into several spatial zones, where each zone has a unique distance R from the epicenter. For example, as shown in Fig. 2.1, we have two spatial seismic zones with R_1 and R_2 from the epicenter, respectively. Secondly, a PGA lognormal distribution is assigned to each zone, which is the probability density function of PGA given the magnitude M and respective distance R [96]. Lastly, a spatial seismic damage scenario set Ω is introduced to model the uncertainty of PGA and damage states. In particular, for each scenario $\omega \in \Omega$, the expected numbers of damaged DLs of different spatial zones are independently generated based on the PGA and the damage state experienced in different zones. After that, the damaged DLs in different zone can be randomly produced according to the probability of sampling a damaged DL. Also, each scenario ω is related to a realization $\boldsymbol{\xi}^{\omega}$, which is a vector of ξ^{ω}_{mn} indicating the DL status under such a scenario. When $\xi^{\omega}_{mn} = 1$, it means that DL (m, n) is damaged under scenario ω, otherwise we have $\xi^{\omega}_{mn} = 0$. For example, in Fig. 2.1, we have $\xi^{\omega}_{23} = 1$. Then, each scenario is associated with a probability of occurrence, and all the probabilities should add up to 1, i.e., $\sum_{\omega\in\Omega} \pi_{\omega} = 1$. Note that when generating scenarios, the PDS is considered as a standard design system. However, the seismic design with hardened DL decision $\boldsymbol{h}$ can influence the probabilities of occurrence of each scenario. This brings the so-called endogenous uncertainty, which means the uncertainty is decision-dependent.

Moreover, since the seismic scenarios are generated based on the fragility curves, the prediction error of the fragility curves can be introduced into the optimization problem and can affect the final solution. For example, fragility curves which are more fragile than the actual ones can induce seismic scenarios with more damaged DLs, and correspondingly an increased investment cost. Also, this dependency can be quantified by solving the optimization problem with parameter-adjusted fragility curves. For example, the seismic fragility curves employed in this research are developed based on the HAZUS earthquake loss estimation method [98]. We can shift the developed fragility curves to the left or right a little, or adjust the shape of the fragility curves a little to evaluate their impact on the final solution. Also, for the management of this dependency, fragility curves from different models can be employed for scenario generation, then stochastic programmings can be applied to find a solution to optimize the expected objective value over all the scenarios from different fragility curves. Through this way, the impact of fragility curve uncertainty can be alleviated. However, the above-mentioned is still an open issue, which needs further investigation. We want to emphasize that no matter how the dependency on the fragility curve is quantified and managed, the accuracy of fragility curves themselves is more relevant. In earthquake engineering, both analytical data and empirical data can be employed to validate the accuracy of the seismic fragility curves. For examples, in [101], damage data collected in real earthquakes are used for prediction accuracy evaluation. In [102], laboratory experiments are conducted to verify the structural capacity of poles under static loading.

In addition, the presented model is different from the models in [36–38, 50], which regard the whole PDS as one single point from the epicenter, without consideration of the seismic attenuation. Since a PDS with several feeders typically covers a service territory with a scale of dozens of square kilometers [103], one single point cannot include the changing destruction of earthquakes by distances. Accordingly, the vulnerable parts of a PDS may not be identified effectively. For example, DLs which are further away from the epicenter than others should occur less often among all the scenarios, while in the existing models, this distance impact is not considered. In comparison, the proposed model partitions the PDS into several zones, such that the vulnerable parts of each zone are identified separately. Hence, the proposed model can be more realistic, especially when the changing destruction of earthquakes by distances cannot be ignored.

2.1.4 Stochastic Repair Model of Damaged DLs

During the outages caused by earthquakes, the crew members will be dispatched by utilities to repair the damaged DLs. The repair duration can be modeled as a random variable (τ), which follows Weibull distribution, given by [104]

$$f(\tau) = \begin{cases} \frac{\alpha_1}{\alpha_2}(\frac{\tau}{\alpha_2})^{\alpha_1 - 1} e^{-(\tau/\alpha_2)^{\alpha_1}} & , \tau \geq 0 \\ 0 & , \tau < 0 \end{cases} \tag{2.7}$$

where α_1 is the shape parameter and α_2 is the scale parameter. Then, for one specific seismic damage scenario ω, the repair sequence of damaged DLs is generated as follows. First, one damaged DL (m, n) is randomly generated to repair. Second, we sample the repair Weibull distribution to generate the repair duration τ_1 for this damaged DL. Herein, we use $r_{nm}^{t\omega}$ to denote the DL repair status. If $r_{mn}^{t\omega} = 1$, it means that the damaged DL (m, n) under scenario ω is in the repaired status. Accordingly, we have $r_{mn}^{\{t=1,2,...,\tau_1-1\},\omega} = 0$ and $r_{mn}^{\{t=\tau_1,\tau_1+1,...,T\},\omega} = 1$. Next, these two steps are repeated by selecting another damaged DL (m', n') to repair and generating a repair duration τ_2 randomly. Assumed that there is only one crew team, then the repair should be conducted sequentially, hence the time that DL (m', n') gets repaired should be $t = \tau_1 + \tau_2$. Then, we have $r_{m'n'}^{\{t=1,2,...,\tau_1+\tau_2-1\},\omega} = 0$ and $r_{m'n'}^{\{t=\tau_1+\tau_2,\tau_1+\tau_2+1,...,T\},\omega} = 1$. Also, this process will be repeated until $t = \tau_1 + \tau_2 +, ..., +\tau_n$ exceeds the multi-time scale considered in the model.

2.2 Stochastic Resilient PDS Planning Problem Formulation

In this research, the resilient PDS planning is achieved through hardening DLs, and investing MEGs and MESSs considering stochastic seismic impact. To this end, we formulate the SRDSPP as a risk-averse two-stage stochastic bi-level programming problem [105]. Firstly, the upper-level generates the representative action including PDS planning decision $\{\boldsymbol{h}, \boldsymbol{g}, \boldsymbol{e}\}$, and decision-dependent seismic scenario ω. Secondly, the lower-level reacts to the upper-level's action by minimizing the multi-time total loss of load in the context of time varying load profiles. Also, the lower-level's reactions including MEG and MESS coordination (co-allocation and energy exchange), and topology reconfiguration can be performed. Finally, the upper-level minimizes the total cost including the investment cost, and the expected multi-time interruption cost after obtaining the lower-level's reactions. Then, the optimal resilient PDS planning solution $\{\boldsymbol{h}^*, \boldsymbol{g}^*, \boldsymbol{e}^*\}$ can be obtained. Different from the research in [39–44], our proposed planning strategy incorporates MESSs, coordinates the operation of MEGs and MESSs, and co-optimizes their respective investment, which leads to a full utilization of different types of MERs. Moreover, the inclusion of risk-aversion provides a trade-off between the cost and the risk, which can be used as investment references for system planners such as utility companies. In this section, the problem formulation will be discussed.

2.2.1 Upper-Level Resilient PDS Planning Problem

The upper-level planning problem is formulated as a two-stage stochastic programming problem. The first-stage determines "here and now variables", including the

DL hardening decision h_{mn}, and the MEG and MESS investment decisions g_b and e_d. The second-stage includes "wait and see variables", which is the loss of load variable $\Delta S_n^{pt}(\omega)$. Then, the upper-level objective is to obtain the optimal investment portfolio $\{\boldsymbol{h}^*, \boldsymbol{g}^*, \boldsymbol{e}^*\}$, which can minimize the total cost, given by

$$\min_{\boldsymbol{h},\boldsymbol{g},\boldsymbol{e}} \left\{ c_h \boldsymbol{l}^\top \boldsymbol{h} + \boldsymbol{c}_g^\top \boldsymbol{g} + \boldsymbol{c}_e^\top \boldsymbol{e} + \mathcal{F}\phi(\Delta \boldsymbol{S}^p) \right\}, \tag{2.8}$$

$$\phi(\Delta \boldsymbol{S}^p) = \mathbb{E}_\omega \Big\{ \min_{\Delta \boldsymbol{S}^p(\omega)} c_s \sum_{t\in T} \sum_{n\in\mathbb{N}} \Delta S_n^{pt}(\omega) \Big\}, \tag{2.9}$$

where $\boldsymbol{h} \in \mathcal{H} \subseteq \{0,1\}^{|\mathbb{L}|}$, $\boldsymbol{g} \in \mathcal{G} \subseteq \mathbb{Z}^{|\mathbb{B}|}$, $\boldsymbol{e} \in \mathcal{E} \subseteq \mathbb{Z}^{|\mathbb{D}|}$. Also, $|\mathbb{L}|$ denotes the number of DLs, and $|\mathbb{B}|$ and $|\mathbb{D}|$ represent the number of types of MEG and MESS, respectively. Note that $\boldsymbol{h}$, $\boldsymbol{g}$, $\boldsymbol{e}$, and $\Delta \boldsymbol{S}^p$ are the vectors of h_{mn}, g_b, e_d, and $\Delta S_n^{pt}(\omega)$. And, $\mathcal{F}$ is the occurrence of earthquakes in the payback period. Also, the former three terms in (2.8) are the investment cost, and the last term is the expected multi-time interruption cost over all scenarios. Then, the following constraints are applied:

$$\sum_{\omega\in\Omega} \pi_\omega \sum_{t\in\mathbb{T}} \sum_{n\in\mathbb{N}} p_n \Delta S_n^{pt}(\omega) \le \Delta \overline{S}_{tr}, \tag{2.10}$$

$$0 \le \sum_{b\in\mathbb{B}} g_b \le N_m^g |\mathbb{K}|, \tag{2.11}$$

$$0 \le \sum_{d\in\mathbb{D}} e_d \le N_m^e |\mathbb{E}|, \tag{2.12}$$

$$\Delta \boldsymbol{S}^p(\omega) \in \operatorname{argmin}_{\boldsymbol{\theta},\boldsymbol{\gamma},\boldsymbol{\chi},\boldsymbol{\beta}} \sum_{t\in T} \sum_{n\in\mathbb{N}} p_n \Delta S_n^{pt}(\omega). \tag{2.13}$$

Constraint (2.10) ensures the expected multi-time total loss of load is under a threshold $\Delta\overline{S}_{tr}$. Constraints (2.11)-(2.12) limit the number of MEG and MESS within the maximum number that the PDS can accommodate. Note that $|\mathbb{K}|$ and $|\mathbb{E}|$ represent the numbers of MEG and MESS connection nodes, respectively. Constraint (2.13) implies the upper-level's objective function is restrained by the lower-level's optimal reaction $\Delta \boldsymbol{S}^{p*}$.

2.2.2 Lower-Level PDS Contingency Operation Problem

Given the upper-level representative PDS planning decision $\{\boldsymbol{h}, \boldsymbol{g}, \boldsymbol{e}\}$ and seismic scenario ω, the lower-level problem is formulated as a mixed integer non-linear programming problem. It is used to obtain the contingency operation decisions, including θ_{kb}^{ω}, $\gamma_{se}^{t\omega}$, $\chi_{mn}^{\omega t}$, and β_e^t. Then, the objective is to minimize the multi-time total loss of load, given by

$$\min_{\boldsymbol{\theta},\boldsymbol{\gamma},\boldsymbol{\chi},\boldsymbol{\beta}} \Big\{ \textstyle\sum_{t\in\mathbb{T}} \sum_{n\in\mathbb{N}} p_n \Delta S_n^{pt}(\omega) \Big\}\Big|_{\boldsymbol{h},\boldsymbol{g},\boldsymbol{e},\omega}. \tag{2.14}$$

Also, the following MEG and MESS coordination, power flow, and topology reconfiguration constraints are applied:

$$(2.1)-(2.3), \text{and } \; P_{mnk}^{t\omega}, Q_{mnk}^{t\omega} \leq \upsilon_{nk}^{t\omega} M, \forall k \in \mathbb{K}, \tag{2.15}$$

$$0 \leq V_{nk}^{t\omega} \leq \upsilon_{nk}^{t\omega} M, \forall n \in \mathbb{N}, k \in \mathbb{K}, \tag{2.16}$$

$$-(1-\upsilon_{nk}^{t\omega})M \leq \delta_{nk}^{pt\omega}, \delta_{nk}^{qt\omega} \leq (1-\upsilon_{nk}^{t\omega})M, \forall n \in \mathbb{N}, \tag{2.17}$$

$$0 \leq \delta_{nk}^{Vt\omega} \leq (1-\upsilon_{nk}^{t\omega})(1+\tau)V_0, \forall n \in \mathbb{N}, k \in \mathbb{K}, \tag{2.18}$$

$$\textstyle\sum_{k\in\mathbb{K}} V_{nk}^{t\omega} \leq \sum_{k\in\mathbb{K}} \upsilon_{nk}^{t\omega}(1+\tau)V_0, \forall n \in \mathbb{N}, \tag{2.19}$$

$$\textstyle\sum_{k\in\mathbb{K}} V_{nk}^{t\omega} \geq \sum_{k\in\mathbb{K}} \upsilon_{nk}^{t\omega}(1-\tau)V_0, \forall n \in \mathbb{N}, \tag{2.20}$$

$$S_n^{pt}(\omega) = (1-u_n^{t\omega} \textstyle\sum_{k\in\mathbb{K}} \upsilon_{nk}^{t\omega}) D_n^{pt}, \forall n \in \mathbb{N}, t \in \mathbb{T}, \tag{2.21}$$

$$S_n^{qt}(\omega) = (1-u_n^{t\omega} \textstyle\sum_{k\in\mathbb{K}} \upsilon_{nk}^{t\omega}) D_n^{qt}, \forall n \in \mathbb{N}, t \in \mathbb{T}, \tag{2.22}$$

$$\textstyle\sum_{n|(k,n)\in\mathbb{L}} P_{knk}^{t\omega} + \upsilon_{kk}^{t\omega} D_k^{pt} \leq \sum_{b\in\mathbb{B}} \theta_{kb}^{t\omega} \overline{G}_b^p + E_k^{pt\omega}, \tag{2.23}$$

$$\textstyle\sum_{n|(k,n)\in\mathbb{L}} Q_{knk}^{t\omega} + \upsilon_{kk}^{t\omega} D_k^{qt} \leq \sum_{b\in\mathbb{B}} \theta_{kb}^{t\omega} \overline{G}_b^q + E_k^{qt\omega}, \tag{2.24}$$

$$V_{nk}^{t\omega} = \upsilon_{nk}^{t\omega} V_0, \forall n = k \in \mathbb{K}, t \in \mathbb{T}, \omega \in \Omega, \tag{2.25}$$

$$\epsilon \textstyle\sum_{b\in\mathbb{B}} \theta_{kb}^{\omega} \leq \upsilon_{nk}^{t\omega} \leq \sum_{b\in\mathbb{B}} \theta_{kb}^{\omega}, \forall n = k \in \mathbb{K}, t \in \mathbb{T}, \tag{2.26}$$

$$\textstyle\sum_{k\in\mathbb{K}} \upsilon_{nk}^{t\omega} \leq 1, \forall n \in \mathbb{N}, t \in \mathbb{T}, \tag{2.27}$$

$$\upsilon_{nk}^{t\omega} \leq \upsilon_{mk}^{t\omega}, \forall m \in \mathbb{N}, n \in \mathbb{N}_{ch}(m), \omega \in \Omega, \tag{2.28}$$

$$0 \leq \textstyle\sum_{k\in\mathbb{K}} \theta_{kb}^{\omega} \leq g_b, \forall b \in \mathbb{B}, \omega \in \Omega, \tag{2.29}$$

$$0 \leq \textstyle\sum_{s\in\mathbb{S}} \psi_{sd}^{\omega} \leq e_d, \forall d \in \mathbb{D}, \omega \in \Omega, \tag{2.30}$$

$$0 \leq \textstyle\sum_{b\in\mathbb{B}} \theta_{kb}^{\omega} \leq N_m^g, \forall k \in \mathbb{K}, \omega \in \Omega, \tag{2.31}$$

$$0 \leq \sum_{s\in\mathbb{S}} \gamma_{se}^{t\omega} \leq N_m^e, \forall e \in \mathbb{E}, t \in \mathbb{T}, \omega \in \Omega, \tag{2.32}$$

$$\sum_{e\in\mathbb{E}} \gamma_{se}^{t=1,\omega} \leq \sum_{d\in\mathbb{D}} \psi_{sd}^{\omega}, \forall s \in \mathbb{S}, \omega \in \Omega, \tag{2.33}$$

$$\sum_{e\in\mathbb{E}} \gamma_{se}^{t=1,\omega} = \sum_{e\in\mathbb{E}} \gamma_{se}^{t>1,\omega}, \forall s \in \mathbb{S}, \omega \in \Omega, \tag{2.34}$$

$$E_e^{pt\omega} = \sum_{s\in\mathbb{S}} \hat{E}_{se}^{pt\omega} - \sum_{s\in\mathbb{S}} \check{E}_{se}^{pt\omega}, \forall e \in \mathbb{E}, t \in \mathbb{T}, \tag{2.35}$$

$$\sum_{s\in\mathbb{S}} \hat{E}_{se}^{pt\omega} \leq \beta_e^t M, \forall e \in \mathbb{E}, t \in \mathbb{T}, \tag{2.36}$$

$$\sum_{s\in\mathbb{S}} \check{E}_{se}^{pt\omega} \leq (1-\beta_e^t)M, \forall e \in \mathbb{E}, t \in \mathbb{T}, \tag{2.37}$$

$$\gamma_{se'}^{t\omega} \leq \zeta_{ee'}^{t\omega} \gamma_{se}^{t-1,\omega}, \forall s \in \mathbb{S}, e, e' \in \mathbb{E}, t \in \mathbb{T}, \tag{2.38}$$

$$\begin{aligned} &\hat{E}_{se}^{pt\omega}/\eta^{dis} \leq \sum_{d\in\mathbb{D}} \psi_{sd}^{\omega} \overline{E}_d^{dis} - t_{e'e} \sum_{d\in\mathbb{D}} \psi_{sd}^{\omega} \overline{E}_d^{dis} \\ &+(2-\gamma_{se'}^{t-1,\omega} - \gamma_{se}^{t\omega})M, \forall s \in \mathbb{S}, e', e \in \mathbb{E}, t \in \mathbb{T}, \end{aligned} \tag{2.39}$$

$$\begin{aligned} &\hat{E}_{se}^{pt\omega}\eta^{ch} \leq \sum_{d\in\mathbb{D}} \psi_{sd}^{\omega} \overline{E}_d^{ch} - t_{e'e} \sum_{d\in\mathbb{D}} \psi_{sd}^{\omega} \overline{E}_d^{ch} \\ &+(2-\gamma_{se'}^{t-1,\omega} - \gamma_{se}^{t\omega})M, \forall s \in \mathbb{S}, e', e \in \mathbb{E}, t \in \mathbb{T}, \end{aligned} \tag{2.40}$$

$$0 \leq \hat{E}_{se}^{pt\omega}/\eta^{dis}, \check{E}_{se}^{pt\omega}\eta^{ch} \leq \gamma_{se}^{t\omega} M, \forall s \in \mathbb{S}, e \in \mathbb{E}, t \in \mathbb{T}, \tag{2.41}$$

$$\hat{E}_{se}^{pt\omega}/\eta^{dis} \leq \sum_{d\in\mathbb{D}} \psi_{sd}^{\omega} \overline{E}_d^{dis}, \forall s \in \mathbb{S}, e \in \mathbb{E}, t \in \mathbb{T}, \tag{2.42}$$

$$\hat{E}_{se}^{pt\omega}\eta^{ch} \leq \sum_{d\in\mathbb{D}} \psi_{sd}^{\omega} \overline{E}_d^{ch}, \forall s \in \mathbb{S}, e \in \mathbb{E}, t \in \mathbb{T}, \tag{2.43}$$

$$\eta^{min} \sum_{d\in\mathbb{D}} \psi_{sd}^{\omega} \overline{E}_d \leq \widetilde{E}_s^{t\omega} \leq \eta^{max} \sum_{d\in\mathbb{D}} \psi_{sd}^{\omega} \overline{E}_d \tag{2.44}$$

$$\widetilde{E}_s^{t=1,\omega} = \eta^{ini} \sum_{d\in\mathbb{D}} \psi_{sd}^{\omega} \overline{E}_d, \forall s \in \mathbb{S}, \omega \in \Omega, \tag{2.45}$$

$$\widetilde{E}_s^{t+1,\omega} = \widetilde{E}_s^{t,\omega} + \sum_{e\in\mathbb{E}} \check{E}_{se}^{pt\omega}\eta^{ch} - \sum_{e\in\mathbb{E}} \hat{E}_{se}^{pt\omega}/\eta^{dis}, \tag{2.46}$$

$$-\check{E}_{sn}^{pt\omega} K \leq \check{E}_{sn}^{qt\omega} \leq \check{E}_{sn}^{pt\omega} K, \forall s \in \mathbb{S}, n \in \mathbb{N}, \tag{2.47}$$

$$-\hat{E}_{sn}^{pt\omega} K \leq \hat{E}_{sn}^{qt\omega} \leq \hat{E}_{sn}^{pt\omega} K, \forall s \in \mathbb{S}, n \in \mathbb{N}, \tag{2.48}$$

$$v_{nk}^{t\omega} \leq \chi_{mn}^{\omega}(1 - \xi_{mn}^{\omega} + r_{mn}^{t\omega}), \forall m \in \mathbb{N}, n \in \mathbb{N}_{ch}(m). \tag{2.49}$$

Constraints (2.15)-(2.16) force $P_{mnk}^{t\omega}$, $Q_{mnk}^{t\omega}$, and $V_{nk}^{t\omega}$ to 0, if node n is not restored by MEG connection node k. Constraints (2.17)-(2.18) enable the slack variables

$\delta_{nk}^{pt\omega}$, $\delta_{nk}^{qt\omega}$, $\delta_{nk}^{Vt\omega}$ such that Constraints (2.1)-(2.3) can be feasible. Constraints (2.19)-(2.20) limit the nodal voltages within an acceptable range by tolerance τ. Constraints (2.21)-(2.22) ensure that a load can be restored only when this load belongs to a microgrid and the corresponding load switch is on. For linearization, we replace the quadratic term $u_n^{t\omega} \sum_{k\in\mathbb{K}} v_{nk}^{t\omega}$ with $u_n^{t\omega}$, and add an additional constraint $u_n^{t\omega} \leq \sum_{k\in\mathbb{K}} v_{nk}^{t\omega}$. Constraints (2.23)-(2.24) ensure that the power injected into each microgrid is within the generation capacity of the MEGs deployed at the root node. Constraint (2.25) means the voltages of the root nodes are set to the reference voltage V_0. Constraint (2.26) ensures the root node can be energized only when there are MEGs deployed at this node. Constraint (2.27) means that a node can be energized by only one microgrid at a time. Constraint (2.28) means that a child node can be energized only when its parent is energized. Constraints (2.29)-(2.30) mean that the MEGs and MESSs can be used only when they are invested. Constraints (2.31)-(2.32) limit the total number of MEGs and MESSs that each MEG and MESS connection node can accommodate. Constraints (2.33)-(2.34) mean that a MESS must be deployed at one certain node at one time t. Constraints (2.35)-(2.37) are to calculate the total MESS injected or consumed power ($E_e^{pt\omega}$) at MESS connection node e. Constraint (2.38) means that if the road between MESS connection node e and e' is damaged during time t, then no MESS can be transported to node e' through this road. Constraints (2.39)-(2.40) restrict the maximum charging and discharging power of MESSs at each time t. When $\gamma_{se'}^{t-1,\omega} = 1$ and $\gamma_{se}^{t\omega} = 1$, it means that the s_{th} MESS is transported to MESS connection node e' from e during time t. Then, the charging and discharging power during the lag time of transportation $t_{e'e}$ should be deducted. Constraint (2.41) ensures there is no charging or discharging, if no MESS is deployed at MESS connection node e. Constraints (2.42)-(2.43) are to restrict the maximum charging and discharging power of MESSs by the rated power $\overline{E}_d^{dis}$ and $\overline{E}_d^{ch}$. Constraint (2.44) limits the State of Charge (SOC) such that no over-charging or over-discharging will occur. Constraint (2.45) specifies the initial SOC by η^{ini}. Constraint (2.46) calculates the SOC of MESS at each time t. Constraints (2.47)-(2.48) limit the reactive power of MESS by factor K. Constraint (2.49) is non-linear. It means that a child node n can not be energized by the MG in which its parent node m is, when the line switch (m, n) is opened, or DL (m, n) is damaged but not repaired. For linearization, we introduce an auxiliary variable $\ddot{a}^{\omega}_{mn}$, then constraint (2.49) can be replaced by $\ddot{a}^{\omega}_{mn} \leq 1 - \xi^{\omega}_{mn} + r^{t\omega}_{mn}$, $\ddot{a}^{\omega}_{mn} \leq \chi^{\omega}_{mn}$, $\ddot{a}^{\omega}_{mn} \geq \chi^{\omega}_{mn} + (1 - \xi^{\omega}_{mn} + r^{t\omega}_{mn}) - 1$, and $v^{\omega}_{nk} \leq \ddot{a}^{\omega}_{mn}$.

2.2.3 Complete Stochastic Resilient PDS Planning Problem

Based on the upper- and the lower-level problems, the risk-neutral version of SRD-SPP can be represented as follows:

$$\begin{aligned} \min\nolimits_{\boldsymbol{\vartheta}_u} \mathbb{F}(\boldsymbol{\vartheta}_u) = \min\nolimits_{\boldsymbol{\vartheta}_u} \big\{\mathbb{E}_{\omega}\big\{ \min\nolimits_{\Delta \boldsymbol{S}^p(\omega)} c_s \textstyle\sum_{t,n} \Delta S^{pt}_n(\omega) \\ \big|\Delta \boldsymbol{S}^p(\omega) \in \Psi(\boldsymbol{\vartheta}_u, \omega)\big\} + \mathcal{C}_p^{\top} \boldsymbol{\vartheta}_u\big\} \big| \mathbb{G}_u(\boldsymbol{\vartheta}_u, \omega) \leq 0\big\}, \end{aligned} \tag{2.50}$$

where $\mathcal{C}_p$, and $\boldsymbol{\vartheta}_u \in \mathcal{H} \times \mathcal{G} \times \mathcal{E}$ are the joint investment cost, and the upper-level planning decision vector, respectively. The lower-level's optimal reaction set mapping Ψ can be defined:

$$\Psi \triangleq \operatorname{argmin}_{\boldsymbol{\vartheta}_l} \mathbb{E}_{\omega}\{\textstyle\sum_{t,n} p_n \Delta S^{pt}_n(\omega) | \mathbb{G}_l(\boldsymbol{\vartheta}_l, \omega) \leq 0\}, \tag{2.51}$$

where $\boldsymbol{\vartheta}_l$ denotes the lower-level contingency operation decision vector. Then, by considering the mean upper semideviation risk measure [106], the SRDSPP can be derived as

$$\min\nolimits_{\boldsymbol{\vartheta}_u} \{\mathbb{F}(\boldsymbol{\vartheta}_u) + \rho \mathbb{E}_{\omega^\star} \max\{0, \mathbb{F}_d(\boldsymbol{\vartheta}_u, \omega^\star) - \mathbb{F}(\boldsymbol{\vartheta}_u)\}\}, \tag{2.52}$$

$$\begin{aligned} \mathbb{F}_d(\boldsymbol{\vartheta}_u, \omega^\star) = \big\{\mathcal{C}_p^{\top} \boldsymbol{\vartheta}_u + \min\nolimits_{\Delta \boldsymbol{S}^p(\omega^\star)} \big\{c_s \textstyle\sum_{t,n} \Delta S^{pt}_n(\omega^\star) \\ \big|\Delta \boldsymbol{S}^p(\omega^\star) \in \Psi(\boldsymbol{\vartheta}_u, \omega^\star)\big\} \big| \mathbb{G}_u(\boldsymbol{\vartheta}_u, \omega^\star) \leq 0\big\}, \end{aligned} \tag{2.53}$$

where $\mathbb{F}_d(\boldsymbol{\vartheta}_u, \omega^\star)$ is $\mathbb{F}(\boldsymbol{\vartheta}_u)$ under a sampled scenario $\omega^\star \in \Omega$. Note that the first term of equation (2.52) is the total mean cost, and the second term represents the risk. It can be deemed as a multi-objective programming with risk weighted by $\rho \in [0, 1]$, which penalizes an excess of $\mathbb{F}_d(\boldsymbol{\vartheta}_u, \omega^\star)$ over its mean. In this research, the risk refers to the risk of experiencing seismic scenarios with high cost. Then, parameter ρ represents the significance of the risk measure. It depends on the will of a system planner to take the risk. A conservative system planner would like to minimize the risk, hence a larger ρ should be selected to increase the weight of the risk in equation (2.52). However, for a system planner who want to minimize the

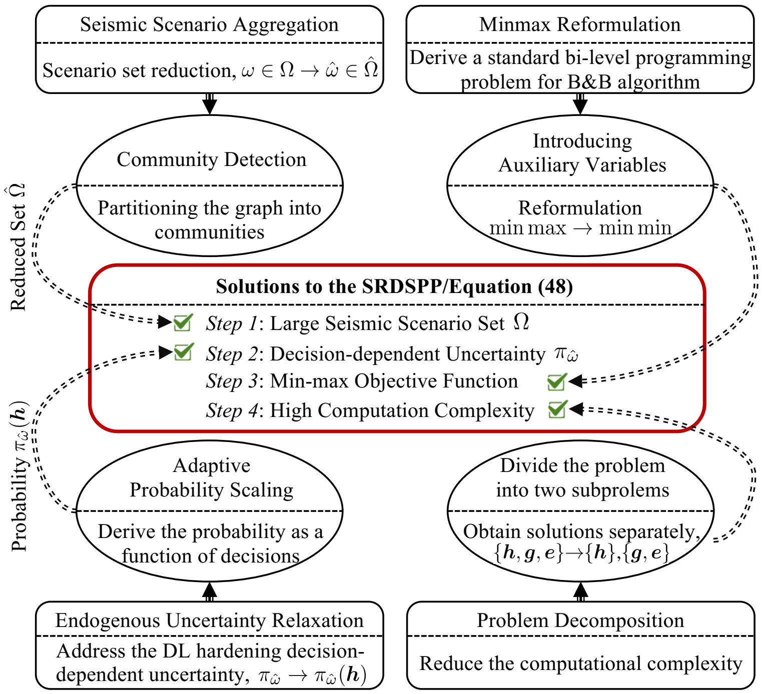

Figure 2.2: An illustration of the solution procedures of the SRDSPP.

cost with little consideration of the risk, a smaller ρ is preferred.

2.3 Stochastic Resilient PDS Planning Problem Solution

As shown in Fig. 2.2, the solution procedure to the SRDSPP consists of four steps. First of all, as the increasing number of seismic scenarios can result in heavy computational burden, scenario reduction is necessary. To this end, a seismic scenario aggregation method is proposed based on graph theory and community detection, such that the seismic scenario set Ω can be replaced by a reduced subset $\hat{\Omega} \subset \Omega$. Second, to address the DL hardening decision-dependent uncertainty, an endogenous uncertainty relaxation method is proposed. It can achieve an adaptive scenario probability scaling with the variation of DL hardening decision, i.e., $\pi_{\omega}(\boldsymbol{h})$. Third, the SRDSPP with $\min\max$ form is reformulated into a standard bi-level programming problem with $\min\min$ form. Then, it can be solved by the Branch-and-Bound (B&B) algorithm [107]. Finally, to reduce the computation complexity, a decomposition method is proposed. It can break up the original problem into two sub-problems, so that the DL hardening decision ($\boldsymbol{h}$), and the MEG and MESS investment decisions ($\boldsymbol{g}$ and $\boldsymbol{e}$) can be optimized separately. In this section, the solutions will be presented.

2.3.1 Seismic Scenario Aggregation

Based on graph theory and community detection, the seismic scenario set Ω can be replaced with a reduced subset $\hat{\Omega}$ to reduce the computation burden. Next, we present the procedure of the seismic scenario aggregation method.

1) Graph Generation: To capture the pairwise relationship of seismic scenarios, we firstly generate a weighted undirected graph without self-loops. Specifically, each vertex represents a seismic scenario ω, and the weight of each edge indicates the correlation of the pairwise scenarios. Then, an adjacency matrix $\mathcal{A}$ of the graph can be developed as follows:

$$\mathcal{A}_{ij} = N_s(\boldsymbol{\xi}^{\omega}, \boldsymbol{\xi}^{\omega'})/\max\{N(\boldsymbol{\xi}^{\omega}), N(\boldsymbol{\xi}^{\omega'})\}, \tag{2.54}$$

where $N_s(\boldsymbol{\xi}^{\omega}, \boldsymbol{\xi}^{\omega'})$ is the number of identical damaged DLs in $\boldsymbol{\xi}^{\omega}$ and $\boldsymbol{\xi}^{\omega'}$, and $N(\boldsymbol{\xi}^{\omega})$ represents the number of damaged DLs in $\boldsymbol{\xi}^{\omega}$. It means that the higher the similarity of damaged DLs between ω and ω' is, the more correlation of this pairwise scenario should be, and the larger the element $\mathcal{A}_{ij}$ will be.

2) Community detection: Community detection is a process of partitioning the graph into communities [108]. The quality of this can be measured by the metric modularity, given by

$$Q = \frac{1}{2m} \sum\nolimits_{i,j} [\mathcal{A}_{ij} - \frac{k_i k_j}{2m}] \delta(C_i, C_j), \tag{2.55}$$

where $k_i = \sum_j \mathcal{A}_{ij}$ denotes the sum of edge weight attached to vertex i, and $m = \frac{1}{2} \sum_{i,j} \mathcal{A}_{ij}$ is the total edge weight in the graph. The Kronecker δ-function $\delta(C_i, C_j) = 1$ when $C_i = C_j$. Then, the Louvain algorithm is applied, which in the first-phase greedily maximizes gain in modularity by

$$\Delta Q_{i \to C_j} = w_{i \to C_j}/2m - \textstyle\sum_{tot}^{C_j} \times w_i/2m^2, \tag{2.56}$$

where $w_{i \to C_j}$ represents the sum of edge weights from vertex i to vertices in community C_j, w_i is the sum of edge weights incident to vertex i, and $\sum_{tot}^{C_j}$ denotes the sum of weights from edges incident to any vertex in community C_j. Then, all the vertices will be evaluated until no further gain in modularity can be obtained. Next, the second-phase builds up a new graph based on communities discovered in the first-phase. The two phases iteratively continue until the number of communities is lower than a predefined number of scenarios limit N_C.

3) Centroid Identification: Once the communities are detected, the seismic scenarios can then be clustered. The centroid of each community can be identified based on the graph density and connectivity [109]. In this work, we will choose the vertex with the largest sum of edge weights attached to it, expressed by $i^* = \mathrm{argmax}_i \sum_j \mathcal{A}_{ij}, C_i = C_j$. Then, the reduced scenario set becomes $\hat{\Omega} \subset \Omega$, and the centroids form the representative seismic scenarios $\hat{\omega} \in \hat{\Omega}$.

2.3.2 Endogenous Uncertainty Relaxation

As aforementioned in Subsection 2.1.3, the seismic scenario uncertainty is decision-dependent, if seismic design PDSs with hardened DLs are considered. Specifically, the probabilities of occurrence $\pi_{\hat{\omega}}$ vary with the DL hardening decision $\boldsymbol{h}$, i.e., $\pi_{\hat{\omega}}(\boldsymbol{h})$. In this regard, we propose an endogenous uncertainty relaxation method to achieve an adaptive scenario probability scaling. Firstly, we perform 'bitwise AND operation' on vector $\boldsymbol{h}$ and $\boldsymbol{\xi}^{\hat{\omega}}$, i.e., $\boldsymbol{\mathcal{D}}^{\hat{\omega}} = \boldsymbol{h} \wedge \boldsymbol{\xi}^{\hat{\omega}}$, to locate the hardened DLs but damaged. Then, the probability of scenario which contains damaged hardened DLs $\pi_{\hat{\omega}}, \hat{\omega} \in \hat{\Omega}_h$ can be given by

$$\pi_{\hat{\omega}}(\boldsymbol{h}) = (1 - \mathcal{I}(\boldsymbol{l}^\top \boldsymbol{\mathcal{D}}^{\hat{\omega}} / \boldsymbol{l}^\top \boldsymbol{\xi}^{\hat{\omega}}))\pi_{\hat{\omega}}, \hat{\omega} \in \hat{\Omega}_h, \tag{2.57}$$

which means the more damaged hardened DLs that a scenario contains, the more corresponding probability will be scaling down. Note that $\mathcal{I} \leq 1$ denotes a seismic design improvement factor. Moreover, the probability of scenario where all DLs are standard designed $\pi_{\hat{\omega}}$, $\hat{\omega} \in \hat{\Omega}_s$ can be derived as

$$\pi_{\hat{\omega}}(\boldsymbol{h}) = (1 - \textstyle\sum_{\hat{\omega}' \in \hat{\Omega}_h} \pi_{\hat{\omega}'}(\boldsymbol{h})) / (\textstyle\sum_{\hat{\omega}' \in \hat{\Omega}_s} \pi_{\hat{\omega}'}) \pi_{\hat{\omega}}, \hat{\omega} \in \hat{\Omega}_s, \tag{2.58}$$

where $\sum_{\hat{\omega} \in \hat{\Omega}} \pi_{\hat{\omega}}(\boldsymbol{h}) = 1$ and $\hat{\Omega}_s \cap \hat{\Omega}_h = \emptyset$. Then, by replacing $\pi_{\hat{\omega}}$ with $\pi_{\hat{\omega}}(\boldsymbol{h})$ (denoted as $\pi_{\hat{\omega}}^{\boldsymbol{h}}$), the endogenous uncertainty relaxation of $\mathbb{F}$ can be equivalently obtained as

$$\mathbb{F} = \big\{\mathcal{C}_p^\top \boldsymbol{\vartheta}_u + \big\{ \textstyle\sum_{\hat{\omega}\in\hat{\Omega}} \pi_{\hat{\omega}}^{\boldsymbol{h}} \min_{\Delta \boldsymbol{S}^p(\hat{\omega})} c_s \sum_{t,n} \Delta S_n^{pt}(\hat{\omega}) \\ \big|\Delta \boldsymbol{S}^p(\hat{\omega}) \in \Psi(\boldsymbol{\vartheta}_u, \hat{\omega})\big\}\big|\mathbb{G}_u(\boldsymbol{\vartheta}_u, \hat{\omega}) \leq 0\big\}, \tag{2.59}$$

where the sampling average approximation is applied by replacing the second-stage $\mathbb{E}_{\hat{\omega}}\{\min_{\Delta \boldsymbol{S}^p(\hat{\omega})} c_s \sum_{t,n} \Delta S_n^{pt}(\hat{\omega})\}$ with $\sum_{\hat{\omega}\in\hat{\Omega}} \pi_{\hat{\omega}}^{\boldsymbol{h}} \min_{\Delta \boldsymbol{S}^p(\hat{\omega})} c_s \sum_{t,n} \Delta S_n^{pt}(\hat{\omega})$ [110].

2.3.3 Reformulation of the SRDSPP

To solve the SRDSPP with $\min\max$ form, given in equation (2.52), by the B&B algorithm, we reformulate it into a standard bi-level programming problem with $\min\min$ form as follows,

Theorem 2.1. The proposed SRDSPP in equation (2.52) can be equivalently rewritten as the following $\min\min$ form:

$$\min_{\boldsymbol{\vartheta}_u} \big\{\mathcal{C}_p^\top \boldsymbol{\vartheta}_u + \min_{\Delta \boldsymbol{S}^p, \boldsymbol{\lambda}_{\hat{\omega}}} \big\{(1-\rho) \sum_{\hat{\omega}\in\hat{\Omega}} \pi_{\hat{\omega}}^{\boldsymbol{h}} c_s \sum_{t,n} \Delta S_n^{pt}(\hat{\omega}) \\ + \rho \textstyle\sum_{\hat{\omega}\in\hat{\Omega}} \pi_{\hat{\omega}}^{\boldsymbol{h}} \lambda_{\hat{\omega}} \big|(\Delta \boldsymbol{S}^p(\hat{\omega}), \boldsymbol{\lambda}_{\hat{\omega}}) \in \Psi_D\big\}\big|\mathbb{G}_u \leq 0\big\}, \tag{2.60}$$

$$\Psi_D \triangleq \operatorname{argmin}_{\Delta \boldsymbol{S}^p, \boldsymbol{\lambda}_{\hat{\omega}}} \big\{ \textstyle\sum_{\hat{\omega}\in\hat{\Omega}} \sum_{t,n} p_n \Delta S_n^{pt}(\hat{\omega}) \big| \tag{2.61}$$

$$\lambda_{\hat{\omega}} \geq c_s \sum_{t,n} \Delta S_n^{pt}(\hat{\omega}), \lambda_{\hat{\omega}} \geq \sum_{\hat{\omega}'\in\hat{\Omega}} \pi_{\hat{\omega}'}^{\boldsymbol{h}} c_s \sum_{t,n} \Delta S_n^{pt}(\hat{\omega}), \mathbb{G}_l \leq 0\}.$$

Proof: By introducing auxiliary variable $\lambda_{\hat{\omega}}$ into the risk-averse SRDSPP, *Theorem 1* can be derived as follows,

$$\mathbb{F}(\boldsymbol{\vartheta}_u) + \rho \mathbb{E}_{\hat{\omega}} \max\{0, \mathbb{F}_d(\boldsymbol{\vartheta}_u, \hat{\omega}) - \mathbb{F}(\boldsymbol{\vartheta}_u)\} = \tag{2.62}$$

$$\mathbb{F}(\boldsymbol{\vartheta}_u) + \rho \textstyle\sum_{\hat{\omega}\in\hat{\Omega}} \pi_{\hat{\omega}}^{\boldsymbol{h}} \max\{0, \mathbb{F}_d(\boldsymbol{\vartheta}_u, \hat{\omega}) - \mathbb{F}(\boldsymbol{\vartheta}_u)\} = \tag{2.63}$$

$$(1-\rho)\mathbb{F}(\boldsymbol{\vartheta}_u) + \rho \textstyle\sum_{\hat{\omega}\in\Omega} \pi_{\hat{\omega}}^{\boldsymbol{h}} \max\{\mathbb{F}(\boldsymbol{\vartheta}_u), \mathbb{F}_d(\boldsymbol{\vartheta}_u, \hat{\omega})\} = \tag{2.64}$$

$$(1-\rho)\mathbb{F} + \rho \mathcal{C}_p^\top \boldsymbol{\vartheta}_u + \rho \sum_{\hat{\omega}\in\Omega} \pi_{\hat{\omega}}^{\boldsymbol{h}} \min_{\boldsymbol{\lambda}} \left\{ \begin{array}{c} \lambda_{\hat{\omega}} - \mathcal{C}_p^\top \boldsymbol{\vartheta}_u \\ s.t. \lambda_{\hat{\omega}} \geq \mathbb{F}, \lambda_{\hat{\omega}} \geq \mathbb{F}_d \end{array} \right\} = \tag{2.65}$$

$$\mathcal{C}_p^\top \boldsymbol{\vartheta}_u + (1-\rho) \sum_{\hat{\omega}\in\hat{\Omega}} \pi_{\hat{\omega}}^{\boldsymbol{h}} \big\{ \min_{\Delta \boldsymbol{S}^p(\hat{\omega})} c_s \sum_{t,n} \Delta \boldsymbol{S}_n^{pt}(\hat{\omega}) \big| \Delta \boldsymbol{S}^p(\hat{\omega}) \in \Psi \big\} +$$

$$\min_{\boldsymbol{\lambda}} \left\{ \rho \sum_{\hat{\omega}\in\hat{\Omega}} \pi_{\hat{\omega}}^{\boldsymbol{h}} \lambda_{\hat{\omega}} \middle| \begin{array}{l} \lambda_{\hat{\omega}} \geq \min_{\Delta \boldsymbol{S}^p(\hat{\omega})} \{c_s \sum_{t,n} \Delta \boldsymbol{S}_n^{pt}(\hat{\omega})\}, \\ \lambda_{\hat{\omega}} \geq \sum_{\hat{\omega}\in\hat{\Omega}} \pi_{\hat{\omega}}^{\boldsymbol{h}} \{ \min_{\Delta \boldsymbol{S}^p(\hat{\omega})} c_s \sum_{t,n} \Delta \boldsymbol{S}_n^{pt}(\hat{\omega})\} \end{array} \right\} = \tag{2.66}$$

$$\mathcal{C}_p^\top \boldsymbol{\vartheta}_u + \min_{\Delta \boldsymbol{S}^p, \boldsymbol{\lambda}_{\hat{\omega}}} \Bigg\{ (1-\rho) \textstyle\sum_{\hat{\omega}\in\hat{\Omega}} \pi_{\hat{\omega}}^{\boldsymbol{h}} c_s \sum_{t,n} \Delta \boldsymbol{S}_n^{pt}(\hat{\omega}) \tag{2.67}$$

$$+\rho \textstyle\sum_{\hat{\omega}\in\hat{\Omega}} \pi_{\hat{\omega}}^{\boldsymbol{h}} \lambda_{\hat{\omega}} \Bigg| \begin{array}{l} \Delta \boldsymbol{S}^p \in \Psi, \lambda_{\hat{\omega}} \geq c_s \sum_{t,n} \Delta S_n^{pt}(\hat{\omega}), \\ \lambda_{\hat{\omega}} \geq \sum_{\hat{\omega}' \in \Omega} \pi_{\hat{\omega}'}^{\boldsymbol{h}} c_s \sum_{t,n} \Delta S_n^{pt}(\hat{\omega}) \end{array} \Bigg\}. \ \square$$

Also, (2.60) and (2.61) can be further simplified as

$$\min\nolimits_{\boldsymbol{\vartheta}_u} \left\{ \mathcal{C}_p^\top \boldsymbol{\vartheta}_u + \min\nolimits_{\boldsymbol{\vartheta}_l'} \left\{ K^\top \boldsymbol{\vartheta}_l' \middle| \boldsymbol{\vartheta}_l' \in \Psi_D \right\} \middle| \boldsymbol{\vartheta}_u \in \mathcal{V}_u \right\}, \tag{2.68}$$

$$\Psi_D = \mathrm{argmin}_{\boldsymbol{\vartheta}_l'} \left\{ T^\top \boldsymbol{\vartheta}_l' \middle| W \boldsymbol{\vartheta}_l' \leq B \boldsymbol{\vartheta}_u + b \right\}. \tag{2.69}$$

Theorem 2.2. If $\Psi(\boldsymbol{\vartheta}_u)$ is non-empty for any $\boldsymbol{\vartheta}_u \in \mathcal{V}_u$, the following conditions hold: a) Equation (2.64) can be equivalently rewritten as

$$\min\nolimits_{\boldsymbol{\vartheta}_u, \vartheta_l'} \left\{ \mathcal{C}_p^\top \boldsymbol{\vartheta}_u + K^\top \boldsymbol{\vartheta}_l' \middle| \boldsymbol{\vartheta}_u \in \mathcal{V}_u, \boldsymbol{\vartheta}_l' \in \Psi_D \right\}, \tag{2.70}$$

and the optimal values of (2.68) and (2.70) coincide; b) $\boldsymbol{\vartheta}_u^*$ is a global optimum of (2.68) iff $\exists \boldsymbol{\vartheta}_l'^* \in \mathcal{V}_l'$ such that $(\boldsymbol{\vartheta}_u^*, \boldsymbol{\vartheta}_l'^*)$ is a global optimum of (2.70); c) $\boldsymbol{\vartheta}_u^*$ is a local optimum of (2.68) iff $\exists \boldsymbol{\vartheta}_l'^* \in \mathcal{V}_l'$ such that $(\boldsymbol{\vartheta}_u^*, \boldsymbol{\vartheta}_l'^*)$ is a local optimum of (2.70).

Proof: By assumption, the mapping $\mathbb{S}$: $\boldsymbol{\vartheta}_u \mapsto \mathbb{R}$, $\mathbb{S} \triangleq \min_{\boldsymbol{\vartheta}_l'} \left\{ K^\top \boldsymbol{\vartheta}_l' \middle| \boldsymbol{\vartheta}_l' \in \Psi_D(\boldsymbol{\vartheta}_u) \right\}$ is well defined, which means that $\forall \boldsymbol{\vartheta}_u \in \mathcal{V}_u$, $\exists \boldsymbol{\vartheta}_l' \in \mathcal{V}_l'$ such that $K^\top \boldsymbol{\vartheta}_l' = \mathbb{S}(\boldsymbol{\vartheta}_u)$. Furthermore, $\forall \boldsymbol{\vartheta}_l' \in \Psi(\boldsymbol{\vartheta}_u)$, $\mathbb{S}(\boldsymbol{\vartheta}_u) \leq K^\top \boldsymbol{\vartheta}_l'$ always holds. $\square$

2.3.4 Decomposition of the SRDSPP

The SRDSPP can be solved by first specifying the planning decision $\boldsymbol{\vartheta}_u$ and fixing $\pi_{\hat{\omega}}^{\boldsymbol{h}}$ using exhaustive search algorithm, then optimizing the lower-level problem, and finally evaluating the upper-level objective. The computational complexity is $\mathcal{O}(2^{|\mathbb{L}|}(N_m^g|\mathbb{K}|)^{|\mathbb{B}|}(N_m^e|\mathbb{E}|)^{|\mathbb{D}|})$, where $|\mathbb{L}|$ denotes the number of DLs, and $|\mathbb{B}|$ and $|\mathbb{D}|$ represent the number of types of MEG and MESS, respectively. It is time-consuming especially when the solution space is large, e.g., a large PDS with high penetration of MEGs and MESSs. To reduce the computational burden, inspired by [111], we propose a decomposition method, in which the SRDSPP is broken up into two subproblems (1) and (2). Subproblem (1) is to obtain the lower bound of the multi-time total loss of load $\sum_{t,n} p_n \Delta S_n^{pt}(\hat{\omega})$, and derive the optimal DL hardening decision $\boldsymbol{h}^*$. Then, subproblem (2) determines the optimal MEG and MESS portfolio $\boldsymbol{g}^*$ and $\boldsymbol{e}^*$, given $\boldsymbol{h}^*$. Specifically, subproblem (1) is to determine the DL hardening decision $\boldsymbol{h}$, which minimizes the hardening investment cost and the expected interruption cost, given by

$$\begin{aligned}\min_{\boldsymbol{h},\Delta\boldsymbol{S}^p,\boldsymbol{\lambda}} & \Big\{c_h\boldsymbol{\ell}^\top\boldsymbol{h} + \Big\{(1-\rho)\textstyle\sum_{\hat{\omega}\in\hat{\Omega}}\pi_{\hat{\omega}}^{\boldsymbol{h}}c_s\sum_{t,n}\Delta S_n^{pt}(\hat{\omega}) \\ & + \rho\textstyle\sum_{\hat{\omega}\in\hat{\Omega}}\pi_{\hat{\omega}}^{\boldsymbol{h}}\lambda_{\hat{\omega}}\Big|(10),(\Delta\boldsymbol{S}^p(\hat{\omega}),\boldsymbol{\lambda})\in\Psi_h\Big\},\end{aligned} \tag{2.71}$$

$$\begin{aligned}\Psi_h \triangleq \operatorname{argmin}_{\boldsymbol{v},\Delta\boldsymbol{S}^p} & \Big\{\textstyle\sum_{\hat{\omega}\in\hat{\Omega}}\sum_{t,n}p_n\Delta S_n^{pt}(\hat{\omega})\Big| \\ & (26),(27),\lambda_{\hat{\omega}} \geq \textstyle\sum_{\hat{\omega}'\in\hat{\Omega}}\pi_{\hat{\omega}'}^{\boldsymbol{h}}c_s\sum_{t,n}\Delta S_n^{pt}(\hat{\omega}), \\ & \lambda_{\hat{\omega}} \geq c_s\textstyle\sum_{t,n}\Delta S_n^{pt}(\hat{\omega}), v_{nk}^{\hat{\omega}}=1, n=k, \forall k\in\mathbb{K}\Big\}.\end{aligned} \tag{2.72}$$

Then, subproblem (2) is to obtain the minimum investment cost of MEGs and MESSs, which can lead to the same amount of restored loads as subproblem (1), given $\boldsymbol{h}^*$, stated by

$$\min_{\boldsymbol{g},\boldsymbol{e}}\big\{\boldsymbol{c}_g^\top\boldsymbol{g}+\boldsymbol{c}_e^\top\boldsymbol{e}\big\}|_{\boldsymbol{h}^*,\Delta\boldsymbol{S}^{p*}}, \tag{2.73}$$

subject to: constraints (2.1)-(2.3), (2.10)-(2.12), and (2.15)-(2.49).

Theorem 2.3. Assuming $\exists\boldsymbol{h}\in\mathcal{H}$, $\boldsymbol{g}\in\mathcal{G}$ and $\boldsymbol{e}\in\mathcal{E}$, such that $\Psi_D\neq\emptyset$, then the optimal planning decisions $\boldsymbol{h}^*$, $\boldsymbol{g}^*$, $\boldsymbol{e}^*$ in (2.71) and (2.73) agree with that of (2.70).

Proof: a) Since isolated islands without MEG connection nodes can not get access to the emergency power, then for any $\boldsymbol{g}\in\mathcal{G}$, $\boldsymbol{e}\in\mathcal{E}$, the lower bound of $\sum_{\hat{\omega}\in\hat{\Omega}}\pi_{\hat{\omega}}^{\boldsymbol{h}}\sum_{t,n}p_n\Delta S_n^{pt}(\hat{\omega})$, denoted as $\underline{lol}$, only depends on $\boldsymbol{h}$. Thereby, to ensure $\underline{lol}\leq\Delta\overline{S}_{tr}$, $\boldsymbol{h}$ can be separately optimized by (2.71); b) Given $\boldsymbol{h}^*$, the upper bound of $\sum_{\hat{\omega}\in\hat{\Omega}}\pi_{\hat{\omega}}^{\boldsymbol{h}^*}\sum_{t,n}p_n\Delta S_n^{pt}(\hat{\omega})$, denoted as $\overline{lol}$, only depends on $\boldsymbol{g}$, $\boldsymbol{e}$, which means $\lim_{\boldsymbol{g},\boldsymbol{e}\to\boldsymbol{g}^*,\boldsymbol{e}^*}\overline{lol}=\underline{lol}$. Thus, $\boldsymbol{g}$, $\boldsymbol{e}$ can be separately optimized by (2.73) if $\boldsymbol{h}$ is fixed; c) The risk only depends on $\boldsymbol{h}$, since given $\boldsymbol{h}^*$, the $\boldsymbol{g}^*$, $\boldsymbol{e}^*$ produces $\underline{lol}$, which are only determined by $\boldsymbol{h}$. □

The decomposed SRDSPP can be solved by exhaustively searching the solution space of $\boldsymbol{h}$ to determine $\boldsymbol{h}^*$ that results in $\underline{lol}$, then obtaining $\boldsymbol{g}^*$, $\boldsymbol{e}^*$ using the B&B algorithm. The complexity can be reduced to $\mathcal{O}(2^{|\mathbb{L}|})$, which is linear with respect to MEG and MESS allocation, while still exponential with respect to the number of DLs $|\mathbb{L}|$. To further speed up the computation, we employ Particle Swarm Optimization (PSO) algorithm [112]. It solves the problem by iteratively improving the position of particles towards the optimal solution, utilizing the best local and global known positions. Then, the computational complexity can be further reduced to $\mathcal{O}(IT_P)$, which is of linear complexity. Note that I is the number of particles, and T_P is the number of PSO algorithm iterations.

2.4 Case Study

In this section, the test system setup is illustrated. The effectiveness of the proposed planning strategy are demonstrated based on the IEEE 37-Node Test Feeder and the IEEE 123-Node Test Feeder. Also, comparisons are conducted between the proposed planning strategy and other strategies.

2.4.1 Test System Setup

For case study, a PC with Intel CORE i7-10700 CPU and 8 GB DDR4 RAM, and Gurobi 9.0.3 with B&B algorithm [113] is selected as a test platform. Also, since the 1994 M_L 6.7 Northridge earthquake is the most severe one recorded in urban areas in North America [114], we select the Pico Thrust Fault of this earthquake as the seismic source to demonstrate the proposed planning strategy. Specifically, the coordinate of epicenter is $[34°12'47''N, 118°32'13''W]$, and the PDS is located at $[34°12'47''N, 118°32'13''W]$. Moreover, the loads are categorized as critical loads with load priority $p_n = 5$ and non-critical loads with load priority $p_n = 1$. Fig. 2.3 shows the detailed time-varying load profiles for non-critical loads which are residence, and critical loads which are fuel station, fire station, emergency center, and water station [115]. Furthermore, the DL hardening cost is $\$312.5$K/km [116]. The load shed cost is $\$14$/kWh [117]. The occurrence of earthquakes $\mathcal{F}$ is set to 10. Tables 2.1 and 2.2 show the investment costs of MEGs and MESSs, respectively [118] [119]. Three types of MEGs (i.e., B1, B2, and B3) and three types of MESSs (i.e., D1, D2, and D3) with different parameters are available to be selected. The MESS charging and discharging efficiencies is assumed to be $\eta^{ch} = 0.9$ and $\eta^{dis} = 0.95$, respectively. Also, the initial and minimum SOC of MESS is assumed to be $\eta^{ini} = 0.8$, and $\eta^{min} = 0.1$, respectively.

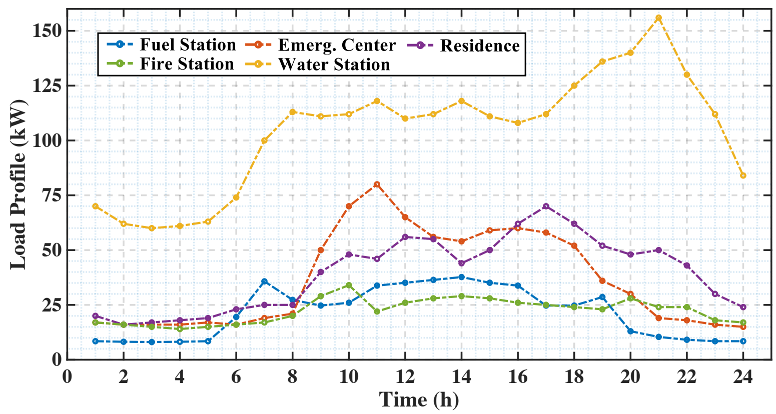

Figure 2.3: Load profiles of different customers over 24-hours time scale.

Table 2.1: Available MEG Product List

MEG Type	$\overline{G}^p$ (kW)	$\overline{G}^q$ (kVar)	Cost ($)
B1	360	270	390k
B2	237	180	260k
B3	185	137	210k

Table 2.2: Available MESS Product List

MESS Type	$\overline{E}^p$ (kW)	$\overline{E}^q$ (kVar)	$\overline{E}$ (kWh)	Cost ($)
D1	300	300	1000	180k
D2	250	250	800	150k
D3	200	200	600	120k

2.4.2 Case Study I: IEEE 37-Node Test Feeder

In this subsection, the seismic damage analysis and scenario aggregation are discussed. The results of simulation based on the IEEE 37-node Test Feeder [92] are presented, including the investment portfolio, and MEG and MESS coordination.

1) Seismic Damage Analysis and Scenario Aggregation: In Case I, the PDS is divided into three spatial seismic zones with 4.5km, 5km, and 5.5km away from the epicenter. The probability density function of PGA for each zone can be obtained, as shown in Fig. 2.4(a). It can be seen that the curves become narrow as the distance increases, which implies that the closer an earthquake is, the more likely the location of interest will experience a higher level of PGA. Also, following HAZUS methodology [98], the seismic damage is divided into 5 states, i.e., normal, slight, moderate, extensive and complete state with 0%, 4%, 12%, 50% and 80% of all DLs being damaged, respectively. Then, the fragility curves can be developed, as shown in Fig. 2.4(b). We can observe that by considering hardening measures, the fragility curves shift to the right hand side significantly. It means that the probability for a PDS to fall into a relatively higher damage state under one specific PGA will be

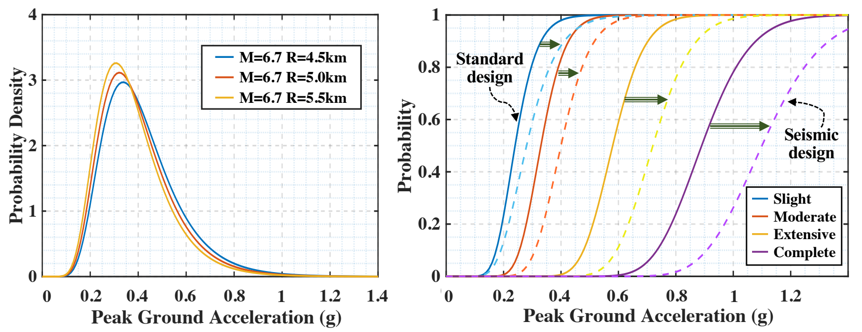

(a) PGA probability density function (b) Fragility curves of power distribution system

Figure 2.4: Seismic damage analysis in terms of PGA and fragility.

DL Index

Scenario	1				5					10					15					20					25					30					35	$\sum_j \mathcal{A}_{ij}$
3	1	1	0	1	1	1	0	1	0	0	0	1	0	0	0	0	0	1	1	1	1	0	1	1	1	0	0	0	1	1	0	0	0	0	1	133.2
52	1	1	1	1	0	0	0	0	0	1	1	0	0	0	1	0	0	0	1	1	0	0	0	0	1	0	0	0	1	0	1	0	0	0	1	119.6
119	1	1	1	1	0	0	0	1	0	0	0	0	0	0	0	1	1	0	1	1	1	1	0	0	0	0	1	0	0	1	0	0	1	1	1	117.5
145	1	1	0	1	0	1	0	0	0	0	0	0	0	0	0	1	0	0	1	0	0	0	1	1	0	0	0	1	1	1	0	0	0	1	1	140.8
153	1	1	1	1	0	0	0	1	0	0	0	0	1	0	0	1	0	0	1	1	0	0	0	1	1	0	0	0	1	0	1	1	0	1	1	130.2
296	1	1	1	1	0	0	0	1	0	0	0	1	1	1	0	1	1	0	1	0	0	0	1	0	0	0	0	1	1	0	0	0	0	0	1	130.5
323	1	1	1	1	0	0	0	1	1	0	1	1	0	0	0	1	0	0	1	0	0	0	1	0	1	0	0	1	1	0	1	1	0	0	1	130.1
405	1	1	1	1	0	1	0	0	0	0	1	1	0	0	1	0	0	0	1	0	0	1	0	1	0	0	1	0	0	0	0	0	0	0	0	115.3
455	1	1	1	1	0	1	0	1	0	0	0	1	0	0	0	1	0	0	1	0	1	0	1	1	1	0	0	0	1	1	0	0	0	0	1	139.8

Realization of Scenario: "1" denotes damaged DL

Figure 2.5: An illustration of seismic scenario aggregation.

decreased if hardening measures are taken. Moreover, we randomly generate 500 seismic scenarios, and implement the scenario aggregation with a predefined number of scenarios limit $N_C = 50$. Then, the Louvain algorithm is executed for two iterations. A total of 21 clusters are detected, which means the size of the scenario set is reduced to 21 from 500. Fig. 2.5 shows one of the clusters which aggregates 9 scenarios. We can see that there are many similarities among these scenarios. For example, for almost each scenario, DLs 1, 2, 3, 4, 19, 29, and 35 are damaged. This also illustrates the reason of their aggregation. Also, since scenario 145 has the largest sum of edge weight $\sum_j \mathcal{A}_{ij} = 140.8$, it is selected as the centroid, and becomes the representative scenario of this cluster.

2) Simulation Results and Analysis: In this subsection, we first implement the proposed SRDSPP on the test platform under zero risk, i.e., when $\rho = 0$. The loss

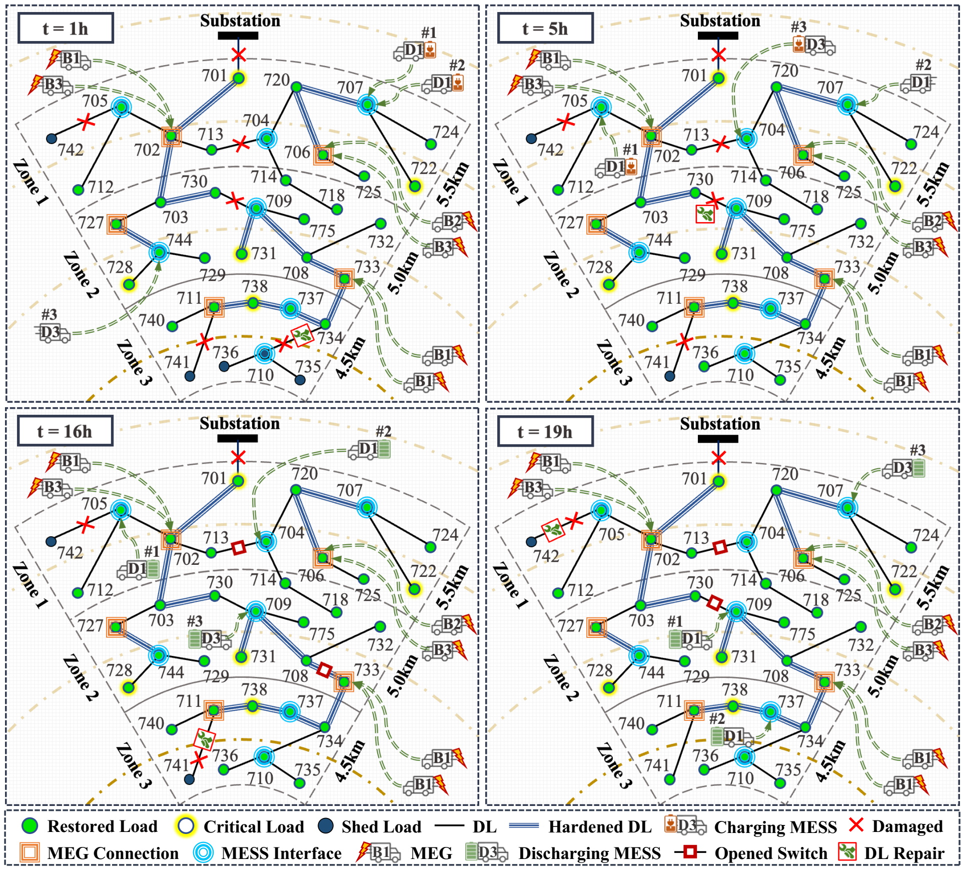

Figure 2.6: Simulation results of IEEE 37-Node Test Feeder under one sampled scenario and several representative time.

of load threshold $\Delta \overline{S}_{tr}$ is assumed to be 5% of all demands over 24 hours. Also, the road condition and the lag time of MESS transportation are ignored. Then, the whole problem is solved in 65.7 hours of wall clock time, of which subproblem (1) consumes 11.3 hours, and subproblem (2) consumes 54.4 hours. The optimal cost of hardening DLs $c_h \boldsymbol{l}^\top \boldsymbol{h}$ is $\$715.63$K. In total, twelve DLs are hardened with a total length of 2.29km. Also, the optimal cost of MEGs $\boldsymbol{c}_g^\top \boldsymbol{g}$ is $\$1,850$K, which includes three B1, one B2, and two B3. The optimal cost of MESSs $\boldsymbol{c}_e^\top \boldsymbol{e}$ is $\$480$K, with two D1, and one D3 are invested. Under this investment portfolio, the expected multi-time interruption cost is $\sum_{\hat{\omega}\in\hat{\Omega}} \pi_{\hat{\omega}}^{\boldsymbol{h}} c_s \sum_{t,n} \Delta S_n^{pt}(\hat{\omega}) = \$336.7$K, and the expected multi-time total loss of load $\sum_{\hat{\omega}\in\hat{\Omega}} \sum_{t,n} p_n \Delta S_n^{pt}(\hat{\omega})$ occupies 4.65% of all the weighted demand, which means that 95.35% of all the weighted demand will be restored over various scenarios. Moreover, when $\rho = 0$, the risk can be derived as

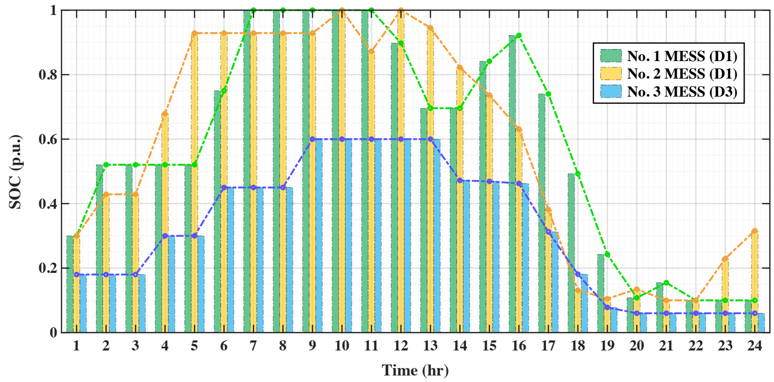

Figure 2.7: SOC of MESS in terms of multi-time scale under one scenario.

45.5K. It means that the probability of experiencing a seismic scenario with a large upper semideviation from the mean cost is very high. Hence, the risk management is necessary. For example, when $\rho = 0.5$, the cost of hardening DLs is increased to 778.21K, whereas the risk is decreased to 33.1K. Also, when $\rho = 1$, the cost of hardening DLs is increased to 909.38K, whereas the risk is further decreased to 12.7K. It implies that the system planner can be willing to pay more investment to obtain a lower risk of experiencing a severe seismic damage scenario.

Also, to demonstrate the performance of the seismic scenario aggregation, we compare the expected multi-time total loss of load over the original scenario set Ω with the reduced scenario set $\hat{\Omega}$. Note that $|\Omega| = 500$ and $|\hat{\Omega}| = 21$. Specifically, we set the DL hardening decision and the MEG and MESS investment decisions to the optimal solutions $\{\boldsymbol{h}^*, \boldsymbol{g}^*, \boldsymbol{e}^*\}$. Then, the loss of load $\Delta S_n^{pt}(\omega)$ under each scenario can be derived by the low-level problem, given by equation (2.14). Accordingly, the expected multi-time interruption cost for both the scenario sets Ω and $\hat{\Omega}$ can be obtained. The results of them are similar, which are $\sum_{\omega\in\Omega} \pi_\omega^{\boldsymbol{h}} c_s \sum_{t,n} \Delta S_n^{pt}(\omega) = \$358.1$K and $\sum_{\hat{\omega}\in\hat{\Omega}} \pi_{\hat{\omega}}^{\boldsymbol{h}} c_s \sum_{t,n} \Delta S_n^{pt}(\hat{\omega}) = \$336.7$K, respectively. It implies that the presented seismic scenario aggregation method performs effectively in scenario reduction, and the reduced scenario set $\hat{\Omega}$ can be used to replace the original set Ω.

Moreover, based on the optimal investment portfolio, we further illustrate the MEGs and MESSs Coordination. Fig. 2.6 shows the hardening DLs, coordination of MEGs and MESSs, including co-allocation and energy exchange, in terms of $t =$1h,

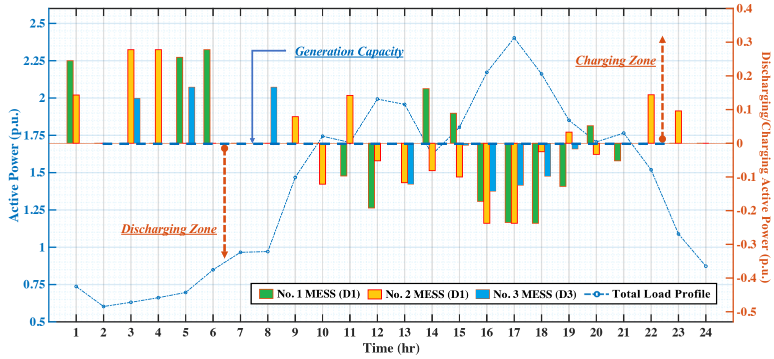

Figure 2.8: Energy exchange between MEGs and MESSs under one scenario.

5h, 16h, 19h under one sampled seismic scenario. Under this situation, a total of three microgrids are formed to provide emergency power, whose roots are at node 702 with one B1 and one B3, at node 706 with one B2 and one B3, and at node 733 with two B1, respectively. Moreover, when t =1h, MESS #1 (D1) and MESS #2 (D1) are charging at node 707, respectively. Crew members are repairing DL $(734, 710)$. In comparison, when t =5h, No.1 MESS (D1) and MESS #3 (D3) are transported to nodes 705, and 704 for charging, respectively. Also, nodes 710, 735, and 741 are further restored due to the repair of DL $(734, 710)$. When t =16h, all three MESSs are discharging because of the peak load demand. Also, the microgrids are re-scaled by opening line switches $(704, 713)$ and $(708, 733)$ to meet the load increment. When t =19h, the total load demand is obviously falling back but still high, thus all three MESSs are discharging. Also, line switch $(730, 709)$ is opened because of the increasing demand caused by the restoration of node 741. In addition, Fig. 2.7 shows the SOC of all the three MESSs, while Fig. 2.8 shows the coordination between MEGs and MESSs in terms of handling time-varying load demand with peak and valley. It can be seen that when the load demand is low, especially lower than the total generation capacity 1.69 p.u., e.g., t $\leq$9h, energy tends to be transferred from MEGs into MESSs in preparation for the peak demand. Also, when the load demand is higher than the generation capacity of 1.69 p.u., e.g., 10h$\leq$ t $\leq$20h, which means power generated by MEGs are not sufficient, the energy stored in MESSs is more likely to be fed back into the microgrids to supplement the power deficiency. Moreover, the total discharged energy is 2.631 p.u., and the total charged energy is 2.743 p.u. It means that almost all the energy

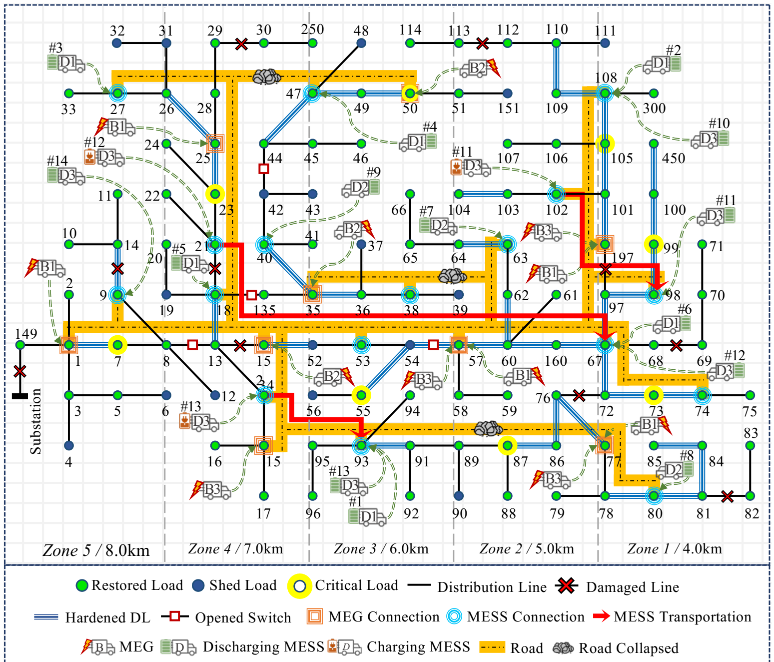

Figure 2.9: Simulation results of IEEE 123-Node Test Feeder under one sampled scenario at time $t = 18$h.

transferred from the MEGs is returned to the microgrids, and the MESSs exert no extra burden on the MEGs.

2.4.3 Case Study II: IEEE 123-Node Test Feeder

In this subsection, the effectiveness of the proposed planning strategy is verified based on the IEEE 123-Node Test Feeder. Specifically, the loss of load threshold $\Delta\overline{S}_{tr}$ is assumed to be 20% of all demands over a 24-hours time scale. The PDS is divided into five spatial seismic zones with 4.0km, 5.0km, 6.0km, 7.0km and 8.0km away from the epicenter. The lag time of MESS transportation is considered, which is 2 mins for each part of road. Note that a part of road refers to the road between two adjacent nodes. The problem is solved within 118.2 hours of wall clock time, including 19.5 hours consumed by subproblem (1), and 98.7 hours consumed by subproblem (2). The DL hardening cost is $\$1,618$K with a total length of 5.18km hardened. The MEG cost is $\$3,570$K, including five B1, three B2, and four B3. Also, the MESS cost is $\$2,130$K, with six D1, three D2, and five D3 invested. Under such an investment portfolio, the expected multi-time interruption cost is

\$3,246K, and the expected multi-time total loss of load occupies 19.81% of all the weighted demand, which means that 80.19% of all the weighted demand will be restored.

Fig. 2.9 shows the hardening DLs, and the coordination of MEGs and MESSs at time t =18h under one sampled seismic scenario, where a total of nine microgrids are established for emergency power supply. In particular, we can see that the microgrids rooted at nodes 57 and 77 contain more loads than others, hence having higher demands of $1,444$kw and $1,248$kw, respectively. Accordingly, MESS #11, #12, and #13 which are charging at previous time are transported to nodes 98, 67, and 93, respectively, discharging for energy exchange. In other words, MESSs can be charged in advance by MEGs when there is sufficient power, and then inject the power back into the microgrids to deal with the peak load. Also, benefiting from the mobility of MESSs, energy can be exchanged across microgrids. However, the MESS transportation is impacted by the road conditions. For example, since the road between nodes 38 and 67 is collapsed, MESS #12 is charged at node 21, and then transported to node 67, even though it is much further away from node 67 than node 38. Moreover, the lag time of MESS transportation can affect the performance of restoration. For example, if the lag time of MESS transportation is 1 min for each part of road instead of 2 mins in the previous setting, the expected multi-time interruption cost will be decreased to \$3,157k. Also, if no lag time is considered, the expected multi-time interruption cost will be further decreased to \$2,881k.

Furthermore, as shown in Fig. 2.9, we can see that the number of hardening DLs decreases along with the distance increases. Also, from zone 1 to 5, the total length of hardening DLs is 2.01km, 1.68km, 0.59km, 0.65km, and 0.24km, respectively, which shows an obvious decline trend by the distance from the epicenter. This is because the closer an earthquake is, the more likely that the zone will experience a higher PGA with more severe damages, and more DLs should be hardened to maintain the loss of load threshold $\Delta\overline{S}_{tr}$. However, if the PDS is regarded as one single point from the epicenter as done in the existing model [36–38], [50], e.g.,

R =6.0km, the total length of hardening DLs of zone 1 to 5 will be 1.37km, 1.48km, 0.76km, 0.85km, and 0.51km, respectively. Such a hardening plan is not realistic in terms of seismic attenuation. For example, zone 1 which is the closest to the epicenter is under hardened, while zone 5 which is the furthest from the epicenter is over hardened.

2.4.4 Case Study III: Comparison with Other Strategies

1) PDS Resilience Comparison: To demonstrate the importance of the pre-disaster long-term investment planning in PDS resilience enhancement, we make comparisons between three strategies based on case study II. The comparison is conducted in terms of the expected multi-time total loss of load $\sum_{\omega\in\Omega}\sum_{t,n} p_n \Delta S_n^{pt}(\omega)$ over various scenarios. The first strategy is the proposed one, which is "with the optimal investment portfolio of hardened DL, MEG, and MESS". The second strategy is "with the optimal investment of MEG and MESS, but with random DL hardening", which is the modified version of strategies in [48–52]. The modification is done by providing them with the MEG and MESS optimal planning derived from our strategy. The third strategy is "random investment portfolio of hardened DL, MEG, and MESS", which is the strategies in [48–52]. The results are listed in Table 2.3. We can see that our proposed strategy outperforms all other ones with only $21,457$kWh loss of load. This is because the investment of DL hardening, and MEGs and MESSs are co-optimized. By contrast, the modified strategies of [48–52] shed significantly more loads, which is $51,945$kWh, since the vulnerable DLs are not recognized and hardened. Also, the case without any optimal planning behaves the worst with $70,193$kWh loss of load. The results indicate that the pre-disaster long-term investment planning including hardening DLs, and adding new MEGs and MESSs can effectively improve PDS resilience.

2) Investment Cost Comparison: To verify the effectiveness of MEG and MESS coordination in cost-saving, we conduct comparisons between five strategies based on case study II, which are "with MEG and MESS coordination" (proposed), "with only MEGs" [43], " with only MESSs" [47], " with only DGs" [40], and "with only ESSs" [37]. Also, the same hardening plan is adopted for each strategy as

Table 2.3: Resilience Comparison in Terms of Loss of Load

Strategy	Description	Loss of load (kWh)
Proposed	With Optimal Hardened DL/ MEG/MESS Planning	21,457
Modified [48–52]	With Only Optimal MEG/MESS Planning	51,945
[48–52]	Without Optimal Planning	70,193

Table 2.4: Investment Cost Comparison Between Different Strategies

Strategy	B1	B2	B3	D1	D2	D3	Total Cost($)
Proposed	5	3	4	6	3	5	5,700k
MEG [43]	12	5	3	×	×	×	6,610k
MESS [47]	×	×	×	81	0	0	14,580k
—	B1'	B2'	B3'	D1'	D2'	D3'	—
DG [40]	16	3	6	×	×	×	7,452k
ESS [37]	×	×	×	94	2	0	15,440k

derived in the optimal portfolio. Table 2.4 lists the total cost and portfolio which results in the same loss of load threshold as in Subsection 2.5.3. Also, B1', B2', B3' and D1', D2', D3' are the non-mobile versions of B1, B2, B3 and D1, D2, D3 in Tables 3.2 and 2.2, respectively, with the same capacity but 10% off in cost. It can be seen that the time-varying load demand with peak and valley can be satisfied flexibly by MEG and MESS coordination, including co-allocation and energy exchange. It means that extra electricity produced by MEGs can be stored in MESSs when the load demand is lower, and fed back into the microgrid when the load demand increases. Thus, the proposed planning strategy costs the least, which is only $\$5,700$K with a total generation capacity of 3.251MW and energy capacity of 11.4MWh, without compromising the restoration capability. In comparison, the strategy with only MEGs costs higher, which is $\$6,610$K with a total generation capacity of 6.06MW. Because much more power is needed to deal with the peak load demand, which on the other hand may lead to MEG idle or under-utilization when demand is lower. Also, the strategy with only MESSs costs significant more, which is $\$14,580$K with a total energy capacity of 81.0MWh. This is because to achieve a power restoration over a 24-hours time scale without any generation, larger amounts of energy need to be stored in advance. Moreover, the strategies with DGs and ESSs perform even worse compared with their mobile versions. Since the fixed locations of DGs and ESSs are not adaptive to the random damages of earthquakes, more installation are required. Also, the comparison shows that by considering MEG and MESS coordination, the capability of MEGs and MESSs in restoration can be fully utilized, hence a lower investment cost can be achieved.

2.5 Summary

In this work, the stochastic planning problem of resilient PDSs against earthquakes is studied. Specifically, the portfolio of resilient measures including hardening DLs and investing MEGs and MESSs are investigated in a stochastic environment considering MEG and MESS coordination. A stochastic spatial seismic damage model is developed to characterize the random damages of earthquakes geographically. A solution procedure including scenario aggregation, endogenous uncertainty relaxation, problem reformulation and decomposition is proposed to reduce the computational burden. Furthermore, case studies based on the IEEE 37-node test feeder, 123-node test feeder and comparisons with other strategies demonstrate that the co-optimization of DL hardening and MEG and MESS investment considering MEG and MESS coordination including co-allocation and energy exchange is necessary. It can enhance the PDS resilience against earthquakes in a cost-effective manner.

Chapter 3

Data-Driven Resilience Enhancement for PDSs Against Multi-shocks of Earthquakes Under Uncertainties

In this work, a data-driven PDS resilience enhancement strategy is proposed against multi-shocks of earthquakes. In particular, the investment and pre-positioning of mobile emergency generators (MEGs) is determined against main shocks. The reallocation of MEG and the repair scheduling are obtained considering aftershocks and post-restoration failures. A resistibility index (RI) is developed based on HHMM for stochastic resilience evaluation. The historical earthquake data is incorporated into the HHMM as observed information of multi-shocks of earthquakes. Based on the RI, the problems of pre-positioning and reallocation of MEGs are formulated as mixed-integer programming problems. The problem of repair scheduling is formulated as an adaptive two-stage non-linear stochastic programming problem, for which a revision period is introduced to allow the decisions to adapt to the underlying uncertainties after the revision. The non-linearity arising from the revision period is addressed by introducing auxiliary variables. To reduce the computational complexity, an iterative algorithm is presented based on linear relaxation. The effectiveness of the proposed strategy is verified via case studies on the IEEE 123-node test feeder and historical earthquake data of Los Angeles, USA.

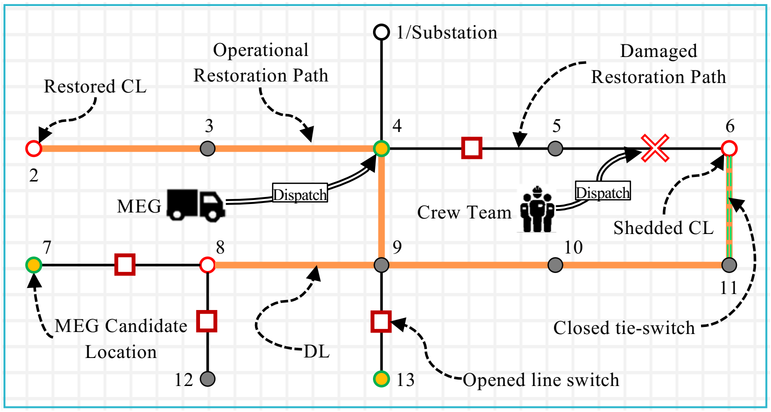

Figure 3.1: An illustration of the power distribution system model.

3.1 System Model

In this section, the system model with respect to PDSs, and stochastic seismic impact on distribution networks and restoration paths are introduced.

3.1.1 Power Distribution System Model

As show in Fig. 3.1, a modified IEEE 13-Node Test Feeder is chosen as the PDS. The modification is considering the PDS as a single phase system folowing the works in [43, 58, 60, 68]. Also, a tie-line is added between nodes 6 and 11. Specifically, the PDS is represented by a graph $G = (\mathcal{B}, \mathcal{L})$, where $\mathcal{B}$ is the set of electrical nodes and $\mathcal{L}$ is the set of DLs. A set of nodes $\mathcal{G} \subset \mathcal{B}$ are selected as candidate locations for MEG deployment according to facility requirements [120]. For example, as shown in Fig. 3.1, we have $\mathcal{B}=\{1, 2, \cdots, 13\}$, $\mathcal{L}=\{(1, 4), (2, 3), \cdots, (10, 11)\}$, and $\mathcal{G} = \{4, 7, 13\}$. Once an earthquake strikes, the worst-case is considered that the bulk system is collapsed, and the power restoration is completly dependent on MEGs. Moreover, we denote the restoration path connecting a MEG candidate location $g \in \mathcal{G}$ to a CL $c \in \mathcal{C} \subset \mathcal{B}$ as $g \Rightarrow c$. For example, in Fig. 3.1, we have $\mathcal{C} = \{2, 6, 8\}$. Accordingly, the restoration paths from MEG candidate location 4 to the three CLs are denoted by $4 \Rightarrow 2$, $4 \Rightarrow 6$ and $4 \Rightarrow 8$, respectively. Also, each restoration path $g \Rightarrow c$ is associated with a group $\mathcal{B}_{cg}$ of DLs. For example, we have $\mathcal{B}_{42} = \{(4, 3), (3, 2)\}$ for restoration path $4 \Rightarrow 2$, in Fig. 3.1. Note that following the work in [43, 58, 60, 68], it is assumed that the PDS is equipped with sufficient remotely controlled switches, so that the restoration paths can be utilized with certain boundaries and be energized by MEGs. For example, in Fig. 3.1, line switches on DLs $(4, 5)$, $(7, 8)$, $(8, 12)$, and $(9, 13)$ are opened, so that restoration paths $4 \Rightarrow 2$ and $4 \Rightarrow 8$ can be energized. Also, the tie-switch on tie-line $(6, 11)$ is closed to transfer isolated CL at node 6 to other feeders. In other words, before the post-disaster restoration, the PDS is de-energized because of the blackout. The system operator can either restore CLs by energizing the restoration paths without faults, or dispatch utility crew teams to repair the de-energized restoration paths if they are damaged. Also, a restoration path can be in either operational state or damaged state after earthquakes. It is considered damaged when one or more DLs of this restoration path are damaged. Because MEGs at one MEG candidate location can deliver power to several CLs via different restoration paths, a microgrid is accordingly established. Herein, the MG formation in [68] based on the linearized DistFlow model is applied. Then, the real and reactive power flows and nodal voltages can be obtained by

$$F_{ig}^{p} = u_{ig}P_i + \sum_j F_{jg}^{p}, \forall i \in \mathcal{B}, j \in \mathcal{B}_{CH}(i), \tag{3.1}$$

$$F_{ig}^{q} = u_{ig}Q_i + \sum_j F_{jg}^{q}, \forall i \in \mathcal{B}, j \in \mathcal{B}_{CH}(i), \tag{3.2}$$

$$V_{ig} - V_{jg} = (r_{ij}F_{ig}^{p} + x_{ij}F_{ig}^{q})/V_0, \forall i \in \mathcal{B}, j \in \mathcal{B}_{CH}(i), \tag{3.3}$$

where $\mathcal{B}_{CH}(i)$ is the set of child nodes of node i. Also, u_{ig} denotes the activation status of node i with respect to MEG candidate location g. If $u_{ig} = 1$, it means node i is picked up by MEG at location g, and vice versa.

Notice that the application of the proposed model can also be extended to three-phase unbalanced systems with missing phases. Specifically, a three-phase unbalanced system can contain single phase, two phase and three phase DLs, denoted by 1ϕ, 2ϕ and 3ϕ, respectively. Then, to ensure that the power can be delivered from MEGs to CLs successfully, effective restoration paths will be identified in advance. An effective restoration path should satisfy one of the following principles: i) MEGs and CLs are connected to DLs with the same number of phases; ii) MEGs should be connected to a DL with at least one more phase than the DL which the CL is connected to. In other words, an effective restoration path can deliver power from 3ϕ to 2ϕ, from 3ϕ to 1ϕ, and from 2ϕ to 1ϕ. However, restoration paths with the opposite power delivery are ineffective, and will not be utilized. Also, to address the power flow analysis in three-phase unbalanced systems, the generalized branch flow method in [121] can be applied.

3.1.2 Stochastic Seismic Impact Model for PDSs

To characterize the spatial seismic attenuation profile and quantify the impact of seismic hazard, we first identify the stochastic attenuation relationship between attenuation profile and the magnitude of earthquake represented by the Richter scale (M) [96], given by

$$\ln Y = f(M, R) + E, \tag{3.4}$$

where R represents the source-to-site distance, and Y denotes the peak ground acceleration (PGA). The uncertainty E can be modeled as a normally distributed random variable in seismological studies [97]. Accordingly, Y follows a log-normal distribution with median value $\overline{Y} = 0.0159 \exp(0.868M)[R{+}0.0606 \exp(0.7M)]^{-1.09}$ and standard deviation $\sigma = 1.45\overline{Y}$. Based on the HAZUS earthquake loss estimation method [98], fragility curves can be developed to model the probability for DLs to fall in or exceed a certain damage state $z \in \mathbb{Z} = \{Z_1, ...Z_n\}$. For a given PGA Y, the probability is given by

$$P(Z \geq z|Y) = \Phi[(1/\sigma_z) \ln{(Y/\overline{Y}_z)}], \tag{3.5}$$

where $\Phi[\cdot]$ denotes the standard normal cumulative distribution function, and the values of $\overline{Y}_z$ and σ_z can be obtained from the HAZUS method. Then, the probability of each damage state under a specific PGA can be derived as

$$P(z|Y) = P(Z \geq z|Y) - P(Z \geq z + 1|Y). \tag{3.6}$$

In order to model the stochastic seismic impact on DLs, we use W_z to denote the percentage of damaged DLs out of all DLs for damage state z. Then, the expected number of damaged DLs can be calculated as $n_d = n_t \sum_z P(z|Y)W_z$, where n_t is the total number of DLs. Moreover, the relationship between the length of DLs and the probability for it to be damaged is given in [60]. Then, based on the log-normal distribution of PGA and fragility curves, the number of damaged DLs can be randomly generated. Combined with the probability for each DL to be damaged, the seismic damage scenarios can be obtained. Each scenario is related to a realization containing a group of damaged DLs, and is associated with a probability of occurrence. We further denote $\xi(b)$ as the failure probability for DL b , which is defined as the occurrence of this damaged DL among all scenarios.

3.1.3 Stochastic Seismic Impact Model for Restoration Paths

The restoration path state ψ can be characterized as operational state ψ_o or damaged state ψ_d, where $\Psi = \{\psi_o, \psi_d\}$. To represent the state transitions of restoration paths considering main shocks and aftershocks of earthquakes, a Markov chain can be integrated in the stochastic seismic impact model. For each aftershock, the changes in the values of magnitude and distance can result in a different value of PGA Y. Accordingly, the transition probability of damage state from Z_i to Z_j can be derived as $T^D(Z_i, Z_j) = P(Z_j|Z_i)$ based on the PGA probability density function and fragility curves. Moreover, consider a restoration path $g \Rightarrow c$ with a group $\mathcal{B}_{cg}$ of DLs. Once a shock of earthquake occurs, based on the probability of a DL to be damaged, i.e., $\xi(b)$, where $b \in \mathcal{B}_{cg}$, the state transition probability of restoration path can be obtained as $T^R(\psi_o, \psi_d) = P(\psi_d|\psi_o) = 1 - \Pi_b(1 - \xi(b))$, $T^R(\psi_o, \psi_o) = P(\psi_o|\psi_o) = \Pi_b(1 - \xi(b))$, $T^R(\psi_d, \psi_o) = P(\psi_o|\psi_d) = 0$, and $T^R(\psi_d, \psi_d) = P(\psi_d|\psi_d) = 1$.

3.2 Formulation of Data-Driven PDS Resilience Enhancement Problem

Considering the randomness of multi-shocks of earthquakes, in this section, we first present the RI metric to evaluate the resilience of restoration paths. Specifically, for each restoration path, one HHMM is established. A PGA observation sequence containing the PGA information of multi-shocks of earthquake will be given based on historical earthquake data. Then, the most probable state sequences of the HHMM can be deduced [122]. Based on the state sequences, the RI metric can then be derived. Since HHMMs are developed to model the evolution of stochastic process

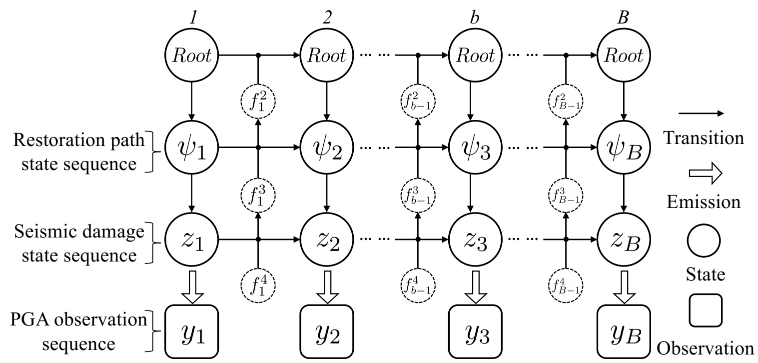

Figure 3.2: An illustration of HHMMs of restoration paths.

over multi-shocks of earthquakes, the RI can stochastically represent the resilience of restoration paths. In other words, by utilizing the historical data with multi-shocks of earthquakes information, the RI metric can be evaluated. Then, by using the derived RI metric, the pre-disaster planning and the post-disaster response are investigated in the context of future multi-shocks of earthquakes. Specifically, in the pre-disaster stage before main shocks, the investment and pre-positioning of MEGs is determined. It means that when investing and pre-positioning MEGs, the restoration path with higher value of RI will be preferred, such that the selected restoration path can be more resilient against multi-shocks of earthquakes. In the post-disaster stage, the reallocation of MEGs and the repair scheduling of restoration paths are determined considering post-restoration failures. In this section, the problem formulation is introduced.

3.2.1 Resistibility Indices Based on HHMMs

To address the random earthquake damages on a restoration path, we establish a dynamic Bayesian network representation of HHMM with three levels [122]. As shown in Fig. 3.2, the first level is the root state. The restoration path state sequence is in the second level, represented by a hidden vector $\boldsymbol{\psi} = (\psi_1, \ldots, \psi_B) \in \Psi^B$. The damage state sequence is in the third level, represented by a hidden vector $\boldsymbol{z} = (z_1, \ldots, z_B) \in \mathbb{Z}^B$. A PGA observation sequence, represented by a known vector $\boldsymbol{y} = (y_1, \ldots, y_B) \in \mathbb{Y}^B$, is emitted from the damage state sequence. It contains the PGA information of multi-shocks of earthquakes, which is composed of one main shock and $B-1$ subsequent aftershocks derived from the historical earthquake data. Next, we present the probabilities for HHMM as follows:

i) Vertical and horizontal transition probability

$$\Gamma = P(q_b^d = J' | q_{b-1}^d = J, f_{b-1}^{d:d+1}, q_{b-1}^{d-1} = I) = \begin{cases} \mu(J, J'), & \text{if } f_{b-1}^d = 0, f_{b-1}^{d+1} = 0; \\ T_I^d(J, J'), & \text{if } f_{b-1}^d = 0, f_{b-1}^{d+1} = 1; \\ \pi_I^d(J'), & \text{if } f_{b-1}^d = 1, f_{b-1}^{d+1} = 1. \end{cases} \tag{3.7}$$

ii) Level ending probability

$$\Sigma = P(f_b^d = 1 | q_b^d = J, q_b^{d-1} = I, f_b^{d+1}) = 0, \ \text{if } f_b^{d+1} = 0; \ T_{end}^d, \ \text{if } f_b^{d+1} = 1. \tag{3.8}$$

iii) Emission probability

$$\Xi = P(y | q_b^D = z) = e_z(y), \tag{3.9}$$

where $b \in \{1, ..., B\}$ denotes the time step of HHMM, and $d \in \{1, ..., D\}$ is the level of HHMM. Also, q_b^d is the state variable at time step b in level d. Specifically, when $d = 2$, $q_b^d = \psi \in \Psi$ is the restoration path state variable; when $d = 3$, $q_b^d = z \in \mathbb{Z}$ is the damage state variable. And, f_b^d is an end indicator, which equals 1 if level d ended at q_b^d. In other words, $f_b^d = 1$ implies a possible state change in level $d-1$. The emission probability is related to the probability of observing a PGA y from damage state z, which can be derived as $e_z(y) = P(y|z) = P(z|y)P(y)/P(z)$, where $P(z) = \mathbb{E}_y[P(z|y)]$. The values of parameters in equations (3.7)-(3.9) are given as follows:

▷ The value of T_{end}^d is the ending probability of level d;

▷ The value of $T_I^d(J, J')$ is the horizontal transition probability from state J to J' in level d, when the upper-level $d-1$ is in state I. Based on the transition probabilities of damage states and restoration path states presented in Subsection 3.1.3, if $d = 2$, $T_I^d(J, J') = T^R(J, J')/(1 - T_{end}^d)$, else if $d = 3$, $T_I^d(J, J') = T^D(J, J')/(1 - T_{end}^d)$;

▷ The value of $\mu(J, J')$ equals to 1 if $J = J'$, meaning that no horizontal transition occurs in level d, otherwise 0;

▷ The value of $\pi_I^d(J')$ is the vertical transition probability from state I in level $d-1$ to state J' in level d.

In addition, the probabilities described in equations (3.7)-(3.9) determine the stochastic evolution of the HHMM. It can affect the restoration path state and damage state transitions over multi-shocks of earthquakes given by the observation sequence $\boldsymbol{y}$. Hence, there can be many feasible state sequences $\{\boldsymbol{\psi}, \boldsymbol{z}\}$, which can be considered as different scenarios. For simplicity, we denote $\mathbb{P} = \{\Gamma, \Sigma, \Xi\}$. Accordingly, we have the following optimization problem for each restoration path $g \Rightarrow c$:

$$\text{(P1)} \qquad \max_{\boldsymbol{\psi},\boldsymbol{z},\boldsymbol{f}} P_{cg}(\boldsymbol{\psi}, \boldsymbol{z}, \boldsymbol{f} | \boldsymbol{y}; \mathbb{P}), \tag{3.10}$$

which implies to find the optimal state sequences $\{\boldsymbol{\psi}^*, \boldsymbol{z}^*\}$ to maximize the joint probability P_{cg} to best match the given PGA observation sequence $\boldsymbol{y}$. Physically, it means that the PGA information is observable, and the decision maker aims to deduce how the restoration path and damage state will transit given the PGA information. In other words, the optimal state sequences $\{\boldsymbol{\psi}^*, \boldsymbol{z}^*\}$ can be regarded as the most representative scenario to model the evolution of stochastic process over $\boldsymbol{y}$. Then, based on the deduced state sequence $\boldsymbol{\psi}^*$, to evaluate the resilience of restoration paths, the RI can be defined.

Definition. The RI of one restoration path $g \Rightarrow c$ (denoted by $\mathcal{R}_{cg}$) is defined as the expected occurrence of the operational state ψ_o in state sequence $\boldsymbol{\psi}^*$ over $\boldsymbol{y}$, stated as

$$\mathcal{R}_{cg} = E_{\boldsymbol{y}}[N_{\psi_o}(\boldsymbol{y})/B], \tag{3.11}$$

where $N_{\psi_o}(\boldsymbol{y})$ denotes the number of the operational state ψ_o in $\boldsymbol{\psi}^*$ given the observation sequence $\boldsymbol{y}$. Physically, it means the higher the occurrence of the operational state ψ_o is, the higher the RI is, and the more resilient the restoration path can be.

Since an earthquake process is a seismic sequence consisting of an intensive main shock and multiple aftershocks, the magnitude and location of each shock can be recorded by seismometers. This recorded historical earthquake data can be obtained from the United States Geological Survey [123]. It is composed of the information of magnitudes and distances $\{M, R\}$ of a series of shocks. Accordingly, the PGA density function for each shock can be derived based on Subsection 3.1.2. Then, by sampling the PGA density function, the PGA at each time step of the HHMM can be obtained. And, the observation sequences $\boldsymbol{y}$ can be randomly generated based on the historical data. Finally, the RI is obtained as the expected value over different $\boldsymbol{y}$. Compared with the indices in [58–60] which are developed based on the deterministic analysis, the proposed RI can stochastically evaluate the resilience of restoration paths, since it is derived from HHMMs which integrated with the randomness of multi-shocks of earthquakes.

3.2.2 Pre-Disaster MEG Investment and Pre-Positioning

In the pre-disaster stage, an investment and pre-positioning problem is formulated. The objective is to identify the portfolio of MEGs with the lowest investment cost, which ensures the system average RI is greater than a threshold, given by

$$\text{(P2)}\quad \min_{\boldsymbol{s},\boldsymbol{p}} \left\{\textstyle\sum_e c_e s_e + w_{\mathcal{R}}\big(1-\sum_{c,g} p_{cg}\mathcal{R}_{cg}/N_c\big)\right\} \tag{3.12}$$

where the first term denotes the total investment cost, and the second term in the parentheses is the system average RI. Also, p_{cg} is a binary variable denoting the status of the restoration path. It equals to 1 if an MEG is deployed at MEG candidate location g, and restoration path $g \Rightarrow c$ is selected to restore CL c. Thus, the second term in equation (3.12) implies that under a specific MEG investment portfolio, the restoration path to each CL will be selected to achieve the highest system average RI. Also, the following constraints are applied:

$$\text{s.t. } (3.1)-(3.3), \text{and} \textstyle\sum_{c,g} p_{cg} = N_c, \tag{3.13}$$

$$\textstyle\sum_{c,g} p_{cg}\mathcal{R}_{cg}/N_c \geq \overline{\mathcal{R}}_{tr}, \tag{3.14}$$

$$v_{ge} \leq s_e, \forall e \in \mathcal{E}, g \in \mathcal{G}, \tag{3.15}$$

$$v_{ge} \geq u_{ig}, \forall i \in \mathcal{B}, g \in \mathcal{G}, \tag{3.16}$$

$$\textstyle\sum_{g\in\mathcal{G}} u_{ig} \leq 1, \forall i \in \mathcal{B}, \tag{3.17}$$

$$u_{ig} - u_{jg} \geq 0, \forall i \in \mathcal{B}, j \in \mathcal{B}_{CH}(i), \tag{3.18}$$

$$p_{cg} \leq u_{ig}, \forall i = c \in \mathcal{C}, \tag{3.19}$$

$$\textstyle\sum_{g\in\mathcal{G}} p_{cg} \leq 1, \forall c \in \mathcal{C}, \tag{3.20}$$

$$(1-\rho)u_{ig} \leq V_{ig} \leq (1+\rho)u_{ig}, \forall i \in \mathcal{B}\backslash\mathcal{G}, \tag{3.21}$$

$$u_{ig}V_0 \leq V_{ig} \leq u_{ig}V_0, \forall i = g \in \mathcal{G}, \tag{3.22}$$

$$\textstyle\sum_{e\in\mathcal{E}} v_{ge} \leq 1, \forall g \in \mathcal{G}, \tag{3.23}$$

$$0 \leq \textstyle\sum_{i\in\mathcal{B}_{CH}(g)} F^p_{ig} \leq \sum_{e\in\mathcal{E}} v_{ge}P^e_M, \forall g \in \mathcal{G}, \tag{3.24}$$

$$0 \leq \textstyle\sum_{i\in\mathcal{B}_{CH}(g)} F^q_{ig} \leq \sum_{e\in\mathcal{E}} v_{ge}Q^e_M, \forall g \in \mathcal{G}. \tag{3.25}$$

Constraint (3.13) ensures that all the CLs can be restored at the pre-disaster stage. Constraint (3.14) ensures the system average RI to be no less than the pre-specified threshold $\overline{\mathcal{R}}_{tr}$. Constraint (3.15) indicates that an MEG can be deployed only when it is invested. Constraint (3.16) means that electrical nodes can only be activated by a source node where an MEG is deployed. Constraint (3.17) ensures each node can be activated by at most one MEG. Constraint (18) represents that a child node cannot be activated unless its parent node is activated. Constraint (3.19) means that a restoration path can only be constructed when the connected CL is activated by the source of this restoration path. Constraint (3.20) ensures each CL is restored by at most one path. Constraint (3.21) limits the nodal voltages within an acceptable range. Constraint (3.22) ensures the voltages at the nodes where MEGs are deployed to be set to the reference voltage V_0. Constraint (3.23) means that one electrical node can accommodate only one MEG. Constraints (3.24)-(3.25) limit the total demand within the generation capacity.

3.2.3 Post-Disaster MEG Reallocation and Repair Scheduling

1) MEG Reallocation: The post-disaster MEG reallocation problem is to transport MEGs to re-establish emergency power services when the pre-planned restoration paths collapsed. The objective is to restore as many CLs as possible with the highest priority ($\mathcal{I}_c$), considering the overall system RI in case of future aftershocks, given by

$$\text{(P3)} \qquad \max_{\boldsymbol{p}} \left\{ w_c \textstyle\sum_{c\in\mathcal{C}} p_{cg}\mathcal{I}_c + \sum_{c,g} p_{cg}\mathcal{R}_{cg} \right\} \tag{3.26}$$

$$\text{s.t. } (1)-(3), (16)-(21), \text{and}$$

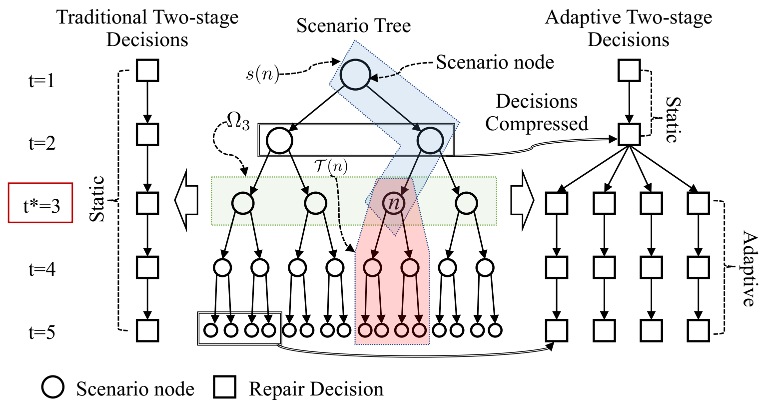

Figure 3.3: An illustration of adaptive two-stage stochastic programmings.

$$v_{ge'} \geq u_{ig}, \ \ \forall i \in \mathcal{B}, \ \ g \in \mathcal{G}, \tag{3.27}$$

$$\textstyle\sum_{e' \in \mathcal{E}'} v_{ge'} \leq 1, \ \ \forall g \in \mathcal{G}, \tag{3.28}$$

$$0 \leq P_g \leq \textstyle\sum_{e' \in \mathcal{E}'} v_{ge'} P_{e'}^M, \ \ \forall g \in \mathcal{G}, \tag{3.29}$$

$$0 \leq Q_g \leq \textstyle\sum_{e' \in \mathcal{E}'} v_{ge'} Q_{e'}^M, \ \ \forall g \in \mathcal{G}. \tag{3.30}$$

where the first term represents the total restored CL priorities, and the second term denotes the overall system RI. In other words, the CLs with higher priorities are prioritized in restoration while using the restoration path with the highest resilience against multi-shocks of earthquakes. Furthermore, constraints (3.27)-(3.30) are similar to constraint (3.16) and constraints (3.23)-(3.25) except that the reallocated MEGs are the ones invested in the pre-disaster stage, i.e., $\mathcal{E}' \subset \mathcal{E}$.

2) Repair Scheduling: The post-disaster repair scheduling problem is formulated as an adaptive multi-period two-stage stochastic programming problem [124]. It aims to determine the sequential repair decisions of damaged restoration paths. In the traditional setup of two-stage stochastic programming [125], such decisions are the first-stage here-and-now decisions that are fixed in any period $t \in \mathbb{T} = \{1, 2, ...T\}$. By contrast, in the adaptive setup, a revision period t^* is introduced. The sequential repair decisions are only fixed before t^*. And, one revision of the sequential repair decisions is allowed during t^*, such that the decisions can be partially adaptive to the underlying uncertainties. Then, after t^*, with respect to each revealed uncertainty, the sequential repair decisions are fixed again. Physically, the system operator intends to determine a sequential repair schedule with length $(t^* - 1)$, then observing the uncertainties at t^* for one time and revising the sequential repair decisions accordingly. An illustration can be shown in Fig. 3.3, where five restoration paths are damaged, i.e., $T = 5$, calling for repair scheduling with $t^* = 3$. The middle shows the multi-shocks of earthquake damage scenario tree. The left shows the sequential decisions of the traditional setup, where the repair decisions are fixed throughout the repair horizon. The right shows the sequential decisions of the adaptive setup, where one revision is conducted by the system operator after observing the uncertainties. Note that the repair time Δt, i.e., duration of each period, for restoration paths are considered equal. The reason is the repair time cannot be specified exactly, until the repair is completed by the crews. Yet, a repair schedule is required for guidance before crew dispatching. Thus, we assume equal repair time to determine the repair sequence for crew dispatch.

For simplicity, we denote $\overline{\mathcal{IR}}_{cg} = \tau_1 - \{\mathcal{I}_c + \tau_2 \mathcal{R}_{cg}\}$, for which the lower the value is, the higher the priority of the CL and the higher the resilience of the restoration path will be. By appropriately setting the values of τ_1 and τ_2, the value of $\overline{\mathcal{IR}}_{cg}$ can carry both the information of load priorities ($\mathcal{I}_c$) and restoration path RI ($\mathcal{R}_{cg}$). Also, we use χ_c^n to denote the available number of restoration paths of CL c at scenario node n. If χ_c^n is multiplied by a large weight factor τ_0, the value of $(\tau_0 \chi_c^n + \overline{\mathcal{IR}}_{cg})$ can include the information of the available number of restoration path of CL c, the load priority of CL c, and the RI of restoration path $g \Rightarrow c$. Then, the objective of the repair scheduling problem is to obtain the sequential repair decisions to minimize the sum of multi-period expected number of available restoration paths and $\overline{\mathcal{IR}}$, given by

$$\text{(P4)} \quad \min_{\boldsymbol{m}, t^*} \textstyle\sum_{t \in \mathbb{T}} \mathbb{E}_{n \in \Omega_t} \big\{ \textstyle\sum_{c,g,k} m_{cg}^{nk} (\tau_0 \chi_c^n + \overline{\mathcal{IR}}_{cg}) \big\} \tag{3.31}$$

where m_{cg}^{nk} is the repair decision. It is a binary variable, which equals 1, if restoration path $g \Rightarrow c$ is repaired at scenario node n by crew team k. Physically, the optimal solution of problem (P4) ensures the following repair principles [58], [68]: i) The damaged restoration path whose CL has the least available paths will be repaired first; ii) If two damaged restoration paths both satisfy principle i), the path whose CL is with higher load priority will be repaired first; iii) If two damaged restoration paths connect to the same CL, the path with higher RI will be repaired first. Accordingly, a damaged restoration path with the lower value of $(\tau_0\chi_c^n+\overline{\mathcal{IR}}_{cg})$ must be repaired first than the one with the higher value, as one of the repair principles must be satisfied. Also, the following constraints are applied:

$$\chi_c^n \leq m_{cg}^{nk}M, \forall c \in \mathcal{C}, g \in \mathcal{G}, n \in \mathcal{T}, k \in \mathbb{K}, \tag{3.32}$$

$$\chi_c^n \leq N_{\mathcal{P}}^c - \sum\nolimits_g d_{cg}^n + \sum\nolimits_{g,n' \in s(n),k} m_{cg}^{n'k}, \tag{3.33}$$

$$\chi_c^n \geq N_{\mathcal{P}}^c - \sum\nolimits_g d_{cg}^n + \sum\nolimits_{g,n' \in s(n),k} m_{cg}^{n'k} - (1-m_{cg}^{nk})M, \tag{3.34}$$

$$m_{cg}^{n'k} \leq d_{cg}^n, n \in \Omega_1, \forall n' \in \mathcal{T}, \tag{3.35}$$

$$\sum\nolimits_{k \in \mathbb{K}, n \in s} m_{cg}^{nk} \leq 1, \forall s \in \mathbb{S}, c \in \mathcal{C}, g \in \mathcal{G}, \tag{3.36}$$

$$\sum\nolimits_{c,g} m_{cg}^{nk} \leq 1, \forall n \in \mathcal{T}, k \in \mathbb{K}, \tag{3.37}$$

$$\sum\nolimits_{c,g,n \in s} m_{cg}^{nk} = N_{\mathcal{P}}^d, \forall s \in \mathbb{S}, \tag{3.38}$$

$$m_{cg}^{nk} = m_{cg}^{n'k}, \forall n, n' \in \Omega_t, t<t^*, \tag{3.39}$$

$$m_{cg}^{n'k} = m_{cg}^{n''k}, \forall n', n'' \in \mathcal{T}(n) \cap \Omega_t, n \in \Omega_{t^*}, t \geq t^*. \tag{3.40}$$

Constraints (3.32)-(3.34) are to calculate the available number of restoration paths of CL c at scenario node n (χ_c^n), when one of the damaged paths of this CL is being repaired. Specifically, if $m_{cg}^{nk} = 1$, then $\chi_c^n = N_{\mathcal{P}}^c - \sum\nolimits_g d_{cg}^n + \sum\nolimits_{g,n' \in s(n),k} m_{cg}^{n'k}$, otherwise $\chi_c^n = 0$. Constraint (3.35) implies only the actual collapsed restoration paths can be repaired. Constraint (3.36) means that one path can be repaired only once. Constraint (3.37) means that one crew team can only repair one damaged path in each scenario node. Constraint (3.38) forces the total number of repaired paths throughout the horizon be equal to the total number of actual damaged paths $N_{\mathcal{P}}^d$. Constraint (3.39) ensures that the repair decisions at each t before the revision period are compressed to the same. Constraint (3.40) indicates the repair decisions of scenario node $n' \in \mathcal{T}(n) \cap \Omega_t$, $t \geq t^*$ are compressed to the same for the remaining horizon, where n is the scenario node in the revision period t^*.

3.3 Solutions of Data-Driven PDS Resilience Enhancement Problem

The solutions of the data-driven PDS resilience enhancement problem consist of three parts: i) The solution to the HHMM to derive the restoration path resilience RI; ii) The solution to the mixed-integer linear programming problem to address the pre-positioning and reallocation of MEGs based on RI; and iii) The solution to the adaptive multi-period two-stage stochastic programming problem to obtain the optimal sequential repair decisions with consideration of RI. For the HHMM, we reformulate problem (P1) recursively and apply the general Viterbi Algorithm. Then, the most probable state sequences $\{\boldsymbol{\psi}^*, \boldsymbol{z}^*\}$ can be deduced to best match the given PGA observation sequence $\boldsymbol{y}$. To solve the mixed-integer linear programming problems (P2) and (P3), the Branch-and-Bound algorithm is applied. Furthermore, to solve the adaptive multi-period two-stage programming problem (P4), auxiliary variables are introduced to address the non-linearity arising from the revision period t^*. Also, an iterative algorithm based on linear programming relaxation is proposed to reduce the computational complexity resulted by the revision period. In this section, the solution procedure is discussed.

3.3.1 HHMM Reformulation and Solution

For each HHMM of restoration paths, the most probable state sequences $\{\boldsymbol{\psi}^*, \boldsymbol{z}^*\}$ are the ones which can best match the given obsevation sequence $\boldsymbol{y}$, given by

$$\{\boldsymbol{\psi}^*, \boldsymbol{z}^*, \boldsymbol{f}^*\} = \arg\max_{\boldsymbol{\psi},\boldsymbol{z},\boldsymbol{f}} P_{cg}(\boldsymbol{\psi}, \boldsymbol{z}, \boldsymbol{f} | \boldsymbol{y}; \mathbb{P}). \tag{3.41}$$

To obtain the most probable state sequences, the general Viterbi Algorithm can be utilized [122]. For notation simplicity, we use: i) $\hat{\boldsymbol{\upsilon}}_b$ to represent the set of elements in the state sequences from step 1 to b, i.e., $\hat{\boldsymbol{\upsilon}}_b \triangleq \{\boldsymbol{\psi}_b, \boldsymbol{z}_b, \boldsymbol{f}_{1:b}^{1:(D+1)}\}$, and ii) υ_b to represent the set of elements at step b, i.e., $\upsilon_b \triangleq \{\psi_b, z_b, f_b^{1:(D+1)}\}$. Then, the maximization of $P_{cg}(\hat{\boldsymbol{\upsilon}}|\boldsymbol{y}; \mathbb{P})$ is equivalent to maximize $P_{cg}(\hat{\boldsymbol{\upsilon}}, \boldsymbol{y}; \mathbb{P}) P_{cg}(\boldsymbol{y}; \mathbb{P})$, where $\hat{\boldsymbol{\upsilon}} = \hat{\boldsymbol{\upsilon}}_B = \{\boldsymbol{\psi}, \boldsymbol{z}, \boldsymbol{f}\}$. Now we can define the log probability of the most probable state sequences which starts at step 1, emits $\boldsymbol{y}_b = (y_1, y_2, ..., y_b)$, passes through $\hat{\boldsymbol{\upsilon}}_{b-1}$, and ends at step b with υ_b as follows:

$$\delta_b(\upsilon) = \max_{\hat{\boldsymbol{\upsilon}}_{b-1}} \log[P_{cg}(\hat{\boldsymbol{\upsilon}}_{b-1}, \upsilon_b = \upsilon, \boldsymbol{y}_b; \mathbb{P})], \tag{3.42}$$

where the term $P_{cg}(\boldsymbol{y}; \mathbb{P})$ is omitted since it is independent of $\hat{\boldsymbol{\upsilon}}_{b-1}$, and accordingly has no effect on the maximization with respect to $\hat{\boldsymbol{\upsilon}}_{b-1}$. Then, by introducing $\delta_{b-1}(\upsilon')$, we can rewrite (3.42) recursively as follows:

$$\begin{aligned} \delta_b(\upsilon) = \max_{\upsilon'}\{\delta_{b-1}(\upsilon')+ \\ \log P_{cg}(\upsilon_b{=}\upsilon|\upsilon_{b-1}{=}\upsilon'; \mathbb{P})\}{+}\log P_{cg}(y_b|\upsilon_b; \mathbb{P}). \end{aligned} \tag{3.43}$$

By tracking υ' at time step $b-1$ which maximizes $\delta_b(\upsilon)$ at b, the most probable $\hat{\boldsymbol{\upsilon}}^*$ for the given $\boldsymbol{y}$ can be deduced. To record this tracking, a function ζ is defined as

$$\begin{aligned} \zeta_b(\upsilon) = \arg\max_{\upsilon'}\{\delta_{b-1}(\upsilon') \\ + \log P_{cg}(\upsilon_b = \upsilon|\upsilon_{b-1} = \upsilon'; \mathbb{P})\}, \end{aligned} \tag{3.44}$$

where function $\zeta(\upsilon)$ stores υ' at time step $b-1$, which can maximize $\delta_b(\upsilon)$ for any υ at time step b.

3.3.2 Linearization of the Repair Scheduling Problem

The formulated adaptive multi-period two-stage stochastic programming problem is nonlinear due to the revision period t^* related constraints (3.39)-(3.40). To linearize the problem, we introduce an auxiliary variable γ_t for each period to eliminate the impact of t^*. If $\gamma_t = 1$, it means the revision period $t^* = t$. Then, the problem (P4) can be reformulated as follows:

$$\min_{\boldsymbol{m},\boldsymbol{\chi},\boldsymbol{\gamma}} \sum_{t\in\mathbb{T}} \mathbb{E}_{n\in\Omega_t}\big\{ \sum_{c,g,k} m_{cg}^{nk}\big\{\tau_0\chi_c^n + \overline{\mathcal{IR}}_{cg}\big\}\big\} \tag{3.45}$$

$$\text{s.t. } (3.31)-(3.37), \text{and} \sum_{t\in\mathbb{T}} \gamma_t = 1, \tag{3.46}$$

$$m_{cg}^{nk} \geq m_{cg}^{n'k} - \sum \overline{\gamma}_{t'}, \forall n, n' \in \Omega_t, t \in \mathbb{T}\backslash\{T\}, \tag{3.47}$$

$$m_{cg}^{nk} \leq m_{cg}^{n'k} + \sum \overline{\gamma}_{t'}, \forall n, n' \in \Omega_t, t \in \mathbb{T}\backslash\{T\}, \tag{3.48}$$

$$m_{cg}^{nk} \geq m_{cg}^{n'k} - \overline{\gamma}_t, \forall n, n' {\in} \mathcal{T}(n'') \cap \Omega_{t'}, t' \geq t, n'' {\in} \Omega_t, \tag{3.49}$$

$$m_{cg}^{nk} \leq m_{cg}^{n'k} + \overline{\gamma}_t, \forall n, n' {\in} \mathcal{T}(n'') \cap \Omega_{t'}, t' \geq t, n'' {\in} \Omega_t, \tag{3.50}$$

where $\sum \overline{\gamma}_{t'}$ is used to denote $(1 - \sum_{t'=t+1}^{T} \gamma_{t'})$ for simplicity, and $\overline{\gamma}_t = (1 - \gamma_t)$. Constraint (3.46) ensures that there exists only one revision period t^* throughout the multi-period repair horizon. Constraints (3.47)-(3.48) and (3.49)-(3.50) are the linearized version of constraints (3.39) and (3.40), respectively.

3.3.3 Iterative Algorithm for the Repair Scheduling Problem

To increase the computational efficiency of the post-disaster repair scheduling problem, we develop an iterative algorithm based on the linear programming relaxation and the traditional two-stage version of problem (P4) [124] [126] [127]. Note that the adaptive two-stage stochastic programming problem can be equivalent to a traditional two-stage stochastic programming problem when $t^* = 1$. Accordingly, constraints (39)-(40) can be simplified as $m_{cg}^{nk} = m_{cg}^{n'k}, \ \forall n, n' \in \Omega_t, t \in \mathbb{T}$. Herein, we use v^{ATS} and v^T to denote the optimal value of the linear programming relaxations of problem (P4) and its traditional version, respectively. Similarly, $\hat{V}^{ATS}(t^*, \boldsymbol{m})$ and $\hat{V}^T(\boldsymbol{m})$ denote the values under arbitrary feasible decision $\boldsymbol{m}$ given revision period t^*, and $V^{ATS}(t^*)$ and V^T denote the optimal values of problem (P4) and its traditional version given t^*, respectively. Then, the following lemmas hold.

Lemma 3.1. The values of v^{ATS} and v^T are the lower bounds of the optimal values of $V^{ATS}(t^*)$ and V^T, respectively.

Proof: Since problem (P4) is a minimization problem, and the convex polyhedron that contains all feasible solutions is smaller than that of the relaxed version of problem (P4). Thus, $v^{ATS}(t^*) \leq V^{ATS}(t^*)$, and $v^T \leq V^T$ [126]. □

Lemma 3.2. The values of $\hat{V}^{ATS}(t^*, \boldsymbol{m})$, $\hat{V}^T(\boldsymbol{m})$ are the upper bounds of the optimal values of $V^{ATS}(t^*)$, V^T, respectively.

Proof: Since problem (P4) is a minimization problem, then we have $V^{ATS}(t^*) \leq \hat{V}^{ATS}(t^*, \boldsymbol{m})$, and $V^T \leq \hat{V}^T(\boldsymbol{m})$. □

Then, the upper and lower bounds of the difference between the optimal values of $V^{ATS}(t^*)$ and V^T can be stated as

$$V^T - V^{ATS}(t^*) \leq \hat{V}^T(\boldsymbol{m}) - v^{ATS}(t^*), \tag{3.51}$$

$$V^T - V^{ATS}(t^*) \geq v^T - \hat{V}^{ATS}(t^*, \boldsymbol{m}). \tag{3.52}$$

Algorithm 1: Iterative algorithm for obtaining the optimal t^*.

01: Initialize $pool = [1, 2, ..., T]$.
02: Calculating linear programming relaxation v^T.
03: **while** $pool \neq \emptyset$ **do**
04:   **for** ind in range(length($pool$)-1) **do**
05:     Randomly select one element in $pool$ as t_x.
06:     **if** length($pool$)==1, break **while**.
07:     $t_y = t_x + ind$.
08:     Calculating linear relaxation $v^{ATS}(t_x)$, $v^{ATS}(t_y)$.
09:     Randomly generate feasible solution $\boldsymbol{m}$, calculating $\hat{V}^{ATS}(t_x, \boldsymbol{m})$, $\hat{V}^{ATS}(t_y, \boldsymbol{m})$ and $\hat{V}^T(\boldsymbol{m})$.
10:     Calculating $A(t_x)$, $A(t_y)$, $B(t_x)$, $B(t_y)$.
11:     **if** $B(t_x) - A(t_y) > 0$ and $A(t_x) - B(t_y) > 0$,
12:       **then** Store t_y and update the $new.pool$.
13:     **else if** $B(t_x) - A(t_y) < 0$ and $A(t_x) - B(t_y) < 0$
14:       **then** break **if**.
15:     **else** go back to step 09.
16:   $pool = new.pool$. # $pool$ denotes comparison pool vector
17: **return** $t^* = t_x$.

For notation simplicity, we use $A(t_x)$ to denote $v^T - \hat{V}^{ATS}(t^* = t_x, \boldsymbol{m})$, and $B(t_x)$ to denote $\hat{V}^T(\boldsymbol{m}) - v^{ATS}(t^* = t_x)$, respectively. Then, the following theorem holds.

Theorem 3.1. If $B(t_x) - A(t_y) > 0$ and $A(t_x) - B(t_y) > 0$, $V^{ATS}(t^* = t_y) < V^{ATS}(t^* = t_x)$. Else, if $B(t_x) - A(t_y) < 0$ and $A(t_x) - B(t_y) < 0$, then $V^{ATS}(t^* = t_x) < V^{ATS}(t^* = t_y)$.

Proof: When $B(t_x) - A(t_y) > 0$ and $A(t_x) - B(t_y) > 0$, it means that the value of $[V^{ATS}(t^* = t_x) - V^{ATS}(t^* = t_y)]$ is bounded by two positive numbers, which are the upper and the lower bounds, respectively. Thus, $V^{ATS}(t^* = t_y) < V^{ATS}(t^* = t_x)$ can be obtained. Also, if $B(t_x) - A(t_y) < 0$ and $A(t_x) - B(t_y) < 0$, it means that the value of $[V^{ATS}(t^* = t_x) - V^{ATS}(t^* = t_y)]$ is always negative. Thus, we can derive that $V^{ATS}(t^* = t_y) > V^{ATS}(t^* = t_x)$. □

However, when $B(t_x) - A(t_y)$ and $A(t_x) - B(t_y)$ have the inconsistent signs, the feasible solution $\boldsymbol{m}$ should be randomly updated for another round of bound evaluation. Then, the iterative algorithm for obtaining the optimal revision period $\hat{t}^*$ can be described by **Algorithm 1**.

Theorem 3.2. The proposed iterative algorithm can guarantee that the obtained optimal revision period $\hat{t}^*$ is the same as that derived directly by the Branch-and-Bound algorithm.

Proof: Algorithm 1 exhaustively evaluates all pairs of $V^{ATS}(t^* = t_x) - V^{ATS}(t^* = t_y)$ based on any feasible solution $\boldsymbol{m}$. That means for each round of evaluation, the t_x which is the current candidate optimal t^* will be updated until the comparison pool is empty. At last the final value of t_x is the optimal revision period $\hat{t}^*$, i.e., $t_x = \hat{t}^* = \arg\min V^{ATS}$. $\square$

In comparison, the original computational complexity of solving problem (P4) is $\mathcal{O}(M\overline{b}^{\mathcal{D}_{\boldsymbol{m},\boldsymbol{\chi},\boldsymbol{t}^*}})$, where b is branching factors, and M is the time to explore a subproblem [107]. By applying the algorithm to fix the optimal revision period $\hat{t}^*$ first, the complexity can be reduced to $\mathcal{O}(M\overline{b}^{\mathcal{D}_{\boldsymbol{m},\boldsymbol{\chi}}}\overline{n})$, where $\overline{n} \leq \sum_{\overline{k}=1}^{\overline{n}}(N_{\overline{k}} - 1) \leq \sum_{\overline{k}=1}^{T-1}(\overline{k})$, and $\overline{b}^{\mathcal{D}_{\boldsymbol{m},\boldsymbol{\chi}}}\overline{n} << \overline{b}^{\mathcal{D}_{\boldsymbol{m},\boldsymbol{\chi},\boldsymbol{t}^*}}$. Note that $N_{\overline{k}}$ represents the number of $V^{ATS}(t^* = t_x)$ in the $pool$ at $\overline{k}_{th}$ comparison iteration, $N_1 = T$, and $N_1 > N_2 ... > N_n$. Based on Theorems 3.1 and 3.2, the optimal revision period t^* can be determined separately by the iterative algorithm, which significantly reduces the computational complexity. Note that the computational complexity depends on $\boldsymbol{m}$ and $\boldsymbol{\chi}$, without directly relating to the number of nodes of a PDS. It means the most relevant variable impacting the computational complexity is the number of damaged restoration paths, but not the number of nodes. Also, in practice, the number of restoration paths is restrained by the limited numbers of CLs and MEG candidate locations. Therefore, the increasing number of nodes of a PDS will not directly impact the computational complexity.

3.4 Case Study

For case studies, a PC with Intel CORE i7-4770 CPU and 8 GB DDR3 RAM, and Gurobi solver are used as a test platform. The proposed strategy is performed on the modified IEEE 123-Node Test Feeder and the historical data of the 1994 Northridge earthquake which occurred in Los Angeles, USA. In this section, the test system is set up. The simulation results on the MEG investment and pre-positioning and the MEG reallocation and repair scheduling are presented.

Table 3.1: Parameters of Critical Loads

Node Index	P_d (kW)	Q_d (kVar)	$\mathcal{I}_c$ $\times 10^3$	Node Index	P_d (kW)	Q_d (kVar)	$\mathcal{I}_c$ $\times 10^3$
34	50.79	26.74	9.5	59	34.33	18.12	9.8
32	37.28	45.74	9.2	66	53.24	36.71	9.4
33	17.35	7.92	8.8	81	29.23	27.35	8.4
14	36.98	19.49	9.1	86	39.08	15.67	9.6
45	81.28	41.09	8.5	98	39.29	30.74	9.3
56	65.17	21.78	8.3	105	23.45	22.73	8.8

Table 3.2: Available MEG Product List

MEG Type	P_d (kW)	Q_d (kVar)	Cost ($)	MEG Type	P_d (kW)	Q_d (kVar)	Cost ($)
T1	182	137	210k	T4	80	60	90k
T2	120	90	140k	T5	62	45	75k
T3	100	75	125k	T6	44	33	60k

3.4.1 Test System Setup and Historical Data Analysis

In this research, the IEEE 123-Node Test Feeder is chosen as the power distribution network after modification. It is originally an unbalanced three-phase system, while following the work in [68], is considered as a single-phase system in this study. The same setting is also employed in [43, 58, 60], that are selected as three state-of-art methods for comparisons. Specifically, the line parameters can be derived from [128]. A total of twelve CLs are randomly appointed, as listed in Table 3.1, of which the parameters are randomly generated based on [58]. A total of seventeen candidate locations are randomly generated for MEG deployment. The costs and parameters of MEGs are obtained based on products in [119], as listed in Table 3.2.

Moreover, the historical data of the 1994 Northridge earthquake is used to model the seismic impact. A coordinate of $[34°14'20.4''N, 118°30'54.0''W]$ within Northridge is selected as the location of the center of the distribution network. The reason is that this earthquake is very typical, which set a record for the highest peak ground acceleration in an urban area in North America, leading to severe damages on local PDSs in Los Angeles, USA. Specifically, the historical data containing the information of multi-shocks of earthquakes are accessed from the United States Geological

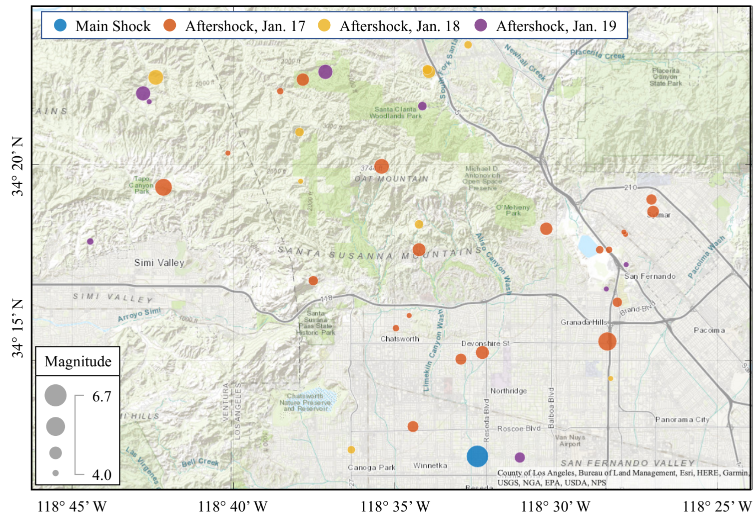

Figure 3.4: Historical earthquake data of the 1994 Northridge earthquake.

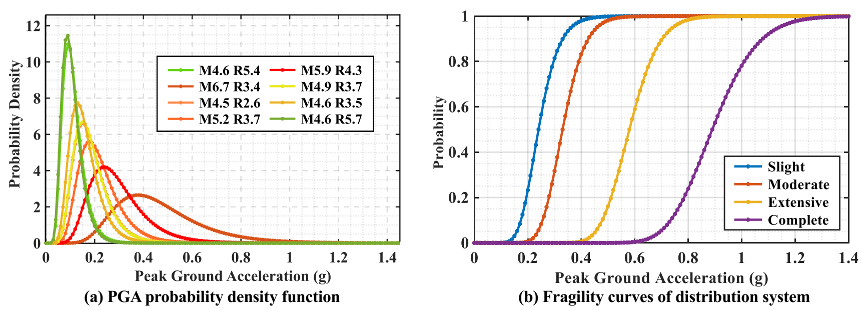

Figure 3.5: Earthquake data analysis in terms of PGA and fragility.

Survey [123]. A total of thirty-eight aftershocks of magnitude $M_L \geq 4.0$ in the former three days after the main shock are selected. Accordingly, the length of HHMMs is $B = 39$, which contains one main shock with magnitude and distance $\{M = 6.7, R = 3.4\}$, and thirty-eight aftershocks with their respective magnitudes and distances $\{M, R\}$, as shown in Fig. 3.4. Then, the PGA density function can be obtained for each shock. Lastly, by sampling the PGA density function, multiple PGA observation sequences $\boldsymbol{y}$ can be generated for RI evaluation.

To illustrate the PGA density function, some examples with different magnitudes and distances are shown in Fig. 3.5(a). We can see with the decreasing of magnitudes and the increasing of distances, the PGA density curves become narrow. It means that the more intensive and closer an earthquake is, the more likely the location of interest will experience a higher level of PGA. Moreover, we classify the

Table 3.3: RI of Restoration Path Based on HHMM

CL Index	Restoration Path/RI		
	1	2	3
CL-14	$3 \Rightarrow 14/0.4037$	$12 \Rightarrow 14/0.9617$	$18 \Rightarrow 14/0.1885$
CL-32	$22 \Rightarrow 32/0.6921$	$30 \Rightarrow 32/0.8408$	$18 \Rightarrow 32/0.6362$
CL-33	$22 \Rightarrow 33/0.4631$	$30 \Rightarrow 33/0.5723$	$18 \Rightarrow 33/0.4526$
CL-34	$3 \Rightarrow 34/0.5903$	$12 \Rightarrow 34/1.0000$	$18 \Rightarrow 34/0.7881$
CL-45	$18 \Rightarrow 45/0.3524$	$38 \Rightarrow 45/0.7685$	$22 \Rightarrow 45/0.2603$
CL-56	$53 \Rightarrow 56/1.0000$	$55 \Rightarrow 56/1.0000$	$93 \Rightarrow 56/0.5004$
CL-59	$53 \Rightarrow 59/0.7951$	$55 \Rightarrow 59/0.6123$	$160 \Rightarrow 59/0.3689$
CL-66	$160 \Rightarrow 33/0.6831$	$53 \Rightarrow 66/0.2563$	$54 \Rightarrow 66/0.1925$
CL-81	$77 \Rightarrow 81/0.7198$	$85 \Rightarrow 81/0.6015$	$160 \Rightarrow 81/0.2719$
CL-86	$77 \Rightarrow 86/0.6238$	$90 \Rightarrow 86/0.8629$	$93 \Rightarrow 86/0.5801$
CL-98	$160 \Rightarrow 98/0.9626$	$450 \Rightarrow 98/1.0000$	$104 \Rightarrow 98/0.4542$
CL-105	$103 \Rightarrow 105/0.339$	$113 \Rightarrow 105/0.2344$	$160 \Rightarrow 105/0.4546$

Note: The top 3 restoration paths ranked by RI for each CL are listed.

seismic impact on distribution networks into five states, which are normal, slight, moderate, extensive and complete states, corresponding to 0%, 4%, 12%, 50% and 80% of all DLs are damaged, respectively. Accordingly, the fragility curves can be developed, as shown in Fig. 3.5(b). Then, based on the fragility curves, we establish HHMM for each restoration path, and calculate the corresponding RI metric, the results are listed in Table 3.3.

3.4.2 MEG Investment and Pre-positioning

In this subsection, the MEG investment and pre-positioning is validated. Specifically, the derived RI metrics are integrated into the MEG investment and pre-positioning problem, which is solved within 0.82s. Fig. 3.6 shows the result of the MEG portfolio and pre-positioning given RI threshold $\overline{\mathcal{R}}_{tr} \geq 0.75$, where seven MEGs are invested. They are T3 for nodes 12, 38, 53, T4 for nodes 30, 77, 160, and T6 for node 450. The total investment cost is \$705K which can achieve the system average RI of 0.7850. Note that the higher the RI threshold $\overline{\mathcal{R}}_{tr}$ we choose, the higher the investment cost will be, because more MEGs are needed to support the desired resilience. For example, when $\overline{\mathcal{R}}_{tr} \geq 0.75$, CL-86 can be allocated with an alternative restoration path $77 \Rightarrow 86$ with a lower $RI = 0.6238$ instead of restoration path $90 \Rightarrow 86$ with higher $RI = 0.8629$. Also, the RI threshold is selected

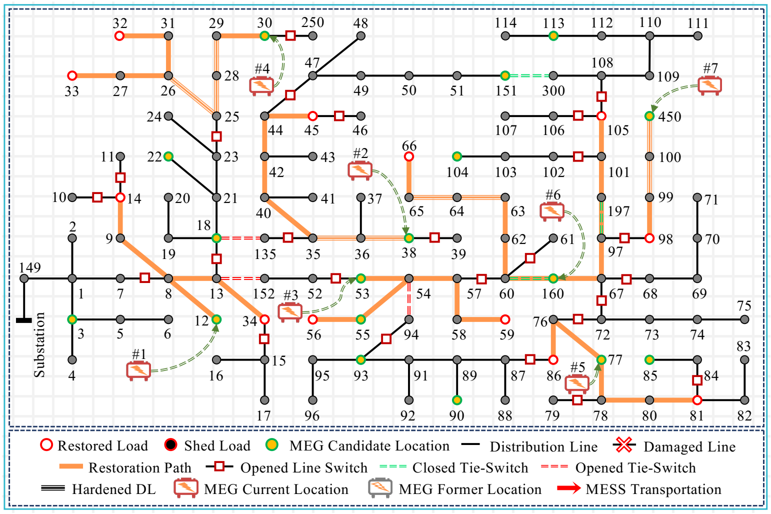

Figure 3.6: Results of investment and pre-positioning given $\overline{\mathcal{R}}_{tr} \geq 0.75$.

according to the system average RI. For illustration, in Fig. 3.7, we compare the total investment costs with respect to various values of $\overline{\mathcal{R}}_{tr}$. We can see that the system average RI improves along with the increasing of investment cost within a range of $\overline{\mathcal{R}}_{tr} \in [0.65, 0.8]$. Outside this range, both investment cost and system average RI remain constant. This is because when the RI threshold is very low ($\overline{\mathcal{R}}_{tr} < 0.65$), to ensure all the CLs can be assigned with an available MEG in the pre-disaster stage, the minimum investment is always used, which results in a fixed system average RI. When $\overline{\mathcal{R}}_{tr} > 0.8$, no further improvement in the system average RI can be gained, since the most resilient restoration paths of all CLs have already been utilized.

3.4.3 MEG Reallocation and Repair Scheduling

To demonstrate the effectiveness of MEG reallocation in dealing with post-restoration failures, a main shock of $M_L = 7.0$ is considered. Accordingly, the expected numbers of damaged DLs is 22, as shown in Fig. 3.8. The problem is solved in 0.73s. The total restored load priority ($\sum_{c \in \mathcal{C}} p_{cg} \mathcal{I}_c$) is 91.6. As highlighted by the red arrows in Fig. 3.8, only five transportation of MEGs are needed to deal with the damages caused by the main shock. Also, due to MEG capacity deficiency, CL-56 is shed. And, because of available path shortages, CL-33 is shed. By contrast, if there is no MEG reallocation, the total restored load priority will be reduced from

MEG	Type	Deployed Loc.	Restored CL
1	T1	Node-18	CL-14, CL-34, CL-45
2	T3	Node-53	CL-56, CL-59
3	T4	Node-30	CL-32, CL-33
4	T4	Node-77	CL-81, CL-86
5	T4	Node-160	CL-66, CL-105
6	T6	Node-450	CL-98

MEG	Type	Deployed Loc.	Restored CL
1	T2	Node-151	CL-45,CL-105
2	T3	Node-12	CL-14, CL-34
3	T3	Node-160	CL-66, CL-98
4	T3	Node-54	CL-56, CL-59
5	T4	Node-30	CL-32, CL-33
6	T4	Node-77	CL-81, CL-86

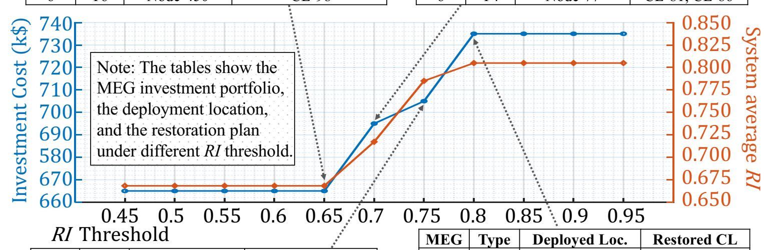

MEG	Type	Deployed Loc.	Restored CL
1	T3	Node-12	CL-14, CL-34
2	T3	Node-38	CL-45
3	T3	Node-53	CL-56, CL-59
4	T4	Node-30	CL-32, CL-33
5	T4	Node-77	CL-81, CL-86
6	T4	Node-160	CL-66, CL-105
7	T6	Node-450	CL-98

MEG	Type	Deployed Loc.	Restored CL
1	T3	Node-12	CL-14, CL-34
2	T3	Node-38	CL-45
3	T3	Node-53	CL-56, CL-59
4	T4	Node-30	CL-32, CL-33
5	T4	Node-160	CL-66, CL-105
6	T6	Node-77	CL-81
7	T6	Node-90	CL-86
8	T6	Node-450	CL-98

Figure 3.7: Comparison of different investment portfolio under various $\overline{\mathcal{R}}_{tr}$.

91.6 to 64.0, corresponding to CL-13, CL-33, CL-34, CL-45, and CL-105 being shed. This demonstrates the importance of considering restoration path RI, when deploying the MEGs against multi-shocks of earthquakes. In other words, by considering RI, not only the load can be restored, but also the resilience of restoration can be optimized against future shocks. Moreover, we can see that the line switches are opened to form electrical boundaries of restoration paths. Also, the tie-switches are operated to provide additional paths for restoration. For example, in Fig. 3.8, the normally opened tie-switch on tie-line $(18, 135)$ is closed after the earthquake, such that CL-45 can be restored by restoration path $18 \Rightarrow 45$. If there is no tie-switches, CL-45 will be shed since no available restoration path can be utilized.

Moreover, we use Case II with the worst damages to verify the effectiveness of the proposed repair scheduling problem. In this case, totally ten restoration paths need to be repaired. The values of τ_1 and τ_2 are set as 10 and 0.1, respectively. The repair time of a restoration path is $\Delta t = 6$ hours. Considering that only one crew team is available for dispatch, the results are shown in Table 3.4. The optimal objective value 8116.65 is obtained when the revision period $t^* = 6$. It means that the system operator will determine a repair schedule with length 5, and observe the uncertainties during time $t = 6$, then schedule the repair decisions after time $t = 6$ accordingly. The corresponding sequential repair decisions are shown in Table 3.5.

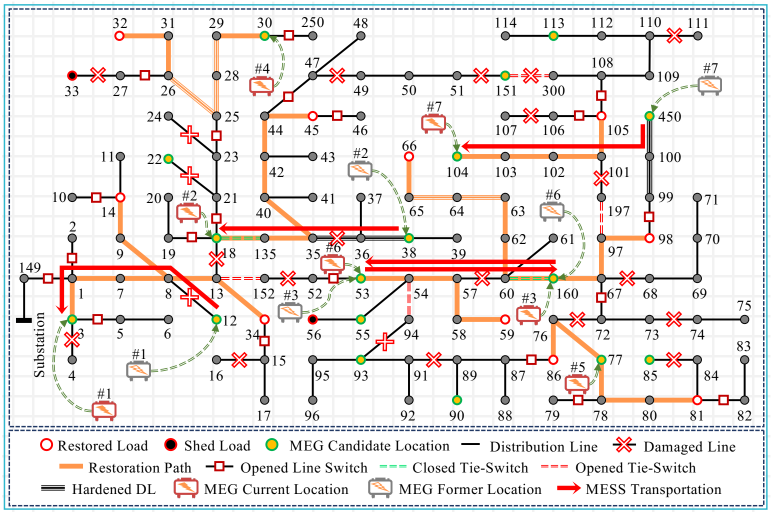

Figure 3.8: Results of MEG reallocation dealing with post-restoration failures.

Table 3.4: Objective Value of Different t^* Given One Crew Team

t^*	1	2	3	4	5
OBJ	8335.42	8253.04	8175.05	8124.25	8126.37
t^*	6	7	8	9	10
OBJ	8116.65	8155.80	8173.32	8270.98	8335.42

Another important feature of the proposed algorithm is that it can reduce the computational time to 32.3 minutes on the test platform, in comparison with the 126.7 minutes of the original Branch-and-Bound algorithm, with the same optimal solution being achieved. This feature is of particular importance for prompt response and decision making in between multi-shocks of earthquakes. Also, if two crew teams can be dispatched simultaneously, the repair horizon can be halved, as shown in Table 3.6. The optimal period for the system operator to observe the uncertainties is $t^* = 4$. Then, the sequential repair decisions for two teams can be derived. Specifically, crew team #1 will be responsible for repairing paths $18 \Rightarrow 34$, $30 \Rightarrow 33$, $85 \Rightarrow 81$, and crew team #2 will be assigned with paths $151 \Rightarrow 105$, $151 \Rightarrow 45$, $160 \Rightarrow 98$, respectively. We can also see that a more effective repair process can be achieved by adding one more crew team. As shown in Table 3.6, six repairs can be executed within three repair periods, compared with five repairs within five periods.

Table 3.5: Optimal Repair Decisions When Given One Crew Team ($t^* = 6$)

Period	1	2	3	4	5
Restoration Path	$30 \Rightarrow 33$	$151 \Rightarrow 45$	$160 \Rightarrow 98$	$85 \Rightarrow 81$	$18 \Rightarrow 34$
Period	6	7	8	9	10
Restoration Path	-	-	-	-	-

Table 3.6: Optimal Repair Decisions When Given Two Crew Teams ($t^* = 4$)

Crew team No. 1	Period	1	2	3
	Restoration Path	$18 \Rightarrow 34$	$30 \Rightarrow 33$	$85 \Rightarrow 81$
Crew team No. 2	Period	1	2	3
	Restoration Path	$151 \Rightarrow 105$	$151 \Rightarrow 45$	$160 \Rightarrow 98$

3.4.4 Comparison with Other Existing Strategies

To further validate the effectiveness of the proposed strategy, we compare it with the other ones presented in [43], [58], and [60]. Specifically, we have the following strategies:

- Strategy 1: The proposed strategy considering stochastic post-restoration failures against future shocks;
- Strategy 2: The strategy in [60] considering deterministic post-restoration failures without MEG investment;
- Strategy 3: The strategy in [43] without considering post-restoration failures and MEG investment;
- Strategy 4: The strategy in [58] using distributed generators considering deterministic post-restoration failures.

The PDS is struck by a main shock at 0 hours. And, three subsequent aftershocks occur at 2, 5 and 7 hours, respectively. The MEG transportation time is 1 hour. Also, we conduct 15 rounds of simulations with randomly generated damage scenarios to obtain an expected performance. The simulation results are shown in Fig. 3.9. We can see that our proposed strategy outperforms all the others in terms of restored CLs. This is benefited from the overall consideration of pre-disaster

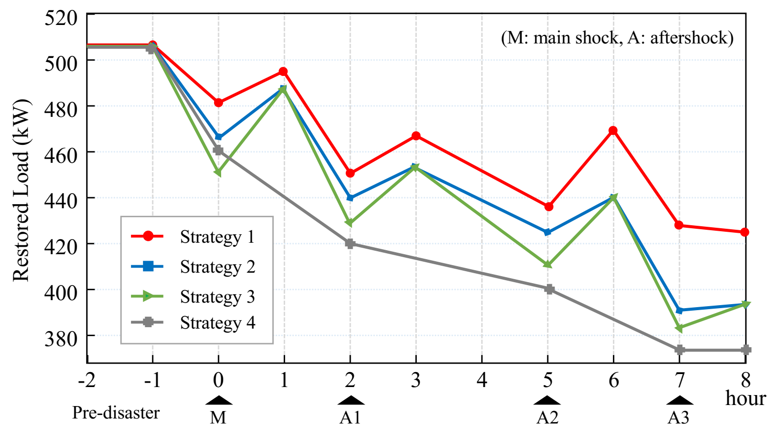

Figure 3.9: Comparative results of different strategies.

MEG investment and pre-positioning, and post-disaster MEG reallocation and repair scheduling against stochastic post-restoration failures caused by multi-shocks of earthquakes. Specifically, compared with Strategy 4, the value of the restored load bounces back a little after each shock. For example, at 0 hours when the main shock strikes, our strategy has a restored load of 481.7kW, while after MEG reallocation, the restored load can bounce back to 494.0kW. This demonstrates the flexibility of MEG reallocation in post-disaster restoration. Also, compared with Strategy 3, it can be concluded that the optimized MEG investment is very important. In other words, selecting MEG with random parameters can deteriorate the restoration performance. Compared with Strategy 2, it shows that our strategy can achieve a higher resilience. For example, at 0 hours when the main shock strikes, our strategy can have a restored load of 481.7kW even before MEG reallocation, whereas Strategy 2 can only restore 468.5kW. Also, at 6 hours after the main shock, the restored load of our strategy is even higher than the one at 3 hours after the second aftershock A2. The reason is that some damaged restoration paths are repaired such that the isolated load can be restored.

3.5 Summary

This chapter proposes a data-driven PDS resilience enhancement strategy against multi-shocks of earthquakes. The RI metric is developed based on HHMMs for stochastic resilience evaluation. The historical earthquake data are included into the HHMM as observed information of multi-shocks of earthquakes. Then, by employing the RI metric, the pre-disaster planning and the post-disaster response are investigated. Case studies based on the modified IEEE 123-Node Test Feeder and historical earthquake data of the 1994 Northridge earthquake demonstrate the proposed strategy. The results shows that 1) by considering RI, not only the load can be restored, but also the resilience of restoration can be optimized against future shocks of earthquakes; 2) the overall consideration of MEG investment, pre-positioning, reallocation, and repair scheduling against post-restoration failures caused by multi-shocks of earthquakes can achieve an improved restoration performance.

Chapter 4

Efficient MG Formation for Resilient PDSs Considering Large-Scale Deployment of MERs

MGs are promising solutions to improve PDS resilience against natural disasters. However, the existing MG formation approaches based on the LinDistflow model always demand MG roots and their corresponding topologies. This can result in an increased number of variables and constraints in the optimization problem, and deteriorate their computational performance. In this research, an adaptive LinDistflow model is proposed based on the single commodity flow model in graph theory. Specifically, we show that active and reactive powers can be represented as commodities, which are sent from one node to each of its adjacent nodes in the graph. Then, the power flow and nodal voltage calculation based on the commodity flow only requires adjacent node information of the original topology rather than various MG topologies caused by the dynamic deployment of MERs. Furthermore, by incorporating the adaptive LinDistflow model as constraints, a dynamic MG formation approach is proposed for resilient load restoration considering large-scale MER deployment. The problem is formulated as a mixed-integer nonlinear programming problem (MINLP). A linearization technique is proposed based on the propositional logic constraints. It employs the propositional logic that partitions the solution space into two separated regions. Accordingly, the region that the solution lies in can be selected linearly. The effectiveness of the proposed approach is

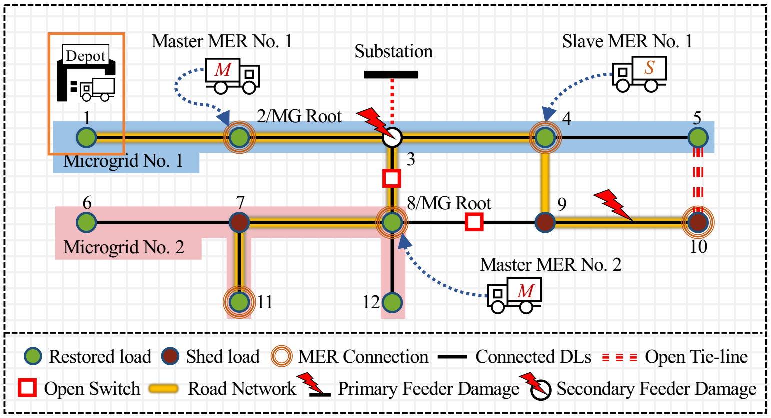

Figure 4.1: An illustration of the power distribution system model.

demonstrated based on the IEEE 37-Node, 123-Node and 8500-Node Test Feeders.

4.1 System Model

In this section, the PDS model and the LinDistflow model for MG formation are presented.

4.1.1 Power Distribution System Model

An illustration of the PDS model is shown in Fig. 4.1. Without loss of generality, it is based on the IEEE 13-Node Test Feeder [92]. Specifically, the PDS can be represented as a graph $G = (\mathcal{B}, \mathcal{E})$, where $\mathcal{B}$ is the set of nodes, and $\mathcal{E}$ is the set of lines. After natural disasters, the power supply from the bulk system can be interrupted, then MERs will be allocated to MER connection nodes for load restoration. Such nodes $\mathcal{C} \subseteq \mathcal{B}$ are equipped with electrical interfaces to connect MERs to PDSs [69]. In terms of control mode, MERs can be categorized into two types : master MERs (e.g., diesel generators, gas turbine generators, and storage systems), and slave MERs (e.g., wind turbines and photovoltaics) [53, 76, 129]. In particular, master MERs are capable of regulating voltage and frequency. By contrast, slave MERs, working in PQ control mode, can supply supplemental power to master MERs. Herein, we use θ_n^k and α_n^z to represent the deployment of master MERs and slave MERs, respectively. If $\theta_n^k = 1$, it means master MER k is deployed at node n. If $\alpha_n^z = 1$, it means that slave MER z is deployed at node n. Considering that road networks can be collapsed after natural disasters, the traffic information are included to model the transportation of MERs from the depot to MER connection nodes. Then, we use ζ_{dnr} to denote road status. If $\zeta_{dnr} = 0$, it means that the r_{th} road between the depot and node n is collapsed, and no MERs can be transported along this road.

Moreover, the nodes where master MERs located are served as the MG roots with reference voltage V_0. With respect to each root, a specific MG topology can be obtained. The MG topology refers to "the parent-child relationship of nodes with respect to the MG root" [68]. For example, in Fig. 4.1, node 3 is the parent node of node 8 with respect to MER connection node 2, whereas node 3 is the child node of node 8 with respect to MER connection node 11. Note that in a topological graph, a parent node is also called being on the upstream of its child nodes, and a child node is called being on the downstream of its parent node [130]. It implies that the MG topology will change along with the variation of the MG root. Moreover, RCSs will be operated for emergency operation. They can be divided into two groups: line switches and load switches [131]. The line switches can be opened to form boundaries between MGs, or to isolate the faults occurred on the primary feeders resulted by natural disasters. The load switches are used to shed loads when emergency power is deficient, or to clear the faults happened on the secondary network. Herein, we use s_{nm} to denote the status of line switch on DL (n, m), and it equals 0 if the line switch is opened. We use γ_n to denote the status of load switch at node n, and it equals 0 if the load switch is opened.

4.1.2 Linearized Distflow Model for Microgrid Formation

The LinDistflow model is widely utilized in power flow analysis in distribution networks. Compared with the bus injection model, power flow in the LinDistflow model can be calculated recursively, which can result in a more efficient computation [82]. Also, when the power losses along DLs are much smaller than the power flow, the LinDistflow model that neglects the nonlinear power losses term can be effective to calculate the power flow [94]. Therefore, all the MG formation approaches in [43, 68, 69, 72, 74–76] employ the LinDistflow model for power flow analysis. Specifically, the active and reactive power flow, and nodal voltages with respect to MER connection node $c \in \mathcal{C}$ can be given by [68, 94]

$$\sum\nolimits_{n \in \mathcal{H}^c(m)} P_{mn}^c = P_{hm}^c - (D_m^p - G_m^p - \Delta S_m^p), \tag{4.1}$$

$$\sum\nolimits_{n \in \mathcal{H}^c(m)} Q_{mn}^c = Q_{hm}^c - (D_m^q - G_m^q - \Delta S_m^q), \tag{4.2}$$

$$V_h^c - V_m^c = (r_{hm} P_{hm}^c + x_{hm} Q_{hm}^c)/V_0, \tag{4.3}$$

where $\mathcal{H}^c(m)$ is the set of child nodes of node m in the MG whose root is at MER connection node c. Also, P_{hm}^c and Q_{hm}^c represent the active and reactive power flow on DL (h, m) with respect to MER connection node c. Equations (4.1)-(4.3) imply the calculations of power flow and nodal voltages with respect to node c requires the topology of the MG whose root is at node c [132]. Hence, when the size of the set of MER connection nodes $(|\mathcal{C}|)$ increases, the number of power flow and nodal voltage calculation equations will also increase. This is where the MG formation approaches in [43, 68, 69, 72, 74–76] based on LinDistflow model are dependent on MG topologies, and their performance in computation will be deteriorated.

4.2 Adaptive Linearized DistFlow Model

In this section, an adaptive LinDistflow model for MG formation is proposed according to the LinDistflow model [94] and the single commodity flow in graph theory [133]. Firstly, we represent active and reactive powers as commodities and calculate the amount of commodities sent from each node to each of its adjacent nodes. Then, we show that active and reactive power flows can be derived from commodity flows when the MG roots are revealed by deploying master MERs. The meaning of the adaptive LinDistflow model is that it only requires the set of adjacent nodes of each node in the graph, without the need of various MG topology information. Hence, even though the MG topologies will change along with the deployment of master MERs, the calculations of power flow always remain the same. In other words, as long as the MER is deployed and the MG root node is revealed, the power flow can be calculated "adaptively", without needs of rewriting power flow equations. In the rest of this section, the adaptive LinDistflow model will be discussed in details.

4.2.1 Representing Power as Commodities

The single commodity flow in graph theory has been widely applied in minimum spanning tree problems [133]. In the single commodity flow model, one node is selected as the root node, which sends only one unit of commodity "1" to each other node. Taking the graph representation of a PDS in Subsection 2.1 as an example, the single commodity flow can be stated as

$$\sum_{h\in\mathcal{N}_m} f_{hm} - \sum_{h\in\mathcal{N}_m} f_{mh} = 1, \tag{4.4}$$

where $\mathcal{N}_m$ denotes the set of adjacent nodes of node m in the graph, thus node h is one of the adjacent nodes of node m. And, f_{hm} represents the commodity flow on line (h, m) in the direction from h to m. Note that even though the graph representation of a PDS is undirected, the commodity flow is directed, which means $f_{hm} \neq f_{mh}$ [134]. Also, equation (4.4) is used for commodity flow balances at each node. It means for any node $m \in \mathcal{B}$ in the graph, the commodities flow into node m is always one unit more than the commodities flow out of node m. In other words, the consumption of node m is always one unit of commodity. After rearrangement, equation (4.4) can be rewritten as

$$f_{nm} - f_{mn} = -\sum_{h\in\mathcal{N}_m\backslash n} f_{hm} + \sum_{h\in\mathcal{N}_m\backslash n} f_{mh} + 1, \tag{4.5}$$

where $\mathcal{N}_m\backslash n$ denotes the set of adjacent nodes of node m excluding node n. For notation simplicity, we use F_{nm} to denote $(f_{nm} - f_{mn})$. Note that F_{nm} is also directed, which means $F_{nm} \neq F_{nm}$. Then, by substituting, equation (4.5) can be rewritten as

$$\sum_{h\in\mathcal{N}_m\backslash n} F_{mh} = F_{nm} - 1. \tag{4.6}$$

Physically, F_{nm} represents how many units of commodities should be sent from node n to m in the graph, if node n is selected as the root node, such that the one unit consumption of node m can be satisfied.

Example 4.1. Fig. 4.2 (a) shows a graph with four nodes. According to the single commodity flow model, we have $F_{34} = 1$. It means that if node 3 is selected as

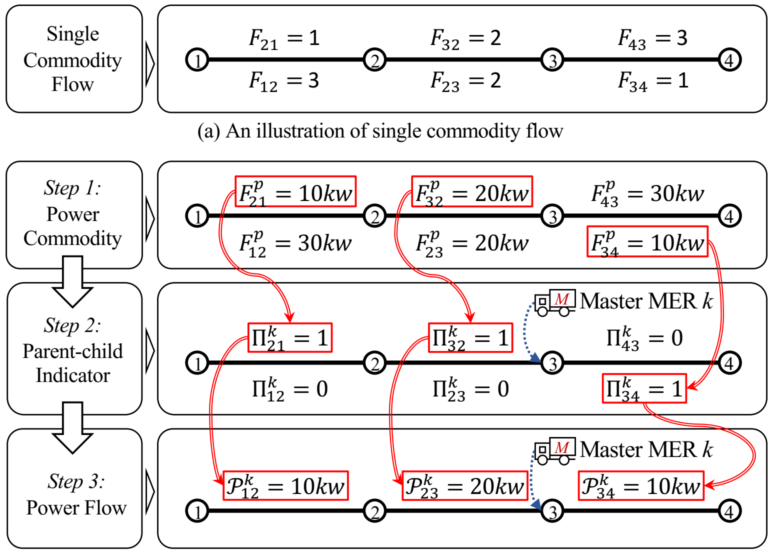

(a) An illustration of single commodity flow

(b) An illustration of power flow calculation based on commodity flow

Figure 4.2: An example of the proposed adaptive Linearized Distflow model.

the root node, it needs to send one unit of commodity to node 4. Also, we have $F_{23} = 2$, derived from $F_{34} = F_{23} - 1$. It means that if node 2 is selected as the root node, it needs to send two units of commodities to node 3. Similarly, it can be calculated by equation 4.6 that $F_{12} = 3$, $F_{21} = 1$, $F_{32} = 2$ and $F_{43} = 3$.

Inspired by the single commodity flow model, we can represent active and reactive power as commodities, and calculate how much active and reactive power commodities should be delivered from node n to m, if one node n is selected as the root node. Specifically, when commodity flow balances are considered in a radial PDS, which is already a spanning tree, the one unit commodity consumption "1" can be relaxed. In this sense, the one unit commodity consumption "1" at any node $m \in \mathcal{B}$ can be replaced by any real number consumption $\mathcal{R}_m$. Then, equation (4.6) can be rewritten as

$$\sum_{h \in \mathcal{N}_m \backslash n} F_{mh} = F_{nm} - \mathcal{R}_m. \tag{4.7}$$

If $\mathcal{R}_m$ is positive, it denotes the amount of commodity injected into node m. If $\mathcal{R}_m$ is negative, it denotes the amount of commodity withdrawn from node m. Moreover, considering that the active and reactive power are two types of commodities, we have $\mathcal{R}_m = (D^p_m - G^p_m - \Delta S^p_m)$ if the commodity is active power, or $\mathcal{R}_m = (D^q_m - G^q_m - \Delta S^q_m)$ if the commodity is reactive power. Then, equation (4.7) can be rewritten as

$$\textstyle\sum_{h \in \mathcal{N}_m \backslash n} F^p_{mh} = F^p_{nm} - (D^p_m - G^p_m - \Delta S^p_m), \tag{4.8}$$

$$\textstyle\sum_{h \in \mathcal{N}_m \backslash n} F^q_{mh} = F^q_{nm} - (D^q_m - G^q_m - \Delta S^q_m), \tag{4.9}$$

where F^p_{nm} and F^q_{nm} are the notations for F_{nm}, if active and reactive power are commodities, respectively. Also, ΔS^p_n and ΔS^q_n are the active and reactive load shed of node n, respectively, D^p_n and D^q_n are the active and reactive load demand of node n, respectively, and G^p_n and G^q_n are the active and reactive power generation at node n, respectively. Physically, F^p_{nm} and F^q_{nm} represent how much active and reactive power commodities should be delivered from node n to m, if node n is selected as the root node, such that the consumption of node m can be satisfied, respectively.

Example 4.2. Fig. 4.2 (b) shows a PDS with four electrical nodes. In step 1, we give an example of representing active power as commodity. We let $(D^p_m - G^p_m - \Delta S^p_m) = 10$kW for each node, which means each node has an equal active power consumption of 10kW. Then, by using equation (4.8), we have $F^p_{34} = 10$kW, $F^p_{23} = F^p_{34} + 10 = 20$kW, and $F^p_{12} = F^p_{23} + 10 = 30$kW. It means that if node 1 is selected as the root node, 30kW of active power commodity should be delivered from node 1 to 2 to satify the power consumption of each node. Similarly, we have $F^p_{21} = 10$kW, $F^p_{32} = F^p_{21} + 10 = 20$kW, and $F^p_{43} = F^p_{32} + 10 = 30$kW.

4.2.2 Power Flow Calculation Based on Commodity Flow

In this subsection, we show that active and reactive power flow can be calculated based on active and reactive commodity flows as long as the MG roots are revealed by deploying master MERs. Also, the calculation of nodal voltages is presented. Note that we employ the calligraphic font ($\mathcal{P}$, $\mathcal{Q}$, $\mathcal{V}$) to denote the active and reactive power and nodal voltages to distinguish from those of the LinDistflow model (P, Q, V).

Theorem 4.1. If node n is selected as the root node of graph G', then the amount of active and reactive power commodities delivered from node n to m (F^p_{nm}, F^q_{nm}) are equivalent to the active and reactive power flow on line (n, m) with respect to master MER k ($\mathcal{P}^k_{nm}$, $\mathcal{Q}^k_{nm}$), which is deployed at node n.

Proof. By deploying master MER k at node n, the MG root is revealed. Then, we have $\mathcal{P}^k_{nm} = P^{c=n}_{nm}$ and $\mathcal{Q}^k_{nm} = Q^{c=n}_{nm}$. Because equations (4.8)-(4.9) are equivalent to equations (4.1)-(4.2) if node n is selected as the root node of graph G' and the MG root at the same time, then we have $F^p_{nm} = P^{c=n}_{nm}$ and $F^q_{nm} = Q^{c=n}_{nm}$. Thus, we have $\mathcal{P}^k_{nm} = F^p_{nm}$ and $\mathcal{Q}^k_{nm} = F^q_{nm}$. $\square$

Furthermore, we can see that equations (4.8)-(4.9) are similar to equations (4.1)-(4.2). Nevertheless, the only difference is that the calculations of F^p_{nm} and F^q_{nm} are not with respect to any MER connection node c, hence requiring no MG topologies. In other words, to calculate F^p_{nm} and F^q_{nm}, the only information needed is the set of adjacent nodes of each node in graph G', i.e., $\mathcal{N}_m$, which always remains the same. By contrast, in equations (4.1)-(4.2), the calculations of P^c_{hm} and Q^c_{hm} need the MG topology information with respect to MER connection node c, i.e., $\mathcal{H}^c(m)$.

Theorem 4.2. For any line $(m, h) \in \mathcal{E}$, if node n becomes the root node of graph G' by deploying master MER k, and node h cannot be reached by node n without going through node m. Then, the active and reactive power flow on line (m, h) with respect to master MER k ($\mathcal{P}^k_{mh}$, $\mathcal{Q}^k_{mh}$) are equivalent to the amount of active and reactive power commodities delivered from node m to h when node m is the root node (F^p_{mh}, F^q_{mh}), respectively.

Proof. If node n is selected as the root node of graph G' by deploying master MER k, then we have $\mathcal{P}^k_{mh} = P^{c=n}_{mh}$. Thus, equation (4.1) can be used to calculate $\mathcal{P}^k_{mh}$, given by

$$\sum\nolimits_{h' \in \mathcal{H}^c(h)} P^{c=n}_{hh'} = \mathcal{P}^k_{mh} - (D^p_h - G^p_h - \Delta S^p_h), \tag{4.10}$$

Also, according to Theorem 4.1, if node m is selected as the root node of graph G', then we have $F^p_{mh} = P^{c=m}_{mh}$. Therefore, equation (4.1) can also be rewritten as

$$\sum\nolimits_{h' \in \mathcal{H}^c(h)} P^{c=m}_{hh'} = F^p_{mh} - (D^p_h - G^p_h - \Delta S^p_h), \tag{4.11}$$

Moreover, since node h' is on the downstream of both nodes n and m, equation (4.1) for the calculations of $P_{hh'}^{c=n}$ and $P_{hh'}^{c=m}$ are the same. Thus, from equations (4.10)-(4.11),we have $F_{mh}^{p} = \mathcal{P}_{mh}^{k}$. Similarly, we have $F_{mh}^{q} = \mathcal{Q}_{mh}^{k}$. □

According to Theorems 4.1 and 4.2, for any line $(n, m) \in \mathcal{E}$, if master MER k is allocated to MER connection node c, from which node n can be reached without going through node m, it means that node c is the MG root, and node m is the child of n. Then, the active and reactive power flow on line (n, m) with respect to master MER k ($\mathcal{P}_{nm}^{k}$,$\mathcal{Q}_{nm}^{k}$) is equivalent to the amount of active and reactive power commodities delivered from node n to m when node n is selected as the root node (F_{nm}^{p}, F_{nm}^{q}), i.e., $\mathcal{P}_{nm}^{k} = F_{nm}^{p}$ and $\mathcal{Q}_{nm}^{k} = F_{nm}^{q}$. If node m can be reached from node c without going through node n, the parent-child relationship of nodes n and m will be reversed. Hence, we have $\mathcal{P}_{nm}^{k} = F_{mn}^{p}$ and $\mathcal{Q}_{nm}^{k} = F_{mn}^{q}$. In other words, the active and reactive power flows can be derived from the active and reactive power commodities, given by

$$\begin{cases} \mathcal{P}_{nm}^{k} = F_{nm}^{p}, \mathcal{Q}_{nm}^{k} = F_{nm}^{q}, & \text{if } m \in \mathcal{H}^{c}(n), \\ \mathcal{P}_{nm}^{k} = F_{mn}^{p}, \mathcal{Q}_{nm}^{k} = F_{mn}^{q}, & \text{if } n \in \mathcal{H}^{c}(m), \end{cases} \tag{4.12}$$

where $m \in \mathcal{H}^{c}(n)$ means node m is the child node of n with respect to master MER k which is deployed at node c. To integrate the two options in equation (4.12) into one equation, a parent-child relationship indicator (denoted by Π_{nm}^{k}) is developed. Physically, if $\Pi_{nm}^{k} = 1$, it implies that node n is on the upstream of node m with respect to master MER k. Otherwise, if $\Pi_{nm}^{k} = 0$, it means that node n is on the downstream of node m with respect to master MER k. In other words, Π_{nm}^{k} can be used to represent the parent-child relationship between nodes n and m with respect to master MER k. Also, for one line (n, m), we have either $\Pi_{nm}^{k} = 1$ and $\Pi_{mn}^{k} = 0$, or $\Pi_{nm}^{k} = 0$ and $\Pi_{mn}^{k} = 1$, since node n is either on the upstream or on the downstream of node m with respect to master MER k. Then, equation (4.12) can be rewritten into two equations as

$$\mathcal{P}_{nm}^{k} = \Pi_{nm}^{k} F_{nm}^{p} + \Pi_{mn}^{k} F_{mn}^{p}, \tag{4.13}$$

$$\mathcal{Q}_{nm}^{k} = \Pi_{nm}^{k} F_{nm}^{q} + \Pi_{mn}^{k} F_{mn}^{q}. \tag{4.14}$$

Example 4.3. Step 2 in Fig. 4.2 (b) illustrates the parent-child relationship indicator

(Π^k_{nm}). If we deploy master MER k at node 3, it is clear that node 2 is on the upstream of node 1 with respect to master MER k, thus we have $\Pi^k_{32} = 1$. Similarly, we have $\Pi^k_{12} = 0$, $\Pi^k_{23} = 0$, $\Pi^k_{34} = 1$, $\Pi^k_{21} = 1$, and $\Pi^k_{43} = 0$.

Example 4.4. Step 3 in Fig. 4.2 (b) illustrates the calculation of active power flow from commidity flow based on equation (4.13). We have $\mathcal{P}^k_{12} = \Pi^k_{12}F^p_{12} + \Pi^k_{21}F^p_{21} = 0*30+1*10 = 10$kW. Also, we have $\mathcal{P}^k_{23} = F^p_{32} = 10$kW, and $\mathcal{P}^k_{34} = F^p_{34} = 10$kW.

The above discussion verifies the adaptivity of the proposed model. Specifically, it demonstrates that the power flow ($\mathcal{P}^k_{nm}$, $\mathcal{Q}^k_{nm}$) can be obtained from the commodity flow (F^p_{nm}, F^q_{nm}), as long as the parent-child relationship indicator (Π^k_{nm}) is revealed by deploying master MERs. Accordingly, if master MER k is allocated to MER connection node c, we have $\mathcal{P}^k_{nm} = P^c_{nm}$, and $\mathcal{Q}^k_{nm} = Q^c_{nm}$. Also, if master MER k is transported to another MER connection node c', we have $\mathcal{P}^k_{nm} = P^{c'}_{nm}$, and $\mathcal{Q}^k_{nm} = Q^{c'}_{nm}$. It implies that even though the deployment of master MER k is changed, the calculations of $\mathcal{P}^k_{nm}$ and $\mathcal{Q}^k_{nm}$ always remain the same, which are always with respect to master MER k, as described in equations (4.8)-(4.9) and (4.13)-(4.14). In other words, the calculations of $\mathcal{P}^k_{nm}$ and $\mathcal{Q}^k_{nm}$ are not dependent on MG topologies, then the adaptivity of the proposed model can be verified. By contrast, the calculations of P^c_{nm} and $P^{c'}_{nm}$ using equations (4.1)-(4.2) are completely different, since the MG root is changed from node c to c' and the topology is correspondingly changed.

Moerover, in the LinDistflow model, the voltage drop between nodes n and m with respect to MER connection node c can be stated as $\Delta V = (r_{nm}P^c_{nm} + x_{nm}Q^c_{nm})/V_0$, given by equation (4.3). It means that the parent-child relationship between nodes n and m with respect to MER connection node c is fixed, therefore we have either $\Delta V = V^c_n - V^c_m$, if node n is on the upstream of m, or $\Delta V = V^c_m - V^c_n$, if node n is on the downstream of m, depending on the MG topology. Similarly, in the adaptive linearized Distflow model, the voltage drop between nodes n and m can be obtained by $\Delta \mathcal{V} = (r_{nm}\mathcal{P}^k_{nm} + x_{nm}\mathcal{Q}^k_{nm})/V_0$. However, since it is calculated with respect to master MER k rather than MER connection node c, the dynamic deployment of master MER k can change the parent-child relationship of nodes n

and m. In this sense, we use the adaptive parent-child relationship indicator (Π_{nm}^k) to include various parent-child relationship of nodes n and m, when calculating the nodal voltages. The voltage drop can be stated as

$$\Delta\mathcal{V} = \Pi_{nm}^k(\mathcal{V}_n^k - \mathcal{V}_m^k) + \Pi_{mn}^k(\mathcal{V}_m^k - \mathcal{V}_n^k). \tag{4.15}$$

Physically, it means if node n is on the upstream of node m with respect to master MER k, i.e., $\Pi_{nm}^k = 1$ and $\Pi_{mn}^k = 0$, we have $\Delta\mathcal{V} = \mathcal{V}_n^k - \mathcal{V}_m^k$. Otherwise, if node n is on the downstream of node m with respect to master MER k, i.e., $\Pi_{nm}^k = 0$ and $\Pi_{mn}^k = 1$, we have $\Delta\mathcal{V} = \mathcal{V}_m^k - \mathcal{V}_n^k$. The values of Π_{nm}^k and Π_{mn}^k will be dynamically determined along with the deployment of master MER k. Note that because in the adaptive linearized Distflow model, the calculations of $\mathcal{P}_{nm}^k$ and $\mathcal{Q}_{nm}^k$ are independent of MG topologies, the nodal voltage $\mathcal{V}_n^k$ based on $\mathcal{P}_{nm}^k$, $\mathcal{Q}_{nm}^k$, and Π_{nm}^k is also obtained without the need of MG topologies. The only information required is if node n is an adjacent node of node m, and their parent-child relationship with respect to master MER k.

Example 4.5. In Fig. 4.2 (b), since master MER k is deployed at node 3, we have $\Pi_{32}^k = 1$ and $\Pi_{23}^k = 0$. In other words, node 3 is on the upstream of node 2 with respect to master MER k. Therefore, according to equation 4.15, we have $\mathcal{V}_3^k - \mathcal{V}_2^k = \Delta\mathcal{V}$.

4.2.3 Extension to the Application Considering Losses

The proposed adaptive LinDistflow model can be extended so that power losses can be considered. In particular, according to the second-order cone programming of the Distflow model [135], equations (4.8)-(4.9) and (4.15) can be rewritten as

$$\textstyle\sum_{h\in\mathcal{N}_m\backslash n} F_{mh}^p = F_{nm}^p - \tilde{F}_{nm}^p - (D_m^p - G_m^p - \Delta S_m^p), \tag{4.16}$$

$$\textstyle\sum_{h\in\mathcal{N}_m\backslash n} F_{mh}^q = F_{nm}^q - \tilde{F}_{nm}^q - (D_m^q - G_m^q - \Delta S_m^q), \tag{4.17}$$

$$\Delta\mathcal{V}^2 = \Pi_{nm}^k[(\mathcal{V}_n^k)^2 - (\mathcal{V}_m^k)^2] + \Pi_{mn}^k[(\mathcal{V}_m^k)^2 - (\mathcal{V}_n^k)^2]. \tag{4.18}$$

where $\tilde{F}_{nm}^p$ and $\tilde{F}_{nm}^q$ are continuous variables representing the active and reactive power losses, respectively. And, $\Delta\mathcal{V}^2 = 2(r_{nm}\mathcal{P}_{nm}^k + x_{nm}\mathcal{Q}_{nm}^k)$. Moreover, the following constraints are added for utilizing the second-order cone programming:

$$r_{nm}[(F^p_{nm})^2 + (F^q_{nm})^2] \leq \sum_{k\in\mathbb{K}} (\mathcal{V}^k_n)^2 \tilde{F}^p_{nm}, \tag{4.19}$$

$$x_{nm}[(F^p_{nm})^2 + (F^q_{nm})^2] \leq \sum_{k\in\mathbb{K}} (\mathcal{V}^k_n)^2 \tilde{F}^q_{nm}. \tag{4.20}$$

Note that $(\mathcal{V}^k_n)^2$ is not a quadratic term, but is regarded as a variable to denote the squared voltage magnitude. Compared with the proposed adaptive LinDistflow model, the extension considering power losses based on second-order cone programming can be computationally expensive. Since a fast response during outages after natural disasters is more important than power flow accuracy, the LinDistflow model that neglects the nonlinear power losses term can be more efficient with simple analytical solutions in terms of resilience-oriented strategies [94].

4.3 Dynamic Microgrid Formation Problem Formulation

In this section, a dynamic MG formation problem is proposed for large-scale deployment of MERs by incorporating the adaptive LinDistflow model as constraints. It is formulated as an MINLP problem to minimize the total weighted load shed and the total MER operational cost during outages after natural disasters. In the following, the problem formulation is presented and discussed in details.

4.3.1 Objective Function

Based on the adaptive Distflow model, the dynamic MG formation problem is formulated as an MINLP problem. The objective is to minimize the total weighted load shed cost and the total MER operational cost, given by

$$\min_{\boldsymbol{\theta},\boldsymbol{\alpha},\boldsymbol{s},\boldsymbol{\gamma}} \{(\tau c^{ls} \sum_{n\in\mathcal{B}} w_n \Delta S^p_n + c^{ms} \sum_{n\in\mathcal{C}} G^{p,ms}_n + c^{sl} \sum_{n\in\mathcal{C}} G^{p,sl}_n)\Delta h\}, \tag{4.21}$$

where $\boldsymbol{\theta}$, $\boldsymbol{\alpha}$, $\boldsymbol{s}$, and $\boldsymbol{\gamma}$ are the vectors for θ^k_n, α^z_n, s_{nm}, and γ_n, respectively. And Δh is the restoration duration. The first term in the bracket represents the total weighted load shed cost, and the second and third terms are the total master and slave MER operational costs. Note that loads are different in terms of load priorities [136].

For example, critical loads such as hospitals and water stations are considered more important than residential customers. Thus, a factor w_n is employed to denote the restoration priority of load at each node n. Also, τ is a weight factor used to prioritize the load shed term. It means that the optimizer will minimize the load shed first, and then minimize the total MER operational cost.

4.3.2 Constraints

1) Power Flow Constraints: When implementing the proposed adaptive Distflow model in the dynamic MG formation problem, the following constraints should be satisfied:

$$\textstyle\sum_{h\in\mathcal{N}_m\backslash n} F^p_{mh} = F^p_{nm} - (D^p_m - G^p_m - \Delta S^p_m) + \chi^p_{nm}, \tag{4.22}$$

$$\textstyle\sum_{h\in\mathcal{N}_m\backslash n} F^q_{mh} = F^q_{nm} - (D^q_m - G^q_m - \Delta S^q_m) + \chi^q_{nm}, \tag{4.23}$$

$$-(1-s_{nm})M \leq \chi^p_{nm}, \chi^q_{nm} \leq (1-s_{nm})M, \tag{4.24}$$

$$-s_{nm}M \leq F^p_{nm}, F^q_{nm} \leq s_{nm}M, \forall n \in \mathcal{B}, m \in \mathcal{N}_n, \tag{4.25}$$

$$\Pi^k_{nm} \leq \theta^k_n + (1-\theta^k_n)M, \forall n \in \mathcal{C}, m \in \mathcal{N}_n, k \in \mathbb{K}, \tag{4.26}$$

$$\Pi^k_{nm} \geq \theta^k_n - (1-\theta^k_n)M, \forall n \in \mathcal{C}, m \in \mathcal{N}_n, k \in \mathbb{K}, \tag{4.27}$$

$$\Pi^k_{nm} - \Pi^k_{mh} \leq -\theta^k_m, \forall n \in \mathcal{B}, m \in \mathcal{N}_n, h \in \mathcal{N}_m, k \in \mathbb{K}, \tag{4.28}$$

$$\Pi^k_{nm} + \Pi^k_{mn} = 1, \forall n \in \mathcal{B}, m \in \mathcal{N}_n, k \in \mathbb{K}, \tag{4.29}$$

$$0 \leq \Pi^k_{nm} \leq 1, \forall n \in \mathcal{B}, m \in \mathcal{N}_n, k \in \mathbb{K}, \tag{4.30}$$

$$\mathcal{P}^k_{nm} = \Pi^k_{nm} F^p_{nm} + \Pi^k_{mn} F^p_{mn}, \forall n \in \mathcal{B}, m \in \mathcal{N}_n, \tag{4.31}$$

$$\mathcal{Q}^k_{nm} = \Pi^k_{nm} F^q_{nm} + \Pi^k_{mn} F^q_{mn}, \forall n \in \mathcal{B}, m \in \mathcal{N}_n, \tag{4.32}$$

$$\begin{aligned}&\Pi^k_{nm}(\mathcal{V}^k_n - \mathcal{V}^k_m) + \Pi^k_{mn}(\mathcal{V}^k_m - \mathcal{V}^k_n)\\ &\quad = (r_{nm}\mathcal{P}^k_{nm} + x_{nm}\mathcal{Q}^k_{nm})/V_0, \forall n \in \mathcal{B}, m \in \mathcal{N}_n,\end{aligned} \tag{4.33}$$

$$V_0 - (1-\theta^k_n)M \leq V^k_n \leq V_0 + (1-\theta^k_n)M, \forall n \in \mathcal{C} \tag{4.34}$$

$$u_n^k\underline{V}-(1-u_n^k)M \leq V_n^k \leq u_n^k\overline{V}+(1-u_n^k)M, \forall n \in \mathcal{B}, \tag{4.35}$$

$$G_n^{p,ms} \geq \textstyle\sum_{m\in\mathcal{N}_n} \mathcal{P}_{nm}^k - (1-\theta_n^k)M, \forall n \in \mathcal{C}, \tag{4.36}$$

$$G_n^{p,ms} \leq \textstyle\sum_{m\in\mathcal{N}_n} \mathcal{P}_{nm}^k + (1-\theta_n^k)M, \forall n \in \mathcal{C}, \tag{4.37}$$

$$G_n^{q,ms} \geq \textstyle\sum_{m\in\mathcal{N}_n} \mathcal{Q}_{nm}^k - (1-\theta_n^k)M, \forall n \in \mathcal{C}, \tag{4.38}$$

$$G_n^{q,ms} \leq \textstyle\sum_{m\in\mathcal{N}_n} \mathcal{Q}_{nm}^k + (1-\theta_n^k)M, \forall n \in \mathcal{C}, \tag{4.39}$$

$$-\theta_n^k M \leq G_n^{p,ms} \leq \theta_n^k M, \forall n \in \mathcal{C}, \tag{4.40}$$

$$-\theta_n^k M \leq G_n^{q,ms} \leq \theta_n^k M, \forall n \in \mathcal{C}, \tag{4.41}$$

$$G_n^{p,ms} \leq \textstyle\sum_{k\in\mathbb{K}} \overline{P}_k^{ms}\theta_n^k + (1-\theta_n^k)M, \forall n \in \mathcal{C}, \tag{4.42}$$

$$G_n^{q,ms} \leq \textstyle\sum_{k\in\mathbb{K}} \overline{Q}_k^{ms}\theta_n^k + (1-\theta_n^k)M, \forall n \in \mathcal{C}, \tag{4.43}$$

$$Pr(G_n^{p,sl} \leq \textstyle\sum_{z\in\mathbb{Z}} \overline{P}_z^{sl}\alpha_n^z) \geq \eta, \forall n \in \mathcal{C}, \tag{4.44}$$

$$0 \leq G_n^{q,sl} \leq \textstyle\sum_{z\in\mathbb{Z}} \overline{Q}_z^{sl}\alpha_n^z, \forall n \in \mathcal{C}, \tag{4.45}$$

Constraints (4.22)-(4.23) are used to calculate the commodity flow when the commodities are the active and reactive powers, respectively. Constraint (4.24) enables the effectiveness of slack variables χ_{nm}^p and χ_{nm}^q, such that constraints (4.22)-(4.23) can be feasible when line (n, m) is disconnected. Constraint (4.25) forces the commodity flow on line (n, m) to 0, if the line is disconnected. Constraints (4.26)-(4.27) ensure that if $\theta_n^k = 1$, we have $\Pi_{nm}^k = 1$. It means that if master MER k is deployed at node n, then node n is on the upstream of all its adjacent nodes within the MG established by master MER k. Constraint (4.28) implies that if $\theta_m^k = 0$ and $\Pi_{nm}^k = 1$, we have $\Pi_{mh}^k = 1$. In other words, if master MER k is not deployed at node m, and node m is on the downstream of node n with respect to master MER k, then node h must be on the downstream of node m. Constraint (4.29) ensures that node n is either on the upstream or on the downstream of node m with respect to master MER k. It means that we have either $\Pi_{nm}^k = 1$ and $\Pi_{mn}^k = 0$, or $\Pi_{nm}^k = 0$ and $\Pi_{mn}^k = 1$. Constraint (4.30) is to determine the domain of Π_{nm}^k. Constraints (4.31)-(4.32) are used to derive the power flow from the commodity flow. Constraint (4.33) is to calculate the nodal voltages. Constraint (4.34) forces the voltage of node n to the reference voltage V_0, if node n is the location where master MERs are deployed. Constraint (4.35) ensures the nodal voltages are within an acceptable range $[\underline{V}, \overline{V}]$. Constraints (4.36)-(4.45) ensure that the demands are within MER generation capacity. Note that constraint (4.44) is used to model the power output uncertainties, when slave MERs are renewable energy sources. It is a chance constraint with a confidence level η [137]. For linearization, constraint (4.44) can be replaced by $0 \leq G_n^{p,sl} \leq \sum_{z\in\mathbb{Z}} \overline{P}_z^{sl} \alpha_n^z (1 + \sigma_n \Phi^{-1}(1-\eta))$, where Φ^{-1} is the inverse of the standard normal cumulative distribution function.

2) Post-disaster Operation Constraints: The post-disaster operation includes master MER and slave MER deployments, and line switch and load switch opening or closing operations, which should be limited by the following constraints:

$$\sum_{n\in\mathcal{C}} \theta_n^k \leq 1, \forall k \in \mathbb{K}, \tag{4.46}$$

$$\sum_{n\in\mathcal{C}} \alpha_n^z \leq 1, \forall z \in \mathbb{Z}, \tag{4.47}$$

$$\theta_n^k, \alpha_n^k \leq \sum_{r\in\mathbb{R}_{dn}} \zeta_{dnr}, \forall n \in \mathcal{B}, \tag{4.48}$$

$$\theta_n^k - \epsilon \leq u_n^k \leq \theta_n^k + 1, \forall n \in \mathcal{C}, k \in \mathbb{K}, \tag{4.49}$$

$$\sum_{k\in\mathbb{K}} u_n^k \leq 1, \forall n \in \mathcal{B}, \tag{4.50}$$

$$u_m^k \leq (1-\Pi_{nm}^k)+\Pi_{mn}^k + u_n^k, \forall n \in \mathcal{B}, m \in \mathcal{N}_n, k \in \mathbb{K}, \tag{4.51}$$

$$u_m^k \leq (1-\Pi_{nm}^k)+\Pi_{mn}^k+s_{nm}, \forall n \in \mathcal{B}, m \in \mathcal{N}_n, k \in \mathbb{K}, \tag{4.52}$$

$$0 \leq \Delta S_n^p \leq D_n^p, \forall n \in \mathcal{B}, \tag{4.53}$$

$$0 \leq \Delta S_n^q \leq D_n^q, \forall n \in \mathcal{B}, \tag{4.54}$$

$$-(1-\gamma_n)M+D_n^p \leq \Delta S_n^p \leq (1-\gamma_n)M+D_n^p, \forall n \in \mathcal{B}, \tag{4.55}$$

$$-(1-\gamma_n)M+D_n^q \leq \Delta S_n^q \leq (1-\gamma_n)M+D_n^q, \forall n \in \mathcal{B}, \tag{4.56}$$

$$\gamma_n = \sum_{k\in\mathbb{K}} u_n^k, n \in \mathcal{B}_l, \tag{4.57}$$

$$\gamma_n \leq 1 - \xi_n^s, \forall n \in \mathcal{B}, \tag{4.58}$$

$$u_n^k + u_m^k \le \xi_{nm}^p M, \forall (n,m) \in \mathcal{E}/\mathcal{E}_{sw}, \tag{4.59}$$

$$u_n^k + u_m^k \le (\xi_{nm}^p + (1 - s_{nm}))M, \forall (n,m) \in \mathcal{E}_{sw}, \tag{4.60}$$

$$\xi_{mh}^p \le \xi_{nm}^p, \forall (n,m) \in \mathcal{E}/\mathcal{E}_{sw}, \tag{4.61}$$

$$\xi_{mh}^p \le (1 - s_{mh}) + \xi_{nm}^p, \forall (m,h) \in \mathcal{E}_{sw}, \tag{4.62}$$

Constraints (4.46)-(4.47) ensure one MER can only be deployed at one MER connection node at a time. Constraint (4.48) means that MERs can not be transported to a node if all the possible roads between the depot and the node are collapsed. Constraint (4.49) implies that node n is energized by the MG established by master MER k, if this MER is deployed at node n. Constraint (4.50) means that one node can be energized by only one MG at a time. Constraints (4.51)-(4.52) mean that, for line (n, m), node m can be energized by the MG established by master MER k when satisfying the following conditions: i) node n is within this MG, ii) node n is on the upstream of node m with respect to this master MER k, and iii) line switch on DL (n, m) is closed. Constraints (4.53)-(4.54) gives the operator authority to flexibly determine the amount of load shed according actual demands. Constraints (4.55)-(4.56) imply that the system operator can disconnect one load from the grid by opening the load switch. Constraint (4.57) ensures power supply to key locations after natural disasters. It means that as long as the key location is covered by a MG, it will be restored by MERs. Constraint (4.58) means the load switch will open to isolate the faults happened on the secondary network under node n. Constraints (4.59)-(4.60) mean that if DL (n, m) is de-energized, nodes n and m on the two ends of this line can not belong to any MG. Constraint (4.61) indicates that if DL (n, m) is de-energized, its adjacent DL (m, h) can not be energized as well. A damaged DL on the primary network is in the de-energization status, and this status will propagate until it is isolated by line switches, which is model by constraint (4.62). Note that the damaged lines are identified by field crews dispatched by utility companies after natural disasters. Fault location algorithms, customer reports and expert judgments can also help in expediting the damage assessment process [138].

4.4 Dynamic Microgrid Formation Problem Solution

The proposed dynamic MG formation problem is an MINLP problem with nonlinear constraints, which are resulted from the adaptive LinDistflow model. Specifically, the nonlinearity is introduced from the quadratic terms $\Pi_{nm}^{k} F_{nm}^{p}$, $\Pi_{nm}^{k} F_{nm}^{q}$, and $\Pi_{nm}^{k}(\mathcal{V}_{n}^{k} - \mathcal{V}_{m}^{k})$ as given in constraints (4.31)-(4.32). To this end, a linearization technique is proposed based on the propositional logic constraints [139]. It employs propositional logic to divide the solution space into two separated regions. Then, the variable Π_{nm}^{k} is utilized to select the region that the solution lies in. After linearization, the proposed problem can be transformed from an MINLP problem into an MILP problem, and then be solved efficiently by the most commonly used Branch-and-Bound algorithm [140]. To demonstrate the advantages of the proposed dynamic MG formation approach in computation, comparisons in the number of variables and computational complexity are conducted between different approaches. In this section, the linearization technique and the computational comparison will be discussed in details.

4.4.1 Linearization Technique for Nonlinear Constraints

In the proposed dynamic MG formation problem, constraints (4.31)-(4.32) are nonlinear because of the quadratic terms $\Pi_{nm}^{k} F_{nm}^{p}$ and $\Pi_{nm}^{k} F_{nm}^{q}$. For linearization, the propositional logic constraint is employed [139]. For constraint (4.31), if $\Pi_{nm}^{k} = 1$, we have $\mathcal{P}_{nm}^{k} = F_{nm}^{p}$; if $\Pi_{mn}^{k} = 1$, we have $\mathcal{P}_{nm}^{k} = F_{mn}^{p}$. Since we have $\Pi_{nm}^{k} + \Pi_{mn}^{k} = 1$, as discussed in Subsection 3.2, the solution space of $\mathcal{P}_{nm}^{k}$ can be divided into two regions by Π_{nm}^{k}. Then, propositional logic constraints can be developed for constraint (4.31), given by

$$\mathcal{F}_{nm}^{pk} \leq F_{nm}^{p} + (1 - \Pi_{nm}^{k})M, \forall n \in \mathcal{B}, m \in \mathcal{N}_{n}, \tag{4.63}$$

$$\mathcal{F}_{nm}^{pk} \geq F_{nm}^{p} - (1 - \Pi_{nm}^{k})M, \forall n \in \mathcal{B}, m \in \mathcal{N}_{n}, \tag{4.64}$$

$$-\Pi_{nm}^{k} M \leq \mathcal{F}_{nm}^{pk} \leq \Pi_{nm}^{k} M, \forall n \in \mathcal{B}, m \in \mathcal{N}_{n}, \tag{4.65}$$

where $\mathcal{F}_{nm}^{pk}$ is an auxiliary variable for $\mathcal{P}_{nm}^{k}$. Constraints (4.63)-(4.65) imply that if $\Pi_{nm}^{k} = 1$, constraints (4.63)-(4.64) for Π_{nm}^{k} will be enforced, and constraint (4.65) for Π^k_{nm} will be relaxed. Then, we have $\mathcal{F}^{pk}_{nm}=F^p_{nm}$. Since $\Pi^k_{mn}=0$ when $\Pi^k_{nm}=1$, constraints (4.63)-(4.65) for Π^k_{mn} will be relaxed, and constraint (4.65) for Π^k_{mn} will be enforced. Accordingly, we have $\mathcal{F}^{pk}_{mn}=0$. In this sense, the auxiliary variables $\mathcal{F}^{pk}_{nm}$ and $\mathcal{F}^{pk}_{mn}$ can be used to calculate $\mathcal{P}^k_{nm}$, given by

$$\mathcal{P}^k_{nm} = \mathcal{F}^{pk}_{nm} + \mathcal{F}^{pk}_{mn}, \forall n \in \mathcal{B}, m \in \mathcal{N}_n, \tag{4.66}$$

which are linear constraints compared to constraint (4.31). Physically, the auxiliary variables $\mathcal{F}^{pk}_{nm}$ and $\mathcal{F}^{pk}_{mn}$ can be regarded as two solutions of $\mathcal{P}^k_{nm}$. One is for node n is on the upstream of node m, i.e., $\Pi^k_{nm} = 1$, the other is for node n is on the downstream of node m, i.e., $\Pi^k_{mn} = 1$, with respect to master MER k. Hence, Π^k_{nm} can be used in propositional logic to select the region of the solution space of $\mathcal{P}^k_{nm}$. Also, the discussions about $\mathcal{P}^k_{nm}$ are applied to $\mathcal{Q}^k_{nm}$. Then, constraint (4.32) can be linearized by

$$\mathcal{F}^{qk}_{nm} \le F^q_{nm} + (1-\Pi^k_{nm})M, \forall n \in \mathcal{B}, m \in \mathcal{N}_n, \tag{4.67}$$

$$\mathcal{F}^{qk}_{nm} \ge F^q_{nm} - (1-\Pi^k_{nm})M, \forall n \in \mathcal{B}, m \in \mathcal{N}_n, \tag{4.68}$$

$$-\Pi^k_{nm}M \le \mathcal{F}^{qk}_{nm} \le \Pi^k_{nm}M, \forall n \in \mathcal{B}, m \in \mathcal{N}_n, \tag{4.69}$$

$$\mathcal{Q}^k_{nm} = \mathcal{F}^{qk}_{nm} + \mathcal{F}^{qk}_{mn}, \forall n \in \mathcal{B}, m \in \mathcal{N}_n. \tag{4.70}$$

Moreover, since $\Pi^k_{nm}(\mathcal{V}^k_n - \mathcal{V}^k_m)$ are quadratic terms, constraint (4.33) are nonlinear. Similarly, by using the propositional logic constraints, it can be linearized as

$$\mathcal{V}^k_n - \mathcal{V}^k_m \le (r_{nm}\mathcal{P}^k_{nm} + x_{nm}\mathcal{Q}^k_{nm})/V_0 + (1-\Pi^k_{nm})M, \tag{4.71}$$

$$\mathcal{V}^k_n - \mathcal{V}^k_m \ge (r_{nm}\mathcal{P}^k_{nm} + x_{nm}\mathcal{Q}^k_{nm})/V_0 - (1-\Pi^k_{nm})M, \tag{4.72}$$

which imply that if $\Pi^k_{nm} = 1$, the voltage drop between node n and m, which is $(r_{nm}\mathcal{P}^k_{nm} + x_{nm}\mathcal{Q}^k_{nm})/V_0$, will be calculated by $\mathcal{V}^k_n - \mathcal{V}^k_m$. Otherwise, if $\Pi^k_{nm} = 0$, constraints (53)-(54) for Π^k_{nm} will be relaxed, while for Π^k_{mn} will become enforced to calculate the voltage drop. Then, we have $\mathcal{V}^k_m - \mathcal{V}^k_n = (r_{nm}\mathcal{P}^k_{nm} + x_{nm}\mathcal{Q}^k_{nm})/V_0$. In addition, after linearization, the dynamic MG formation problem, which is an MINLP problem, can be transformed into an MILP problem, and then be solved efficiently by the most commonly used Branch-and-Bound algorithm [140].

Table 4.1: Comparison of Different MG Formation Approaches

——	Approach in [68]	Approach in [74]	Approach in [75]
Binary	u_n^c, s_{nm}	s_{nm}	u_n^c, s_{nm}
# of Binary	$\|\mathcal{B}\|\|\mathcal{C}\| + \|\mathcal{E}\|$	$\|\mathcal{E}\|$	$\|\mathcal{B}\|\|\mathcal{C}\| + \|\mathcal{E}\|$
Continuous	P_{nm}^c, Q_{nm}^c, V_n^c	P_{nm}^c, Q_{nm}^c, V_n^c, f_{nm}	P_{nm}^c, Q_{nm}^c, V_n^c, f_{nm}^h
# of Continuous	$3\|\mathcal{E}\|\|\mathcal{C}\|$	$4\|\mathcal{E}\|\|\mathcal{C}\| + 2\|\mathcal{E}\|$	$4\|\mathcal{E}\|\|\mathcal{C}\| + 2\|\mathcal{E}\|\|\mathcal{N}\|$
Complexity	$2^{(\|\mathcal{B}\|\|\mathcal{C}\|+\|\mathcal{E}\|)}$	$2^{\|\mathcal{E}\|}$	$2^{(\|\mathcal{B}\|\|\mathcal{C}\|+\|\mathcal{E}\|)}$

——	Proposed Approach
Binary	u_n^k, s_{nm}
# of Binary	$\mathcal{P}_{nm}^k$, $\mathcal{Q}_{nm}^k$, V_n^k, F_{nm}^p, F_{nm}^q, Π_{nm}^k
# of Continuous	$5\|\mathcal{E}\|\|\mathbb{K}\| + 2\|\mathcal{E}\|$
Complexity	$2^{(\|\mathcal{B}\|\|\mathbb{K}\|+\|\mathcal{E}\|)}$

4.4.2 Comparisons in terms of Computation

To illustrate the computational advantages of the dynamic MG formation approach based on the adaptive LinDistflow model, comparisons are conducted between the proposed approach and other approaches in [68, 74, 75]. Specifically, the comparisons in terms of the number of binaries, the number of continuous variables, and the computational complexity are conducted. The results are shown in Table 4.1. It can be seen that other than the approach in [74], the proposed approach can achieve the least number of binary variables than the approaches in [68, 75], when $|\mathcal{C}| \geq |\mathbb{K}|$. Accordingly, it can also achieve the least computational complexity, which is $\mathcal{O}(2^{(|\mathcal{B}||\mathbb{K}|+|\mathcal{E}|)})$. Note that the requirement that $|\mathcal{C}| \geq |\mathbb{K}|$ can be easily satisfied, because the number of MER connection nodes ($|\mathcal{C}|$) in PDSs is typically more than the number of master MERs ($|\mathbb{K}|$), such that the flexibility of MERs can be utilized [51]. For the approach in [74], even though it has the least number of binary variables than all other approaches, it may result in suboptimality [74]. The reason is because by dropping binary variable u_n^c, the energization status of each node is not optimized. In other words, the loads in isolated islands without MERs allocated, which should have been shed, but are not included in the objective value. Also, the proposed approach can achieve the lowest number of continuous variables among all approaches, when $|\mathcal{C}| \geq 5/3|\mathbb{K}|$. Again, this requirement can be easily satisfied, especially for large-scale MER deployment.

The reason that the proposed dynamic MG formation approach can achieve a reduced number of binary and continuous variables is that we apply the proposed adaptive LinDistflow model, which is independent of MG topologies. In the proposed approach, the power flows and nodal voltages ($\mathcal{P}_{nm}^k$, $\mathcal{Q}_{nm}^k$, $\mathcal{V}_n^k$) and the node energization indicators (u_n^k) are calculated with respect to master MER k. By contrast, in the approaches in [68, 74, 75] based on the LinDistflow model, these continuous variables (P_{nm}^c, Q_{nm}^c, V_n^c) and binary variables (u_n^c) are calculated with respect to MER connection node c. It means that MG topologies with node c being the root are always required, therefore more power flow and nodal voltage variables are needed, especially when $|\mathcal{C}|$ becomes larger. In summary, the proposed approach has advantages at the number of continuous and binary variables and the computational complexity, which can achieve a better performance in computation. This is benefited from applying the proposed adaptive LinDistflow model for MG formation.

4.5 Case Study

To demonstrate the effectiveness of the proposed MG formation approach, a PC with Intel CORE i7-4770 and 8 GB DDR3 RAM is selected as test platform. The Gurobi is utilized to solve the MILP problem [141]. The case studies are performed based on the IEEE 37-Node, 123-Node and 8500-Node Test Feeders [92]. Two types of loads are considered, which are critical loads with weight $w_n = 10^4$, and non-critical loads with weight $w_n = 1$. The acceptable voltage range is set to $[0.95, 1.05]$ p.u. The load shed cost is $c^{ls} = 14\$/\text{kWh}$. The operational costs of master and slave MERs are $c^{ms} = 0.5\$/\text{kWh}$ and $c^{sl} = 0.1\$/\text{kWh}$, by assuming that master MERs are truck-mounted battery energy storage systems and slave MERs are truck-mounted photovoltaic systems, respectively. The restoration duration is $\Delta h = 10\text{h}$. In the rest of this section, the simulation results are presented and discussed.

4.5.1 Case Study I: IEEE 37-Node Test Feeder

In this case study, the effectiveness of the dynamic MG formation approach is demonstrated based on the modified IEEE 37-Node Test Feeder [92]. Specifically, one tie-line is newly added between nodes 725 and 741. The load demands are the same as those in [68]. Four critical loads are distributed at nodes 704, 705, 730 and 734, respectively. A total of twelve nodes can be used for MER connection. Also, there are four master MERs with generation capacity $\overline{P}_k^{ms}$=182kW and $\overline{Q}_k^{ms}$=137kVar, and six slave MERs with generation capacity $\overline{P}_z^{sl}$=100kW and $\overline{Q}_z^{sl}$=75kVar are available for restoration.

1) Restoration When Utility Power Unavailable: In this subcase, the dynamic MG formation approach is validated considering that natural disasters only cause damages on the bulk system and the utility power is unavailable. The problem is solved within 11.54s of wall time. The total load shed cost is 0, which implies all the loads are restored. The total MER operational cost is $\$2,510.5$, which is resulted by the deployment of three master MERs and six slave MERs. It indicates that even though there are four master MERs and six slave MERs, not all of them should be utilized considering the operational cost. Moreover, the deployment of MERs is shown in Fig. 4.3, where master MERs from #1 to #3 are transported to MER connection nodes 730, 705 and 737, establishing four MGs from #1 to #3, respectively. The line switches $(702, 703)$, $(708, 709)$ and $(711, 738)$ are open to form MG boundaries. The slave MERs from #1 to #6 are allocated to MER connection nodes 709, 744, 720, 710, 711 and 706, supplying supplemental power, and maintaining the nodal voltages within an acceptable range $[0.95, 1.05]$. In particular, MG #2 contains the most number of slave MERs, since the load demands within MG #2 equals 448.7kW, which is the highest among all MGs. Thus, more MERs are needed for restoration. In addition, it can be demonstrated that slave MERs are very useful in voltage regulation. For example, Fig. 4.4 depicts the results of nodal voltages, which are all within the limitation. Nevertheless, if we force all the slave MERs to the roots of their MGs, which means the voltage regulation cannot be fully implemented, the load shed will be increased to 460.85kW. It means more load should

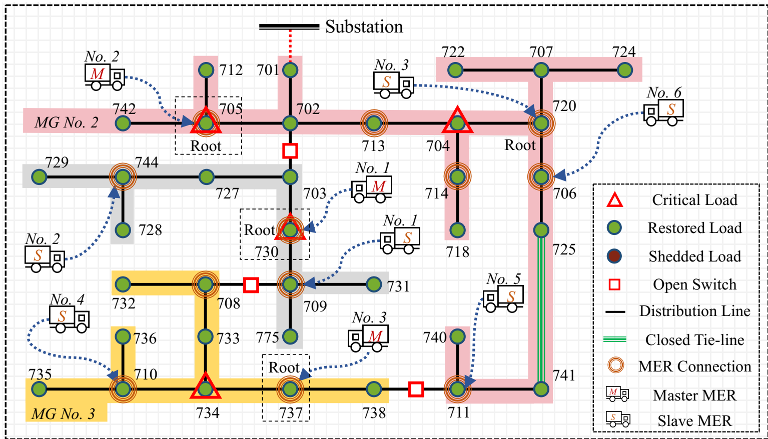

Figure 4.3: Results of IEEE 37-Node Test Feeder when only utility power unavailable.

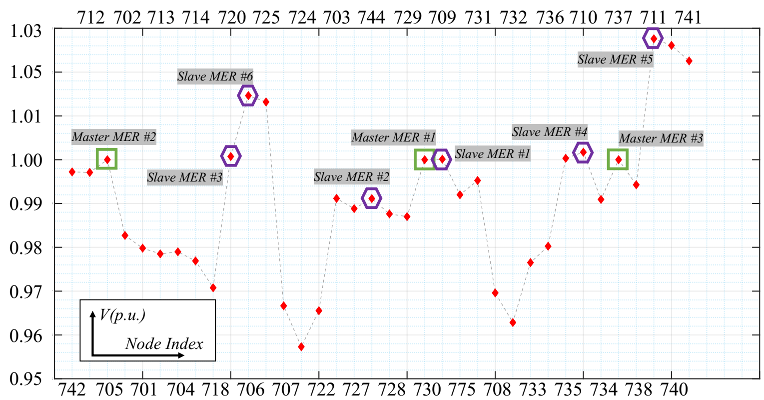

Figure 4.4: Results of nodal voltages after restoration.

be shed to meet the requirement of voltage limitation, even though the generation capacity is sufficient.

2) Restoration When Damages Occur on PDSs: In this subcase, not only the utility power is unavailable after natural disasters, but also three damages occur on both of the primary and secondary feeders. The problem is solved within 14.12s of wall time. The simulation results are shown in Fig. 4.5. Specifically, the total weighted load shed is 88.23kW. The total MER operational cost is $\$2,869.5$, which includes $\$2,469.5$ of four master MERs' operation and $\$400.0$ of four slave MERs' operation. Note that considering the minimization of the MER operational cost, only four out of six available slave MERs are utilized. Also, in Fig. 4.5, nodes 710, 735, 736 and 742 are shed due to shortages of master MERs, and node 722

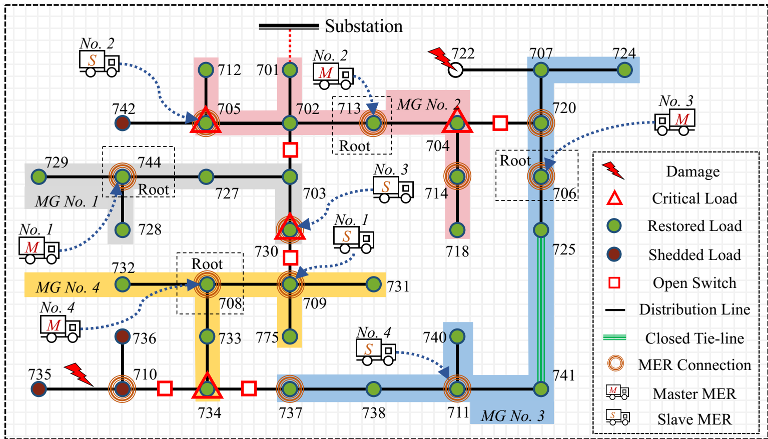

Figure 4.5: Results of IEEE 37-Node Test Feeder when damages occur on PDSs.

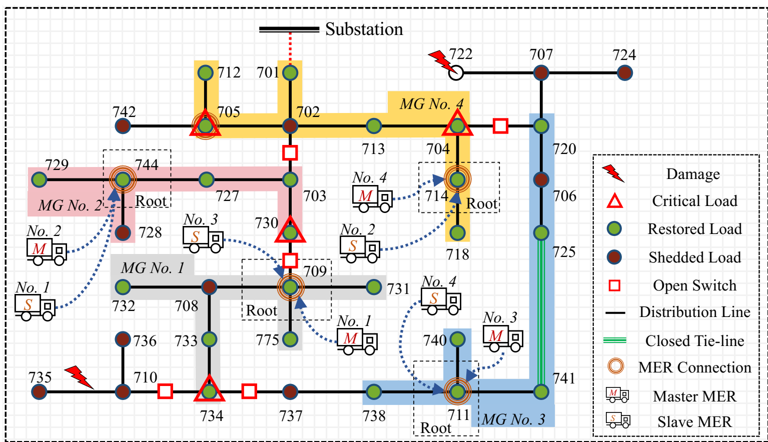

Figure 4.6: Results when limiting MER connection nodes to four.

is not restored because of generation capacity deficiency in MG #3. The tie-line $(725, 741)$ is closed such that nodes 711, 737, 738, 740 and 741 can be transferred to MG #3 to get emergency services. If there is no tie-line, the total weighted load shed will be increased to 218.24kW.

In addition, we would like to emphasize that the number of MER connection nodes has a significant impact on the performance of restoration. For example, if the number of MER connection nodes is reduced from twelve to eight, which are nodes 705, 708, 709, 710, 711, 714, 720 and 744, the total load shed will be increased from 88.23kW to 114.05kW. And, if we are given only four MER connection nodes 709, 711, 714 and 744, then the total load shed will be further increased to 271.84kW. These additional load shed are resulted by the limited number of MER connection nodes, rather than generation capacity deficiency. In other words, even though the load demand can be satisfied by generation, load shed can still happen when the MER connection nodes are not sufficient for MER deployment to maintain the nodal voltages within an acceptable range. For example, the solution to the MG formation of only four MER connection nodes 709, 711, 714 and 744 can be shown in Fig. 4.6. The generation and demands of each MG are listed in Table 4.2. We can see that the load demands covered by each MG is lower than the corresponding generation capacity, which means the load demands of all the MGs can be satisfied by the generation capacity. However, not all the covered load in each MG are restored, since the limited MER connection nodes are not sufficient for MER deployment that can restore all the covered load and maintain the nodal voltage within the limitation at the same time.

To further analyze the impact of the MER connection nodes on the performance of restoration, we randomly generate 100 samples of four nodes, and then calculate their average total load shed. We also do the same sampling for twelve, eight, twelve, sixteen and twenty MER connection nodes. The results are listed in Table 4.3. We can see that the average total load shed decreases, and the MER average utilization rate increases, along with the increase of the number of MER connection nodes. This demonstrates that the performance of restoration can be improved by large-scale MER deployment. It also indicates that if we want to well-utilize the flexibility of MERs, sufficient number of MER connection nodes equipped with electrical infrastructures are required. Otherwise, MERs cannot be well taken advantage of. Moreover, in terms of computational time, Table 4.3 shows that it increases when the number of MER connection node increases. The reason is that the solution space will become more complicated, when the scale that can be used to deploy the MERs gets larger.

4.5.2 Case Study II: IEEE 123-Node Test Feeder

In this case study, the effectiveness of the dynamic MG formation will be further validated on the modified IEEE 123-Node Test Feeder. Specifically, two tie-lines $(48, 250)$ and $(66, 104)$ are added. The load demands are randomly generated ac-

Table 4.2: Generation Capacity and Load Demands of MGs

MG Index	No. 1	No. 2	No. 3	No. 4
Generation Capacity	282kW	282kW	282kW	282kW
Load Covered	192.8kW	222.6kW	220.9kW	197.1kW
Load Restored	170.0kW	181.5kW	180.3kW	178.4kW

Table 4.3: Comparisons of MER Connection Nodes for Case I

Load Shed	Number of MER Connection Nodes				
	4	8	12	16	20
Min.	273.0kW	91.5kW	88.2kW	88.2kW	88.2kW
Avg.	488.7kW	254.8kW	142.5kW	107.3kW	92.5kW
Max.	724.9kW	559.1kW	329.5kW	310.9kW	177.4kW
Avg. UR	43.74%	64.48%	74.43%	77.55%	78.87%
Avg. CT	8.81s	10.82s	13.17s	14.92s	15.60s

Note: Utilization Rate (UR)=Total Restored Load Demand/Total MER Generation Capacity. CT: Computational Time.

cording to [68]. Thirty-six nodes are utilized as MER connection nodes. Nine critical loads are at nodes 07, 23, 38, 50, 60, 55, 73, 87, 98, and 105, respectively. Nodes 07 and 105 are selected as two key locations that should be restored as long as they are covered by MGs. A total of there are six master MERs with generation capacity $\overline{P}_k^{ms}$=410kW and $\overline{Q}_k^{ms}$=310kVar, and six slave MERs with generation capacity $\overline{P}_z^{sl}$=250kW and $\overline{Q}_z^{sl}$=170kVar are available for load restoration. A total of twelve damages occur on both of the primary and secondary feeders. The traffic information are considered through collapsed roads that can hinder the transportation of MERs. The depot is located at node 104. The confidence level $\eta = 0.9$ and deviation $\sigma_n = 0.1$ are assumed for the uncertain outputs of MERs. The restoration result is shown in Fig. 4.7. The total weighted load shed is 579.31kW, where nodes 44, 149 and 450 are shed because of generation capacity deficiency. Such a result is determined by considering the MER output uncertainties. If the uncertainties are not included in the optimization, the total weighted load shed will be decreased to 546.71kW. In other words, a more conservative solution can be achieved by considering the uncertainties, such that the solution can be robust to deal with the worst-case scenario. From Fig. 4.7, we can observe that the system operator

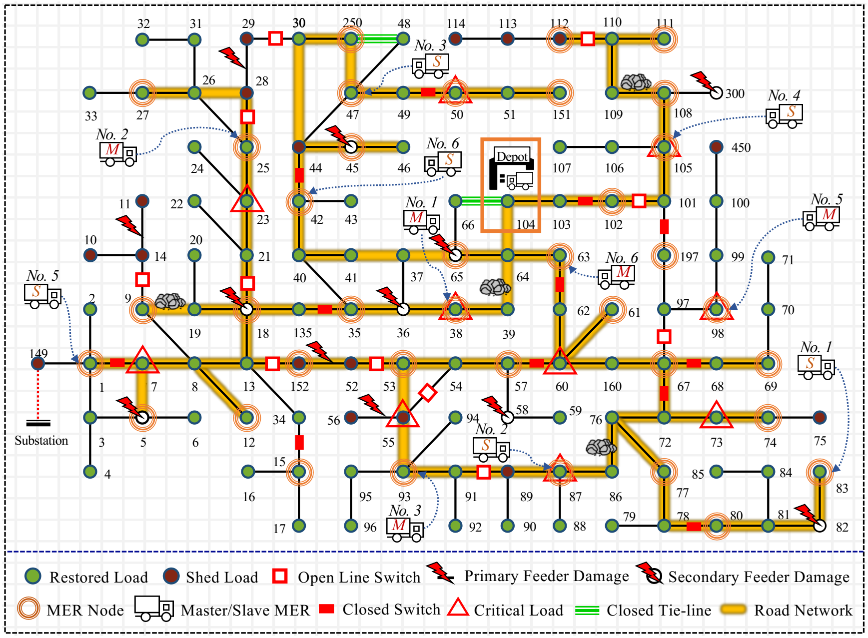

Figure 4.7: Results of IEEE 123-Node Test Feeder.

ensures power supply to the key locations at nodes 7 and 105, because they can be covered by MGs established by MERs. Also, it can be shown that line switches are very effective in isolating faults. For example, after natural disasters, DL $(52, 152)$ is damaged. Accordingly, line switches $(13, 152)$ and $(52, 53)$ are open to prevent the fault from propagating. In other words, nodes 52 and 152 are isolated by line switches so that the fault will not affect the other parts of the PDS. Similarly, damages occur on the secondary network under node 65, thus the load switch is open to isolate the fault. Furthermore, it can be shown that the traffic information can hinder the transportation of MERs. For example, in Fig. 4.7, nodes 112, 113 and 114 are shed because the only road between nodes 108 and 109 is collapsed, hence no MERs can be transported to node 122 to establish a MG.

In addition, the same evaluation of the impact of the number of MER connection nodes on the performance of restoration is conducted as that in Case Study I. We randomly generate 100 samples of twelve, eighteen, twenty-four, thirty and thirty-six nodes as MER connection nodes, and then calculate their average total load shed. The results are listed in Table 4.4. It can be seen that a large number of MER connection nodes can result in a lower average total load shed. However, a larger number of MER connection nodes does not guarantee a lower total load shed. For examples, in Table 4.4, the minimum total load shed achieved by the samples of twenty-four MER connection nodes is 647.5kW, whereas the maximum total load shed achieved by the samples of thirty MER connection nodes, which is 995.8kW, is even higher than the former. It implies that not only the number of MER connection nodes is relevant, but the locations of these nodes is also important. A large number of MER connection nodes with randomly generated locations can deteriorate the efficiency of MERs in restoration. In this sense, the optimal locations of MER connection nodes needs further investigation, especially when considering the randomness of natural disasters. We will left this for future work.

Moreover, to further demonstrate the advantage of the proposed dynamic MG formation approach in the application of large-scale MER deployment, we make comparisons between the proposed approach and the MG formation approaches in [68, 74, 75]. The comparisons are conducted in terms of the number of MER connection nodes. We randomly generate 50 samples of twelve, twenty-four, thirty-six, and forty-eight nodes being MER connection nodes, and then we implement the proposed approach and the approaches in [68, 74, 75]. The results are listed in Table 4.5. We can see that the proposed dynamic MG formation approach always consumes the least computational time. Specifically, when the number of MER connection nodes is smaller, the proposed approach not differs significantly from the existing approaches. Yet, along with this number getting larger, the solutions can still be determined by our proposed approach within several minutes, whereas the others can take much more time. Because the computational time is a part of the response time to the outages, the proposed MG formation approach with an improved computational efficiency is more applicable in practice, especially in terms of large-scale MER deployment in PDSs.

4.5.3 Case Study III: IEEE 8500-Node Test Feeder

In this subsection, we further validate the advantage of the proposed MG formation approach in large-scale MER deployment compared with other approaches based on the modified IEEE 8500-Node Test Feeder. The primary network of this feeder

Table 4.4: Comparisons of MER Connection Nodes for Case II

Load Shed	Number of MER Connection Nodes			
	18	24	30	36
Min.	691.3kW	647.5kW	622.3kW	601.8kW
Avg.	876.7kW	817.4kW	750.1kW	711.6kW
Max.	1502.8kW	1243.2kW	995.8kW	927.1kW

Table 4.5: Computational Comparison of IEEE 123-Node Test Feeder

Average Comput. Time	Number of MER Connection Nodes			
	12	24	36	48
Ref. [68]	291.44s	753.24s	1681.79s	3112.28s
Ref. [74]	251.03s	623.31s	1140.45s	2518.09s
Ref. [75]	225.51s	521.89s	922.64s	2257.83s
Proposed	177.13s	192.66s	230.43s	261.90s

contains 2,469 nodes with a total load demand of $10,773$kW. Following the work in [142], a network with a reduced size with 1,150 nodes is generated. The network parameters can be found in [142]. There are six master MERs with generation capacity $\overline{P}_k^{ms}$=1,720kW and $\overline{Q}_k^{ms}$=1,370kVar, and ten slave MERs with generation capacity $\overline{P}_z^{sl}$=250kW and $\overline{Q}_z^{sl}$=170kVar are available. A total of fifteen damaged DLs are randomly generated. In addition, a time limitation of 2 hours is set for the Gurobi solver. It means that the optimization will be terminated when time runs out. Fig. 4.8 shows the results of MG formation when there exist 24 MER connection nodes. We can see that six microgrids are established with a total restored load of 8278.59kW. In addition, the same evaluation of the impact of the number of MER connection nodes on the performance of restoration is conducted as that in Case Studies I and II. We randomly generate 15 samples of twelve, twenty-four, thirty-six and forty-eight nodes as MER connection nodes, and then calculate their average total load shed. From Table 4.6, it is clear that along with the increasing of the number of MER connection nodes, our proposed approach can achieve an acceptable computational time, which is around 40.0 minutes. By contrast, the other approaches consume too much computational time. In particular, when the number of MER connection nodes is larger than 24, the computation cannot be completed

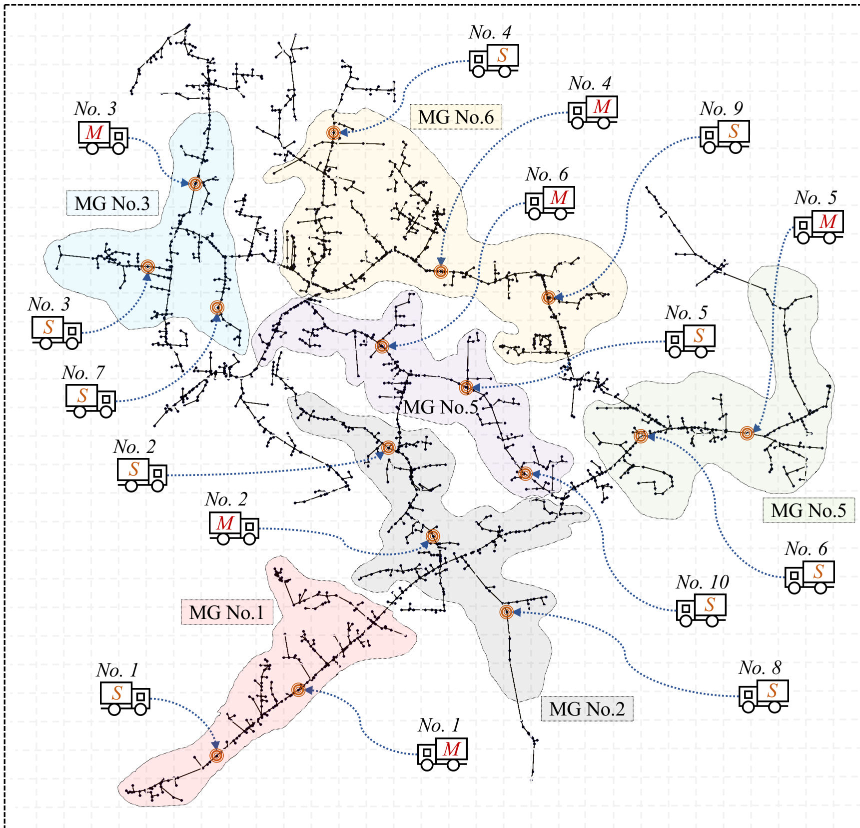

Figure 4.8: Results of IEEE 8500-Node Test Feeder.

within 2.0 hours. These results show that our proposed approach has an obvious advantage in large-scale MER deployment compared with the other approaches, especially in large power distribution networks.

4.6 Summary

In this chapter, a dynamic MG formation approach is proposed for resilient load restoration in PDSs with consideration of large-scale MER deployment. Then, to improve the computational efficiency, an adaptive LinDistflow model is proposed according to the LinDistflow model and the single commodity flow in graph theory. In addition, by incorporating the adaptive LinDistflow model as power flow constraints, a dynamic MG formation problem is formulated as an MINLP problem. Accordingly, a linearization technique is proposed based on the propositional logic constraints. Compared to the existing MG formation approaches based on the LinDistflow model, the proposed one can achieve a reduced number of vari-

Table 4.6: Computational Comparison of IEEE 8500-Node Test Feeder

Average Comput. Time	Number of MER Connection Nodes			
	12	24	36	48
Ref. [68]	116.4min	> 2.0h	> 2.0h	> 2.0h
Ref. [74]	103.5min	> 2.0h	> 2.0h	> 2.0h
Ref. [75]	67.9min	> 2.0h	> 2.0h	> 2.0h
Proposed	33.8min	39.5min	43.2min	47.1min

ables and constraints and computational complexity. Moreover, the effectiveness of the proposed dynamic MG formation approach is demonstrated based on the IEEE 37-Node, IEEE 123-Node and IEEE 8500-Node Test Feeders. It shows that the large-scale MER deployment can result in a lower average total load shed.

Chapter 5

Stochastic Sequential Restoration for Resilient Cyber-Physical PDSs

In this research, we propose a stochastic sequential restoration scheme for CPDSs considering resilience. The sequential restoration problem is formulated as a UMDP with hurricanes incorporated as natural disasters. Different wind velocities and directions are considered as hurricane scenarios, which are used to obtain the fragility of distribution lines. The fragility functions are further used for the derivation of uncertain state transition functions of the UMDP. The minimax regret optimization considering the sample weights of UMDP is presented. The robust sequential actions are determined, such that the loads can be restored in a timely manner. To improve computational efficiency, a minimax regret policy iteration algorithm is presented based on the regret Bellman equation. Case studies are conducted based on the IEEE 123-Node Test Feeder and historical data of Hurricane Bonnie to demonstrate the effectiveness of the proposed scheme.

5.1 System Model

In this section, the cyber-physical distribution system model and the stochastic hurricane damage model are presented.

5.1.1 Cyber-Physical Distribution System Model

In this research, the CPDS is considered as a graph represented by $\mathcal{G} = (\mathbb{N}, \mathbb{L})$, where $\mathbb{N}$ is the set of electrical nodes, and $\mathbb{L}$ is the set of DLs. A set of nodes

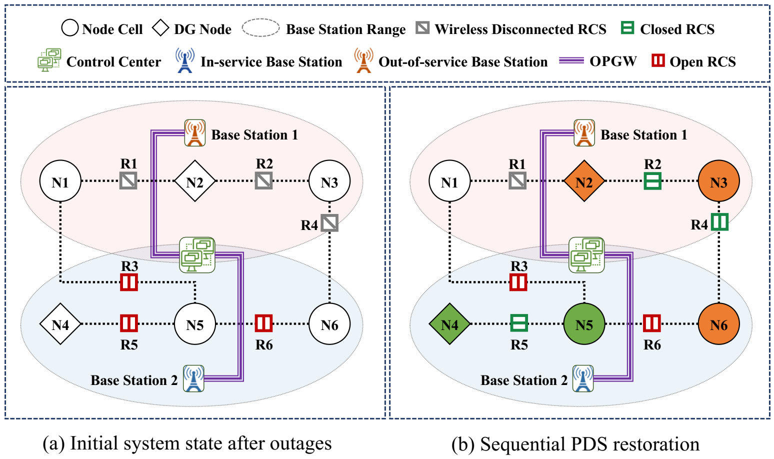

Figure 5.1: An illustration of cyber-physical distribution system model.

$\mathbb{G} \subset \mathbb{N}$ are selected as the locations where DGs are deployed. The DLs are classified into non-switchable lines and switchable lines according to the installation of RCSs. Also, following the works in [62], the concept of node cell is adopted. It is defined as "a set of nodes that are directly interconnected by non-switchable lines without being able to be sectionalized by RCSs". Note that it is assumed that RCSs are integrated with feeder terminal units (FTUs), which can be used to communicate with base stations through wireless links. Without loss of generality, an example can be given in Fig. 5.1(a), which is a CPDS containing six node cells, six RCSs, one control center and two base stations. Note that a base station can cover several RCSs through wireless links. For example, as shown in Fig. 5.1(a), RCSs $(N1, N5)$, $(N4, N5)$ and $(N5, N6)$ are under the range of base station 2. If the OPGW between the control center and one base station is damaged, then all the wireless links of the RCSs under this base station will be disconnected. Hence, in this research, a wirelessly connected or disconnected RCS is referring to whether the wireless link is operational or not. If not, the RCSs can only be manually operated by crews in the field without being controlled remotely.

When outages occur, the system operator will sequentially restore loads utilizing RCSs and DGs. Specifically, commands will be sent from the control center to the wirelessly connected RCSs for remote operation, and crews will be dispatched to operate the wirelessly disconnected RCSs manually. Initially, the system is in a state with all the node cells unserved. Next, every time when taking actions on RCSs, a new state will be observed by the system operator. This research aims to determine the optimal RCS operation in each state, which can guide the system operator to restore the loads as fast as possible. Fig. 5.1(b) shows an illustration of the sequential restoration. After several steps of RCS operations, a new system state is observed by the system operator with RCSs $(N2, N3)$, $(N3, N6)$ and $(N4, N5)$ closed. Then, node cells N3 and N6 can be powered by DG at N2, and node cell N5 can be supplied by DG at N4. For a specific state, since the network topology is given, which is dependent on the status of RCSs and node cells, the real and reactive power flows, and the nodal voltages can be calculated based on the linearized DistFlow model as follows [68]

$$F^p_{mg} = u_{mg} D^p_m + \sum_h F^p_{hg}, \forall m \in \mathbb{N}, h \in \mathbb{N}_{ch}(m), \tag{5.1}$$

$$F^q_{mg} = u_{mg} D^q_m + \sum_h F^q_{hg}, \forall m \in \mathbb{N}, h \in \mathbb{N}_{ch}(m), \tag{5.2}$$

$$v_{mg} - v_{hg} = r_{mh} F^p_{mg} + x_{mh} F^q_{mg}, \forall m \in \mathbb{N}, h \in \mathbb{N}_{ch}(m), \tag{5.3}$$

where u_{mg} denotes the restoration status of node $m \in \mathbb{N}$ with respect to DG at node $g \in \mathbb{G}$. If $u_{mg} = 1$, it means node m is restored by DG at node g, and vice versa. Also, in equation (5.3), the reference voltage is selected as 1 p.u. In addition, the the total weighted load shed $(\mathcal{S})$ can be calculated as

$$\mathcal{S} = \sum_{m \in \mathbb{N}} \sum_{g \in \mathbb{G}} (1 - u_{mg}) w_m D^p_m. \tag{5.4}$$

where w_m denotes load weight. Note that u_{mg} changes with the status of RCSs, hence the operation of RCSs can result in different total restored load. Also, the total weighted load shed $\mathcal{S}$ will be included into the cost function in Section 5.2. Then, shedding critical loads can lead to a higher cost, which will not be preferred. Accordingly, critical loads will be prioritized in terms of restoration.

5.1.2 Stochastic Hurricane Damage Model

Since a node cell is composed of a set of nodes connected via DLs, the fragility of a node cell can be obtained based on the fragility of DLs within the node cell, given by

$$P_i^n(\omega) = 1 - \prod\nolimits_{(m,h)\in\mathbb{L}_i}(1 - P_{mh}^l(\psi_\omega, \theta_\omega)) \tag{5.5}$$

where $P_{mh}^l(\psi_\omega, \theta_\omega)$ is the failure probability of DL (m, h) under wind velocity ψ_ω and wind direction θ_ω. Equation (5.5) means that a single damaged DL can make the node cell unable to be energized. In addition, a DL refers to the line between two nodes, which is normally composed of several conductors and poles [143]. Also, a conductor can be deemed as a segment of a DL between two poles. It means the fragility of a DL is associated with the fragility of poles and conductors, given by

$$\begin{aligned} P_{mh}^l(\psi_\omega, \theta_w) =& 1 - \prod\nolimits_{b\in\mathbb{P}_{mh}}(1 - P_b^p(\psi_\omega)) \\ & \prod\nolimits_{d\in\mathbb{C}_{mh}}(1 - P_d^c(\psi_\omega, \theta_w)), \end{aligned} \tag{5.6}$$

where $P_b^p(\psi_\omega)$ and $P_d^c(\psi_\omega, \theta_w)$ are the failure probability of pole b supporting DL (m, h) and the failure probability of conductor d of DL (m, h), respectively. Moreover, the fragility of pole $b \in \mathbb{P}_{mh}$ can be modeled as a lognormal cumulative distribution function, given by [144]

$$P_b^p(\psi_\omega) = \Phi[\ln(\psi_\omega/m_b)/\zeta_b] \tag{5.7}$$

where m_b is the median of the structural capacity, and ζ_b is the logarithmic standard deviation of intensity measure, which varies with different types of poles. Furthermore, the damages of conductors can be induced by fallen trees during hurricanes, while the probability of a tree falling on conductor $d \in \mathbb{C}_{mh}$ is related to not only wind speed but also wind direction [145]. Hence, the fragility of conductor $d \in \mathbb{C}_{mh}$ can be given by

$$P_d^c(\psi_\omega, \theta_w) = 1 - \prod\nolimits_{z\in\mathbb{T}_d}(1 - P_z^{ct}(\psi_\omega, \theta_w)) \tag{5.8}$$

$$P_z^{ct}(\psi_\omega, \theta_w) = \min\{((\theta_z^b - |\theta_z^p - \theta_w|)/\theta_z^b)P_z^t(\psi_\omega), 0\} \tag{5.9}$$

where $P_z^{ct}(\psi_\omega, \theta_w)$ is the failure probability of conductor d caused by tree z. Also, θ_z^b is the bound angle of tree z falling on conductor c with respect to the direction perpendicular to conductor c, and θ_z^p is the angle of tree z falling perpendicular to conductor d, as shown in Fig. 5.2. In other words, the failure probability of conductor d caused by tree z will reach the maximum value when the tree falls

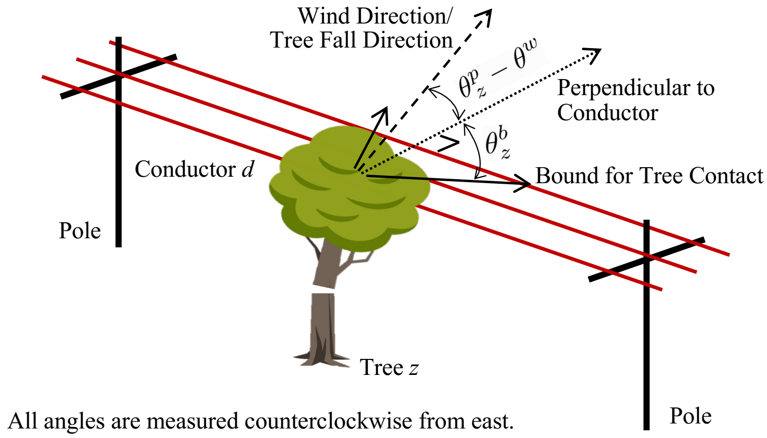

Figure 5.2: An illustration of fallen trees contacting conductors.

perpendicularly on the conductor, i.e., $P_z^{ct}(\psi_\omega, \theta_w) = P_z^t(\psi_\omega)$, and will be reduced to 0 when the tree can not contact the conductor, i.e., $(\theta_z^b - |\theta_z^p - \theta_w|)/\theta_z^b \leq 0$. Moreover, $P_z^t(\psi_\omega)$ represents the failure probability of tree $z \in \mathbb{T}_d$, which can be stated as [146]

$$P_z^t(\psi_\omega) = \frac{\exp[\tau_1 + \tau_3(\psi_\omega/\psi_m)H^{\tau_2}]}{1 + \exp[\tau_1 + \tau_3(\psi_\omega/\psi_m)H^{\tau_2}]} \tag{5.10}$$

where τ_1, τ_2 and τ_3 are tree species parameters, H denotes the diameter at breast height, and ψ_m is the maximum wind speed. In practice, the diameter at breast height H is typically measured at 1.3m above ground using tape measures [147]. Also, the bound angle can be obtained based on the tree height and the perpendicular distance from the tree to the conductor by applying trigonometric principles. And the tree height can be measured using ultrasound hypsometers [148].

5.1.3 Stochastic Manual RCS Operation Model

If damages occur on the OPGW between the control center and one base station after hurricanes, the RCSs covered by such a base station should be operated manually [149]. While, the operation duration is with randomness due to geographic conditions [150]. Thus, the probability of completing the manual operation of a RCS within duration t can be modeled as a normal cumulative distribution function, given by

$$P_{ij}^m(t) = \Phi[(t - \mu_{ij})/\sigma_{ij}] \tag{5.11}$$

where μ_{ij} is the mean of manual operation duration, and σ_{ij} is the standard deviation. Note that unlike the uncertain damages on DLs after hurricanes, the damages of OPGWs can be easily determined by trying communicate with the base station [151]. Hence, the out of connection base stations and their covered RCSs can be observed by the system operator.

5.2 Stochastic Sequential CPDS Restoration Problem Formulation

MDP is a powerful tool for sequential decision making in stochastic dynamic environments. In traditional setup, the policy is evaluated based on state transition functions with certain probabilities. Nevertheless, in many applications, the transition probabilities of an MDP cannot be specified exactly. They are often estimated from collected data or prediction models. This can result in uncertain transition functions, which is referred to as MDP model uncertainty. For example, for hurricanes, different wind velocities ψ_ω and directions θ_ω can produce different hurricane scenarios $(\psi_\omega, \theta_\omega)$. Accordingly, different scenarios can lead to uncertainties in transition functions. In this respect, UMDPs can be utilized to capture the MDP model uncertainty through defining an uncertainty set of transition functions. One transition function is associated with a sample of UMDP [152]. Also, minimax regret optimizations provide a viable solution to obtain robust policies of UMDPs [153]. However, traditional minimax regret optimizations treat transition functions equally, without considering the sample weight. But, in our case, the occurrence of hurricane scenarios can be different. Therefore, equal treatments are not practical. To address the above issues, in this section, we first formulate the stochastic sequential CPDS restoration problem as a UMDP to handle the stochastic nature of hurricanes. Then, we present the minimax regret optimization considering the sample weights of UMDP.

5.2.1 Formulating the Problem as a UMDP

In this research, a UMDP with a tuple $\mathcal{M} = (\boldsymbol{S}, \boldsymbol{A}, \mathcal{T}, \mathcal{C})$ is defined for the stochastic sequential CPDS restoration scheme. In particular, $\boldsymbol{S}$ is the discrete state space,

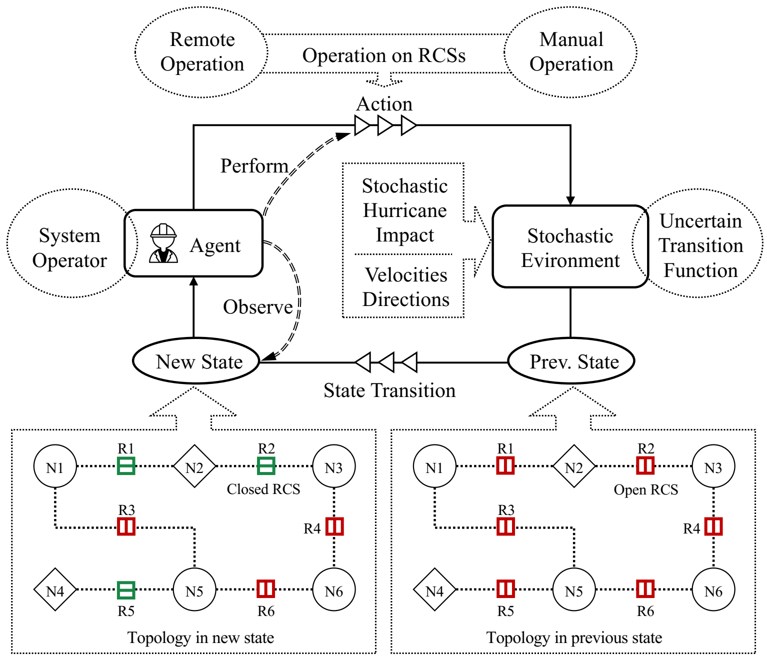

Figure 5.3: An illustration of formulating the problem as a UMDP.

$\boldsymbol{A}$ is the discrete action space, $\mathcal{T}$ denotes a set of transition functions, and $\mathcal{C}$ is the cost function. The uncertainty of a UMDP comes from the uncertainty set $\mathcal{T}$, which is composed of more than one transition function, i.e., $\mathcal{T} = \{T_1, T_2, ..., T_{|\Omega|}\}$. Each function T_ω forms a complete MDP with a tuple $\mathcal{M}' = (\boldsymbol{S}, \boldsymbol{A}, T_\omega, \mathcal{C})$, which is referred to as a sample of UMDP, represented by ω. The problem formulation can be illustrated in Fig. 5.3. It can be considered as an interaction between the system operator and the stochastic environment. Specifically, the system operator will take an action regarding RCS operation in one state. Then, the system will transition into some other state with uncertain transition probabilities resulted by different hurricane scenarios. After that, the system operator will observe the new state, and based on which another action will be taken. The objective is to find the robust policy mapping from states to actions, such that the loads can be restored as fast as possible. Next, we introduce the UMDP for the stochastic sequential CPDS restoration problem in details.

1) State: The state refers to the characteristics of the current environment observed by the system operator. It is denoted by a vector $s \in \boldsymbol{S}$, which contains the status of RCSs and node cells. Herein, we use γ_{ij} to denote the status of RCSs. It can be in open status $\mathcal{O}$, closed status $\mathcal{C}$, unknown status $\mathcal{N}$, and under manual operation status $\mathcal{M}$, i.e., $\gamma_{ij} \in \{\mathcal{O}, \mathcal{C}, \mathcal{N}, \mathcal{M}\}$. The unknown status $\mathcal{N}$ represents that the RCS is wirelessly disconnected. The under manual operation status $\mathcal{M}$ refers to the status of RCSs during manual operation by crew members. Similarly, we use α_i to represent the status of node cells. It can be in intact status $\mathcal{I}$, damaged status $\mathcal{D}$, and uncertain status $\mathcal{U}$, i.e., $\alpha_i \in \{\mathcal{I}, \mathcal{D}, \mathcal{U}\}$. The damaged status means that some damages occur in node cell i. The uncertain status means that the status of node cell i is uncertain to the system operator. Then, the state can be represented by $s = (\gamma_{ij}, \alpha_j)|_{(i,j)\in\mathbb{R}}$. Moreover, at the very beginning of the restoration, the system operator has no information about the damages in the CPDS. Hence, the system is in a specific initial state s_0. In this state, the status of all node cells are uncertain ($\mathcal{U}$), the status of all wirelessly connected RCSs are open ($\mathcal{O}$), and the status of all wirelessly disconnected RCSs are unknown ($\mathcal{N}$).

2) Action: The action is the choice chosen by the system operator based on the current state. It can be denoted by a vector $a \in \boldsymbol{A}$, whose elements are the indices of RCSs that will be operated by the action. Specifically, an action is composed of multiple RCS operations. For example, as shown in Fig. 5.1, one of the feasible actions is $a = \{(N1, N2), (N4, N5)\}$. It implies that RCSs $(N1, N2)$ and $(N4, N5)$ will be under operation. Furthermore, there are two different operations for wirelessly connected and disconnected RCSs. For a wirelessly connected RCS (i, j), the operation refers to remote operation, used to close the RCS remotely. It becomes feasible, when the following conditions hold:

► RCS (i, j) is in the open status, i.e., $\gamma_{ij} = \mathcal{O}$;

► Node cell j is in the uncertain status, i.e., $\alpha_j = \mathcal{U}$;

► RCS (i, j) is connected with a closed status RCS (k, i) on one side, and also connected with an open status RCS (j, k') on the other side, i.e., $\gamma_{ki} = \mathcal{C}$, and $\gamma_{jk'} = \mathcal{O}$. It implies that node cell i is in the intact status, i.e., $\alpha_i = \mathcal{I}$. Note that a DG node is also considered a closed status RCS.

Also, for a wirelessly disconnected RCS (i, j), the operation refers to manual operation, used to dispatch crews to confirm the status of nodel cell j, and manually operate the RCS. The crews in the field will either open the RCS if nodel cell j is damaged, or close the RCS if it is intact. The manual operation becomes feasible, when the following conditions hold:

► RCS (i, j) is in the unknown status, i.e., $\gamma_{ij} = \mathcal{N}$;

► Node cell j is in the uncertain status, i.e., $\alpha_j = \mathcal{U}$;

3) Transition Function Set: In the UMDP, the set of transition functions is composed of multiple transition functions, i.e., $\mathcal{T} = \{T_1, T_2, ..., T_{|\Omega|}\}$. One transition function $T_\omega \in \mathcal{T}$ yields a probability distribution over the next state s', which the system may transition into, when action a is taken in the current state s, i.e., $P_\omega(s'|s, a) = T_\omega(s, a, s')$. Also, a sample of UMDP $\omega \in \Omega$ is considered as a hurricane scenario with specific wind velocities ψ_ω and directions θ_ω. It means that one hurricane scenario $(\psi_\omega, \theta_\omega)$ corresponds to one sample of UMDP ω, and one sample of UMDP is associated with one transition function T_ω. Moreover, since a state is composed of the status of RCSs and node cells, the state transition also means the transitions of RCS and node cell status. Hence, the state transition probability can be derived based on the RCS and the node cell status transition probability, given by

$$P_\omega(s'|s, a) = \prod_{(i,j)\in\mathbb{R}} P_\omega(\gamma'_{ij}, \alpha'_j|\gamma_{ij}, \alpha_j, a) \tag{5.12}$$

where $P_\omega(\gamma'_{ij}, \alpha'_j|\gamma_{ij}, \alpha_j, a)$ is the probability that the status of RCS (i, j) and node cell j transition into γ'_{ij} and α'_j from γ_{ij} and α_j, when taking action a. Furthermore, for RCSs and node cells, the status transition is subject to some constraints, and the status transition probability can be obtained as follows:

► When $\gamma_{ij} = \mathcal{O}$, $\alpha_j = \mathcal{U}$ and $(i, j) \in a$, it means that RCS (i, j) is wirelessly connected, and a remote operation is applied to this RCS. Accordingly, in the next step, one feasible transition is $\gamma'_{ij} = \mathcal{C}$ and $\alpha'_j = \mathcal{I}$. This happens when node cell j is intact, and can be energized. Thus, the status transition probability equals to the node cell intact probability, given by

$$P_\omega(\gamma'_{ij} {=} \mathcal{C}, \alpha'_j {=} \mathcal{I}|\gamma_{ij} {=} \mathcal{O}, \alpha_j {=} \mathcal{U}, a) = (1 - P^n_j(\omega)). \tag{5.13}$$

Another feasible transition is $\gamma'_{ij} = \mathcal{O}$ and $\alpha'_j = \mathcal{D}$. This happens when damages occur in node cell j, and RCS (i,j) is open to isolate the fault. Thus, the status transition probability equals to the node cell damage probability, stated as

$$P_\omega(\gamma'_{ij}{=}\mathcal{O}, \alpha'_j{=}\mathcal{D} | \gamma_{ij}{=}\mathcal{O}, \alpha_j{=}\mathcal{U}, a) = P^n_j(\omega). \tag{5.14}$$

► When $\gamma_{ij} = \mathcal{N}$, $\alpha_j = \mathcal{U}$ and $(i,j) \in a$, it means that RCS (i,j) is wirelessly disconnected, and a manual operation is applied to this RCS. Then, the first feasible transition is $\gamma'_{ij} = \mathcal{C}$ and $\alpha'_j = \mathcal{I}$. This happens when the crews confirm that node cell j is intact, and can be energized by manually closing RCS (i,j). Therefore, the status transition probability equals to the node cell intact probability times the manual operation completion probability, given by

$$P_\omega(\gamma'_{ij}{=}\mathcal{C}, \alpha'_j{=}\mathcal{I} | \gamma_{ij}{=}\mathcal{N}, \alpha_j{=}\mathcal{U}, a){=}(1{-}P^n_j(\omega))P^m_{ij}. \tag{5.15}$$

The status in the next step can also be $\gamma'_{ij} = \mathcal{O}$ and $\alpha'_j = \mathcal{D}$. It happens when the crews confirm that some damages occur in node cell j, and RCS (i,j) should be open. Hence, the status transition probability equals to the node cell failure probability times the manual operation completion probability, given by

$$P_\omega(\gamma'_{ij}{=}\mathcal{O}, \alpha'_j{=}\mathcal{D} | \gamma_{ij}{=}\mathcal{N}, \alpha_j{=}\mathcal{U}, a) = P^\omega_j P^m_{ij}. \tag{5.16}$$

The third feasible transition is $\gamma'_{ij} = \mathcal{M}$ and $\alpha'_j = \mathcal{U}$. It means the crews have not completed the confirmation and manual operation. Thus, the status transition probability equals to the manual operation incompletion probability, given by

$$P_\omega(\gamma'_{ij}{=}\mathcal{M}, \alpha'_j{=}\mathcal{U} | \gamma_{ij}{=}\mathcal{N}, \alpha_j{=}\mathcal{U}, a) = (1 - P^m_{ij}). \tag{5.17}$$

► When $(i,j) \notin a$, it means in the current step no operation is conducted on RCS (i,j). Hence, the status of RCS (i,j) and node cell j remain the same, i.e., $\gamma'_{ij} = \gamma_{ij}$ and $\alpha'_j = \alpha_j$. The status transition probability is given by

$$P_\omega(\gamma'_{ij}{=}\gamma_{ij}, \alpha'_j{=}\alpha_j | \gamma_{ij}, \alpha_j, a) = 1. \tag{5.18}$$

4) Cost Function: The cost function reflects the immediate cost when the system transitions into a state. It is composed of the total load shed cost, and the penalty of voltage and DG capacity violation in state s, given by

$$\mathcal{C}(s) = c_s\mathcal{S}(s) + \lambda_v\mathcal{V}(s) + \lambda_p\mathcal{P}(s) + \lambda_q\mathcal{Q}(s) \tag{5.19}$$

where $\mathcal{S}(s)$ is the total load shed when the system is in state s. Also, $\mathcal{V}(s)$ is the penalty function of voltage, given by

$$\mathcal{V}(s)=\sum_m[\max(0,\sum_g v_{mg}-\overline{v})+\max(0,\underline{v}-\sum_g v_{mg})], \tag{5.20}$$

where $\overline{v}$ and $\underline{v}$ are the upper and lower bounds for voltage, respectively. Similarly, the penalty function of DG generation capacity $\mathcal{P}(s)$ and $\mathcal{Q}(s)$ in state s can be derived as, given by

$$\mathcal{P}(s) = \sum_g[\max(0, \sum_m u_{mg}D_m^p - \overline{P}_g), \tag{5.21}$$

$$\mathcal{Q}(s) = \sum_g[\max(0, \sum_m u_{mg}D_m^q - \overline{Q}_g), \tag{5.22}$$

where $\overline{P}_g$ and $\overline{Q}_g$ denote the upper bounds for the active and reactive capacity of DG located at node g, respectively.

5.2.2 Minimax Regret Optimization in UMDPs

Minimax regret has been considered as an objective to find robust policies in UMDPs [154]. The regret for a fixed policy $\pi \in \Pi$ under a sample of a UMDP $\omega \in \Omega$ can be stated as

$$reg_\omega^\pi(s_0) = V_\omega^\pi(s_0) - V_\omega^{\pi^*}(s_0), \tag{5.23}$$

where $V_\omega^\pi(s)$ is the expected cost of state s when acting under policy π, which can be derived by the Bellman equation as

$$V_\omega^\pi(s) = \mathcal{C}(s) + \gamma \sum_{s' \in \boldsymbol{S}} T_\omega(s,a,s')V_\omega^\pi(s'), \tag{5.24}$$

where $a = \pi(s)$ is the action chosen by policy π in state s. Also, when considering the weight of samples of UMDP (β_ω), equation (5.22) can be rewritten as follows,

$$reg_\omega^\pi(s_0) = \beta_\omega(V_\omega^\pi(s_0) - V_\omega^{\pi^*}(s_0)). \tag{5.25}$$

It means that the regret for π will be scaled by the weight of each sample. For example, the regret for the sample with lower weight will be scaled down much lower than its original regret, i.e., $(V_\omega^\pi(s_0) - V_\omega^{\pi^*}(s_0))$. In the case of sequential restoration after hurricanes, the data of wind velocity and wind direction, i.e., hurricane scenarios $(\psi_\omega, \theta_\omega)$, can be recorded by weather instruments [155]. Hence, the occurrence of hurricane scenarios can be derived, and be used as the UMDP sample weight (β_ω). Then, the threat of the scenario with lower occurrence should be scaled by lower weight than the one with higher occurrence. Note that if the data are not available, the wind-field model can also be used to predict the wind velocity and wind direction [156]. In addition, π^* is the optimal policy which can achieve the lowest expected cost for every state. In other words, the regret represents the performance gap between a policy π and the optimal policy π^*, measured in a competitive environment. This environment consists of an agent (i.e., system operator) performing actions following policy π, and an adversary (i.e., hurricane damages) responding to the actions by applying the worst-case sample of UMDP. Specifically, the adversary intends to maximize the regret for policy π, using the most adversarial sample of UMDP, given by

$$\max_{\omega\in\Omega} reg_\omega^\pi(s_0). \tag{5.26}$$

The agent aims to search for the optimal minimax regret policy π_{reg}^* that can minimize the maximum regret, given by

$$\text{(P1)}\;\; \pi_{reg}^* = \arg\min_{\pi\in\Pi} \max_{\omega\in\Omega} reg_\omega^\pi(s_0). \tag{5.27}$$

Problem (P1) forms the minimax regret optimization in the UMDP. Based on the above-mentioned discussion, the UMDP sample weight (β_ω) can also be considered as a measure to adjust the attacking level of an adversary sample of UMDP.

5.3 Stochastic Sequential CPDS Restoration Problem Solution

The minimax regret policy in UMDPs can be exactly optimized by reformulating problem (P1) as a mixed integer linear programming (MILP) problem [157]. However, this approach scales poorly with respect to the number of state-action pairs. To this end, an approximate solution is proposed to optimize the minimax regret policy in a recursive manner. The solution procedure is shown in Fig. 5.4. First, a regret Bellman equation is presented to calculate the regret considering the sample weights of UMDP through dynamic programming. Second, the uncertainty dependencies over state-action pairs are decoupled by allowing the transition probabilities of two adjacent state-actions being obtained from different samples of UMDP. This

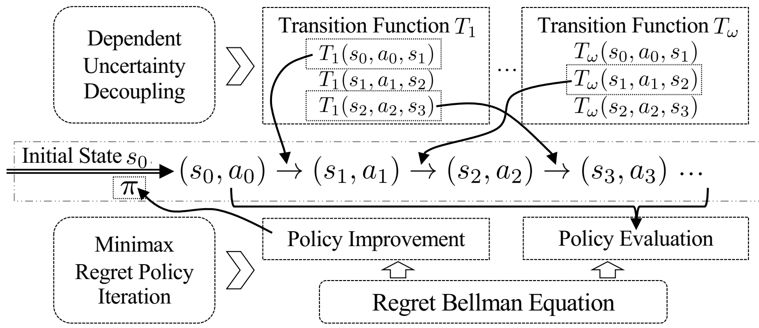

Figure 5.4: An illustration of the proposed approximate solution procedure.

can transform problem (P1) into a stochastic game between an agent and a single-step adversary. At last, a minimax regret policy iteration algorithm is presented to optimize the minimax regret policy iteratively. In the rest of this section, the solution is introduced in details.

5.3.1 Exact Solution via Mixed Integer Linear Programming

The minimax regret policy can be exactly optimized through solving problem (P1) using MILP as follows [157],

$$\text{(P2)} \quad \min_{\hat{\boldsymbol{\pi}}} \mathcal{R}(s_0) \tag{5.28}$$

$$\text{s.t. } \mathcal{R}(s_0) \geq \beta_\omega (V_\omega^{\hat{\boldsymbol{\pi}}}(s_0) - V_\omega^{\hat{\boldsymbol{\pi}}^*}(s_0)), \forall \omega \in \Omega \tag{5.29}$$

$$V_\omega^{\hat{\boldsymbol{\pi}}}(s) = \mathcal{C}(s) + \gamma \textstyle\sum_{s' \in \boldsymbol{S}} T_\omega(s, a, s') V_\omega^{\hat{\boldsymbol{\pi}}}(s'), \forall s, a, \omega \tag{5.30}$$

$$\textstyle\sum_{a \in \boldsymbol{A}} \hat{\pi}_{sa} = 1, \forall s, \tag{5.31}$$

where $\mathcal{R}$ is an auxiliary variable for the regret optimization, hence we have $\mathcal{R}(s_0) = \min_{\pi \in \Pi} \max_{\omega \in \Omega} reg_\omega^\pi(s_0)$ when the reget is optimized. Constraint (5.29) means that $\mathcal{R}(s_0)$ should be greater than the regret under any samples of the UMDP. Constraint (5.30) calculates the expected cost. Constraint (5.31) means that the system operator can choose one single action in each state, which corresponds to the deterministic policy. Note that $\hat{\boldsymbol{\pi}}$ is the vector of $\hat{\pi}_{sa}$, which is a binary variable. If $\hat{\pi}_{sa} = 1$, we have $a = \pi(s)$. In other words, $\hat{\boldsymbol{\pi}}$ can be considered as the auxiliary variables for policy π in the MILP. Furthermore, as MILP problems are NP-Hard, problem (P2) cannot be solved in polynomial time. It means that computing the minimax regret policy exactly via MILPs is only feasible for small UMDPs. For example, the branch and bound (B&B) algorithm is widely used in solving MILPs. However, in our problem, the computational complexity is $\mathcal{O}(2^{|\boldsymbol{S}||\boldsymbol{A}|})$, which is exponential with respect to the number of state-action pairs ($|\boldsymbol{S}||\boldsymbol{A}|$). In other words, along with the increasing number of binary variables $\hat{\pi}_{\boldsymbol{sa}}$, the computational burden becomes heavier. Thus, using MILP to solve the problem scales poorly with respect to the number of state-action pairs.

5.3.2 Approximate Solution Based on Regret Bellman Equation

In this subsection, an approximate solution is proposed to optimize the minimax regret policy in a recursive manner with a reduced computational complexity. The approximate solution is developed based on three Theorems. In particular, Theorem 5.1 shows that the regret can be calculated recursively using the regret Bellman equation. Yet, since the transition function set is dependent over state-action pairs, the computational burden is heavier. Accordingly, Theorem 5.2 indicates that after decoupling uncertainty dependencies to reduce the computational complexity, the approximate regret policy is equivalent to the robust policy of robust MDP. Then, the minimax regret policy iteration algorithm can be developed by employing the robust policy iteration algorithm presented in [158]. Lastly, Theorem 5.3 is to demonstrate the convergence of the proposed algorithm. Next, we present the approximate solution in details. We first present the regret Bellman equation to compute the regret for a policy via dynamic programming.

Theorem 1. The regret for a policy $\pi \in \Pi$ under a sample of UMDP $\omega \in \Omega$ can be calculated recursively using the regret Bellman equation as follows,

$$reg_{\omega}^{\pi}(s) = \beta_{\omega} G_{\omega}(s,a) + \gamma \textstyle\sum_{s' \in \boldsymbol{S}} T_{\omega}(s,a,s') reg_{\omega}^{\pi}(s'), \tag{5.32}$$

$$\textit{where} \qquad G_{\omega}(s,a) = Q_{\omega}^{\pi^*}(s,a) - V_{\omega}^{\pi^*}(s) \tag{5.33}$$

$$Q_{\omega}^{\pi^*}(s,a) = \mathcal{C}(s) + \gamma \textstyle\sum_{s' \in \boldsymbol{S}} T_{\omega}(s,a,s') V_{\omega}^{\pi^*}(s'). \tag{5.34}$$

Note that $G_{\omega}(s,a)$ denotes the suboptimality gap attributed to state-action pair (s,a) under a sample of UMDP ω. It is the difference in the value of a state between taking an action a and taking an action following the optimal policy π^*.

Proof: Substituting equation (5.25) into (5.24), we have

$$reg_\omega^\pi(s) = \beta_\omega(\mathcal{C}(s) + \gamma \sum_{s'} T_\omega(s,a,s') V_\omega^\pi(s') - V_\omega^{\pi^*}(s)). \tag{5.35}$$

From equation (5.25), the following equation can be derived

$$\beta_\omega V_\omega^\pi(s) = reg_\omega^\pi(s) + \beta_\omega V_\omega^{\pi^*}(s). \tag{5.36}$$

Then, substituting equation (5.36) into (5.35), we can derive

$$\begin{aligned} reg_\omega^\pi(s) = \beta_\omega \mathcal{C}(s) + \gamma \sum_{s' \in \boldsymbol{S}} T_\omega(s,a,s') \beta_\omega V_\omega^{\pi^*}(s) - \\ \beta_\omega V_\omega^{\pi^*}(s) + \gamma \sum_{s' \in \boldsymbol{S}} T_\omega(s,a,s') reg_\omega^\pi(s), \end{aligned} \tag{5.37}$$

which is equivalent to equation (5.31). □

Because a sample of UMDP $\omega \in \Omega$ is associated with wind velocity ψ_ω and direction θ_w, the transition function set $\mathcal{T}$ is dependent over state-action pairs (s, a). It means that for all the state-action pairs, the transition probabilities $T_\omega(s, a, s')$ should be obtained from the same transition function T_ω with certain ω. Also, the minimax regret policy should be evaluated under one sample of UMDP. Hence, to solve problem (P1) using the regret Bellman equation recursively, we can calculate the regret with respect to any policy and any sample of UMDP using the exhaustive search algorithm. Then, the policy which can minimize the maximum regret is selected as the optimal minimax regret policy π_{reg}^*. The computational complexity is $\mathcal{O}(|\boldsymbol{S}|^{|\boldsymbol{A}|}|\Omega|)$, which is exponential to the action space $\boldsymbol{A}$. To reduce the computational complexity, we can decouple the dependent uncertainties between two adjacent state-action pairs. Specifically, for one state-action pair (s, a) and subsequent state-action pairs (s', a') and (s'', a''), the transition probabilities $T_\omega(s, a, s')$ and $T_{\omega'}(s', a', s'')$ are not limited to be obtained from the same sample of UMDP, i.e., ω can be different from ω'. This uncertainty decoupling can transform problem (P1) into a stochastic game between an agent (system operator), and a single-step adversary (hurricane damages). At each step, the agent chooses an action $a = \pi(s)$ for state s to minimize the regret, whereas the single-step adversary reacts to this action by choosing one sample of UMDP to maximize the regret.

Algorithm 1: Minimax regret policy iteration algorithm

01: Calculate $V_{\omega}^{\pi^*}(s)$ using standard policy iteration, $\forall s, \omega$
02: Initialize $reg^t(s)$, and π randomly
03: $\Delta \leftarrow 2\epsilon$ /* Policy Evaluation */
04: **while** $\Delta \geq \epsilon$ **do**
05: **for** each $s \in \boldsymbol{S}$ **do**
06: $reg^{t+1}(s) \leftarrow \max_{\eta}\{\beta_{\eta} G_{\eta}(s,a) + \gamma \sum_{s'} T_{\eta}(s,a,s') reg^t(s')\}$
07: $\Delta \leftarrow \max(\Delta, |reg^{t+1}(s) - reg^t(s)|)$
08: policy-stable $\leftarrow true$ /* Policy Improvement */
09: **for** each $s \in \boldsymbol{S}$ **do**
11: old-policy $\leftarrow \pi(s)$
12: $\pi(s) \leftarrow \arg\min_{a} \max_{\eta}\{\beta_{\eta} G_{\eta}(s,a) + \gamma \sum_{s'} T_{\eta}(s,a,s') reg_{\eta}^{t+1}(s')\}$
13: **if** old-policy $\neq \pi(s)$ **then** policy-stable $\leftarrow false$
14: **if** policy-stable $= true$ **then** return $\tilde{\pi}_{reg}^* \leftarrow \pi$
15: **else** go to line 03 for policy evaluation

Herein, we use $\eta : \boldsymbol{S} \times \boldsymbol{A} \times \Omega \rightarrow \{0, 1\}$ to denote the single-step adversary mapping. If $\eta(s, a, \omega) = 1$, it means that the single-step adversary chooses the sample of UMDP ω for adversarial reaction on the action taken by the agent. Then, the stochastic game can be stated as

$$\text{(P3)} \;\; \tilde{\pi}_{reg}^* = \arg\min_{\pi \in \Pi} \max_{\eta} reg^{\pi}(s_0). \tag{5.38}$$

where $\tilde{\pi}_{reg}^*$ is the approximate minimax regret policy.

Theorem 2. Finding the approximate regret policy to Problem (P3) is equivalent to finding the robust policy to the robust Markov Decision Process (RMDP) in [159] as follows:

$$\text{(P4)} \;\; \pi_{robust}^* = \arg\min_{\pi \in \Pi} \max_{\eta} V^{\pi}(s_0). \tag{5.39}$$

Proof: Finding the robust policy for problem (P4) can be considered as a stochastic game between an agent who takes an action, and an adversary which responds to the action by applying the worst-case parameters at each step. □

Accordingly, the robust policy iteration algorithm [158] can be extended after modification to determine the approximate regret policy $\tilde{\pi}_{reg}^*$. Specifically, as the regret Bellman equation contains the suboptimality gap term $G(s, a)$, standard policy iteration should be conducted first to obtain the optimal value of each sample of UMDP, i.e., $V_\omega^{\pi^*}(s)$. Herein, we present **Algorithm 1**, which is the minimax regret policy iteration for problem (P3). From lines 04-08, the policy evaluation is conducted to calculate the regret given one specific policy π. From lines 09-14, the policy will be improved by updating the action a for each state s using the regret calculated by lines 04-08. In particular, in line 12, the action a will be selected which can minimize the maximum regret. Moreover, the iteration will continue until the regret and the policy converge.

Theorem 3. The minimax regret policy iteration is guaranteed to converge, since after t iterations, we have

$$|reg^t(s) - reg^\pi(s)| \leq \gamma^t ||reg^0 - reg^\pi||_\infty, \forall s. \tag{5.40}$$

Proof: It can be shown that the regret $reg^t(s)$ converges to $reg^\pi(s)$ as t increases as follows,

$$\begin{aligned}
&\forall s, |reg^{t+1}(s) - reg^\pi(s)| \\
&= |\max_\eta\{\beta_\eta G_\eta(s,a) + \gamma \textstyle\sum_{s'} T_\eta(s,a,s') reg^{t+1}(s')\} \\
&\quad - \max_\eta\{\beta_\eta G_\eta(s,a) + \gamma \textstyle\sum_{s'} T_\eta(s,a,s') reg^\pi(s')\}| \\
&\leq \gamma \max_\eta |\textstyle\sum_{s'} T_\eta(s,a,s')\{reg^t(s') - reg^\pi(s')\}| \\
&\leq \gamma \max_\eta \{\textstyle\sum_{s'} T_\eta(s,a,s') |reg^t(s') - reg^\pi(s')|\} \\
&\leq \gamma ||reg^t - reg^\pi||_\infty \leq \gamma^{t+1} |reg^0 - reg^\pi||_\infty.
\end{aligned} \tag{5.41}$$

Also, we have $\gamma^t \to 0$ when t inceases, hence $reg^t(s) \to reg^\pi(s)$ after t many times of iteration. □

Furthermore, the computational complexity of the minimax regret policy iteration algorithm is reduced to $\mathcal{O}(|\boldsymbol{S}||\boldsymbol{A}||\Omega|)$. Compared with the exponential complexity $\mathcal{O}(2^{|\boldsymbol{S}||\boldsymbol{A}|})$ by using the MILP reformulation, and the exponential complexity $\mathcal{O}(|\boldsymbol{S}|^{|\boldsymbol{A}|}|\Omega|)$ using the exhaustive search algorithm based on the regret Bellman equation, the reduced complexity is linear to the number of state-action pairs $|\boldsymbol{S}||\boldsymbol{A}|$, and the number of samples of UMDP $|\Omega|$. In practice, the number of switches that can be used for sectionalization in a distribution network is not that large, accordingly the number of reasonable network topologies and the number

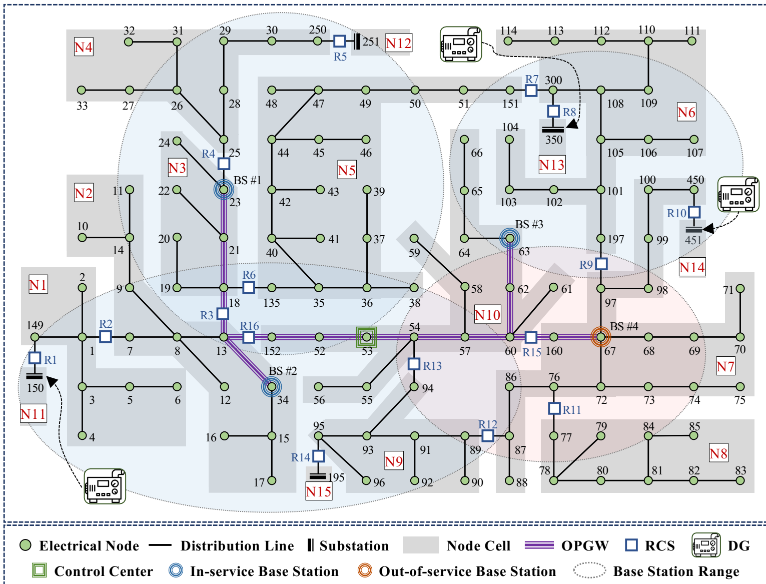

Figure 5.5: An illustration of the modified IEEE 123-Node Test Feeder.

of possible operations on RCSs are limited. Because the states represent network topologies and the actions refer to RCS operations, the number of state-action pairs is also limited. Therefore, the proposed stochastic sequential CPDS restoration scheme can be applicable in realistic distribution systems.

5.4 Case Study

In this section, the test system is set up. The simulation and comparison is conducted based on the IEEE 123-Node Test Feeder and historical data of Hurricane Bonnie.

5.4.1 Test System Setup

To illustrate the effectiveness of the proposed stochastic sequential CPDS restoration scheme, case studies are conducted on a PC with Intel CORE i7-10700 CPU and 8 GB DDR4 RAM. The modified IEEE 123-Node Test Feeder in [62] is adopted as the CPDS, as shown in Fig. 5.5. For the physical layer, there are five substations distributed at nodes 150, 195, 251, 350 and 451, respectively. Also, three DGs are installed at three substation nodes 150, 350 and 451, respectively, with the same generation capacity $\overline{P}_g = 1400$kW and $\overline{Q}_g = 1000$kVar. It means that the restoration can only be performed by using DGs during outages after hurricanes. Also, a

Table 5.1: Hurricane Bonnie Wind Speed and Direction

Sample	1	2	3	4	5
Speed (m/s)	13.9	19.7	27.8	29.3	32.5
Direction (Degree)	67	45	34	65	46
Weight	0.20	0.15	0.15	0.10	0.40

total of sixteen RCSs partition the distribution network into fifteen node cells, as shown in Fig. 5.5. The total load demand is $3,490$kW. For the cyber layer, one control center is located at node 53. It communicates with four base stations from #1 to #4 located at nodes 23, 34, 63 and 67 through the OPGWs, respectively. The base stations, which adopt the IEEE 802.11ah standard (Wi-Fi HaLow), have a link range of 1 km. We want to note that the communication standard is not necessarily to be Wi-Fi. For example, LTE can also utilized to achieve a relatively longer coverage range. Also, it is assumed that the species of trees on the side of DLs are acer rubrum with parameters $\tau_1 = -2.261$, $\tau_2 = 0.426$, and $\tau_3 = 1.140$. The distance from trees to DLs is 5m. The heights of DLs are 10m. The tree heights are randomly generated in $[10, 15]$m. The diameter at breast heights are randomly generated in $[0.4, 0.6]$m. All the trees are planted along the direction of DLs with a spacing of 15m. After hurricanes, the control center cannot communicate with base station #4. Therefore, the RCSs covered only by base station #4, i.e., RCSs R11 and R15, can only be operated manually by crews. Moreover, the historical data of Hurricane Bonnie is adopted to model the hurricane impact [155]. This hurricane made landfalls on the Costa Rica–Nicaragua border, and destructively crossed Nicaragua and Costa Rica from east to west on August 27, 1998, at 04:00 UTC. A total of five hurricane scenarios in terms of wind speed are selected, which are with scales < 15m/s, $15 - 20$m/s, $20 - 25$m/s, $25 - 30$m/s and > 35m/s. The system operator is assumed to make restoration decisions at $22:00$ UTC. Table 5.1 shows the average wind velocity and wind direction of each scenario. The occurrence of each scenario is considered as the UMDP sample weight. Different pairs of wind speeds and wind directions can result in different DL failure probabilities, and then MDP transition functions with respective sample weights.

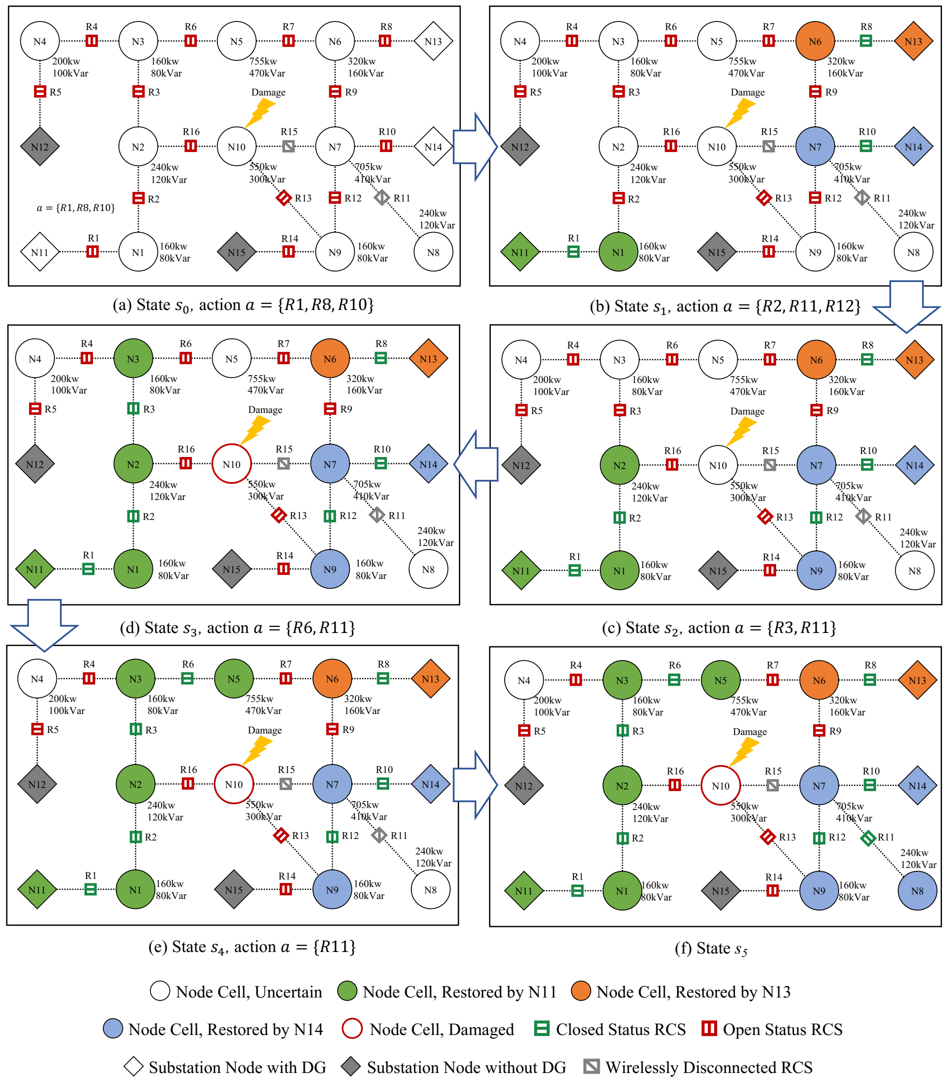

Figure 5.6: An illustration of restored load after state transition following the minimax regret policy.

5.4.2 Simulation Results and Analysis

In this subsection, we take the hurricane damage scenario shown in Fig. 5.6 as an example to illustrate the minimax regret policy. Specifically, in this scenario, some damages occurred in node cell N10 after the hurricane. The main grid is collapsed, which means only the DGs located at nodes 150, 350 and 451 can be utilized for restoration. Note that the system operator has no information on the fault location. All the observation is the current state, which contains the status of RCSs and node cells. Thus, the system operator needs to take actions based on the current state

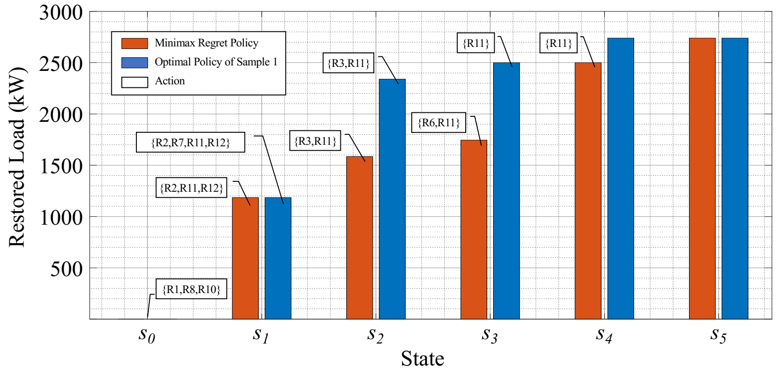

Figure 5.7: Comparison in terms of restored load between the minimax regret policy and the optimal policy of Sample 1.

following the minimax regret policy. The simulation results of the minimax regret policy can be shown in Fig. 5.6. In the initial state s_0, the system operator will operate RCSs R1, R8 and R10. Because there are no damages in node cells N1, N6 and N7, the status of RCSs R1, R8 and R10 will transition into closed status from open status. Then, node cells N1, N6 and N7 can be recognized intact and be energized by DGs at N11, N13 and N14, respectively. In state s_1, the status of RCSs R2 and R12 will transition into closed status by remote operation. The crews will be dispatched to operate wirelessly disconnected RCS R11 manually. Then, the system will transition into state s_2 with node cells N2 and N9 being further restored. In state s_2, when the system operator tried to energize node cell N10, RCS R13 tripped because some damages occurred in N10. Hence, the status of RCS R13 will transition back into open status, and the status of node cell N10 will transition from uncertain status into damaged status. Furthermore, the system operator will close RCS R3 and R6 step by step, such that node cells N3 and N5 can be restored sequentially. Lastly, the system will remain in state s_4 until the manual operation of RCS R11 is completed. Then, the total amount of restored load is $2,740$kW. Note that the system operator will not try to operate RCS R4, because the energization of node cell N4 can induce generation deficiency of DG at node cell N11.

To further illustrate the minimax regret policy, we present the optimal policy π^* of Sample 1 of UMDP, as shown in Fig. 5.7. It can be seen that, under this specific damage scenario, the optimal policy π^* of Sample 1 can achieve a faster restora-

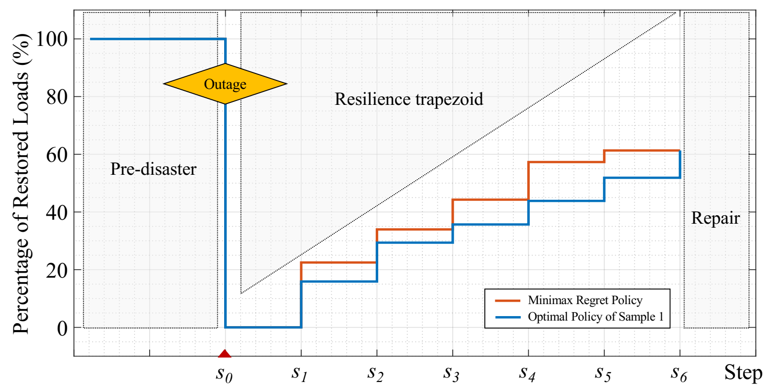

Figure 5.8: Comparison in terms of resilience between the minimax regret policy and the policy of Sample 1.

tion scheme. For example, in state s_2, a total of $2,340$kW of load demand can be restored by the optimal policy, compared with $1,585$kW achieved by the minimax regret policy. The reason is that by following the optimal policy of Sample 1, node cell N5 can be restored as earlier as in state s_2 by taking remote operation on RCS R7 in state s_1. In comparison, the minimax regret policy will not obtain the same amount of restored load until the system transitions into state s_5. However, the optimal policy of a specific sample is not robust in dealing with MDP model uncertainties. In other words, because the wind velocity and wind direction of hurricanes can change, its impact on CPDSs can be various and uncertain to the system operator. For example, the optimal policy of Sample 1 is not the optimal policy of Sample 4, because node cell N6 is very likely to experience damages. Accordingly, restoring node cell N5 by DGs at N13 following the optimal policy of Sample 1 is very risky for Sample 4. In this sense, the minimax regret policy is adopted as a robust solution. It represents the best action that the system operator can conduct step by step considering the worst-case attack from different hurricane scenarios. Also, the minimax regret policy can achieve a higher resilience in terms of restoration. Herein, we randomly generated 5,000 damage scenarios and adopt the resilience metric in [160] for resilience evaluation. The comparison between the average restored loads of the minimax regret policy and the optimal policy of Sample 1 is shown in Fig. 5.8. From the resilience trapezoid, we can observe that the minimax regret policy of UMDP can achieve a faster restoration. It demonstrates that the proposed restoration scheme can effectively enhance the system resilience.

Another feature is that the computational time of the minimax regret policy using the proposed approximate solution is 173.4s. However, the computational time using the exhaustive search based on the regret Bellman equation is 728.9s, and that using the MILP reformulation failed to obtain a solution within a time limit of $1,800$s. This feature is critical for restoration decision making since a prompt response is necessary during outages. Also, the computational time reduction validates the efficiency of the approximate solution. To further validate the expected performance of the minimax regret policy, we perform the proposed stochastic sequential CPDS restoration scheme on $5,000$ randomly generated damage scenarios. The results show that by considering MDP model uncertainties using minimax regret optimization, the restoration can speed up by 13.3% on average over the optimal policy of samples of UMDP. It means that considering the stochastic nature of hurricanes in terms of wind speeds and directions, the minimax regret policy of UMDP can be more robust compared with the optimal policy of traditional MDP.

5.4.3 Comparative Studies and Analysis

To evaluate the performance regarding uncertain damages and communication interruption resulted from cyber-physical interdependence, we compare the following schemes:

1. Proposed scheme considering both uncertain damages and communication interruption;
2. Scheme in [88] considering uncertain damages without communication interruption;
3. Scheme in [62] without considering uncertain damages and communication interruption.

The comparison is based on 50 randomly generated damage scenarios. The results are listed in Table 5.2. It can be observed that Scheme 3 behaves the worst with

Table 5.2: Results of Comparative Studies of Different Schemes

	Scheme 1	Scheme 2	Scheme 3
Avg. Restored Load	2,985kW	2,540kW	1,950kW
DG Utilization Rate	71.1%	60.5%	46.4%

only $1,950$kW average restored load and 46.4% DG utilization rate. The reason is that the deterministic approach obtains the restoration scheme requiring explicit damage information. Hence, any unknown damages can interrupt the sequential restoration as scheduled. Also, by considering uncertain damages, the restoration performance can be improved. For example, the average restored load and the DG utilization rate are increased to $2,540$kW and 60.5%, respectively, by using Scheme 2. However, because of ignoring communication interruption, Scheme 2 can not obtain the best solution. In other words, the sequential restoration will be interrupted when operating the wirelessly disconnected RCSs. By contrast, Scheme 1, which is the proposed scheme, can achieve the highest amount of average restored load with $2,985$kW, and the DG utilization rate can be further increased to 71.1%. This is benefited from considering both uncertain damages and communication interruption of CPDSs.

5.5 Summary

In this chapter, we propose a stochastic sequential restoration scheme based on UMDPs. The cyber-physical interdependent impact, including uncertain damages and communication interruption are considered via transition probabilities. Different wind velocities and wind directions are incorporated as hurricane scenarios to model the uncertain state transition functions of UMDP. The minimax regret optimization considering the sample weights of UMDP is presented to obtain the robust sequential restoration actions. A minimax regret policy iteration algorithm is presented based on the regret Bellman equation to reduce the computational complexity. Case studies show that the performance of restoration can be improved by considering both uncertain damages and communication interruption.

Chapter 6

Conclusions and Future Works

In the 21st century, climate change has emerged as an urgent global concern, unleashing a cascade of environmental variations that escalate the frequency and severity of natural disasters. Consequently, power grids are facing significant challenges in terms of stability and reliability. For example, the continuing rises in global temperatures can bring about devastating storms and wildfires, which can significantly damage electrical infrastructures, interrupt power services and cause substantial economic losses. This spotlights the critical need for power grid resilience, which is defined as the ability to withstand and recover from disruptions. Then, how to effectively enhance grid resilience to alleviate the impact of natural disasters becomes a topical issue in both industry and academia. On the other hand, smart grids represent a modernized electrical infrastructure that leverages advanced communication, control, and monitoring technologies. Unlike traditional grids, smart grids enable bidirectional communications between utilities and consumers, facilitating real-time data exchange and intelligent decision-making. Also, through the deployment of sensors, smart meters, and automation systems, utilities can gain insights into grid conditions, optimize resource allocation, and reconfigure network topologies, and respond rapidly to disruptions. Therefore, smart grid allows for enhanced grid management, improved efficiency, and increased reliability, laying the foundation for resilient power systems. However, one of the greatest challenges is the effective integration and utilization of emerging smart devices, such as DERs, MERs and IEDs, in a resilience-oriented framework. In particular, the inherent randomness of natural disasters can complicate this task, which demands systematic research for a better utilization of smart devices in respond to natural disasters.

To achieve resilience-oriented planning and operation for smart PDSs against natural disasters, stochastic models and the corresponding optimization problems have been investigated in this thesis. Firstly, the stochastic planning of resilient PDSs considering uncertain impacts of earthquakes is investigated. The portfolio of resilient countermeasures including hardening DLs and investing new MEGs and MESSs are addressed through a two-stage stochastic programming problem. The MEG and MESS coordination including co-allocation and energy exchange is incorporated, such that the solution can be more resilient and cost-saving. Secondly, a data-driven PDS resilience enhancement strategy is proposed to deal with post-restoration failures. By employing HHMMs and historical earthquake data, the pre-disaster MEG investment and pre-positioning against multi-shocks, and the post-disaster MEG reallocation and repair scheduling against aftershocks are addressed. Thirdly, a dynamic MG formation approach for large-scale MER deployment is proposed. Through the novel presented adaptive LinDistflow model, the computational efficiency of the MG formation is significantly improved. Last but not least, the problem of sequential load restoration in CPDSs against hurricanes is investigated. By formulating the problem as a UMDP, the cyber-physical interdependent impacts caused by hurricanes is addressed.

6.1 Contributions of Thesis

The main contributions of this thesis can be summarized as follows:

- A stochastic spatial seismic damage model is developed based on the stochastic seismic impact analysis of PDSs. A stochastic resilient PDS planning problem with a bi-level structure is formulated considering coordination between MEGs and MESSs. A solution procedure is proposed to reformulate the problem with $\min\max$ form into a problem with $\min\min$ form and decompose the problem into two subproblems to speed up the computation.

- A RI metric is developed based on HHMM and historical earthquake data to stochastically evaluate restoration path resilience. A data-driven PDS resilience enhancement strategy is proposed for resilient MEG investment, prepositioning and reallocation, and repair scheduling of restoration paths. An iterative algorithm based on linear programming relaxation is proposed to reduce the computational complexity of the repair scheduling problem.

- An adaptive LinDistflow model is proposed based on the LinDistflow model and the single commodity flow in graph theory. A dynamic MG formation problem is proposed considering large-scale deployment of MERs. A linearization technique based on the propositional logic constraints is proposed to address the problem nonlinearity. Computational complexity is analyzed, which shows that the proposed dynamic MG formation approach can improve the computational efficiency without loss of optimality.

- A sequential CPDS restoration scheme is proposed by formulating the problem as a UMDP with uncertain state transition functions. The cyber-physical interdependent impacts are modeled by integrating the hurricane fragility of DLs. To address model uncertainties of a UMDP resulted by various wind velocities and directions with respective occurrence, a minimax regret optimization considering sample weights is presented. An approximate solution based on the regret Bellman equation and the minimax regret policy iteration algorithm is proposed to improve computational efficiency.

6.2 Directions for Future Work

The stochastic resilience-oriented smart PDS planning and operation against natural disasters is a broad research area. Although several critical issues have been addressed in this thesis, there are still many research issues to be investigated. The following topics are proposed for future work:

- For the stochastic planning strategy of resilient PDSs against earthquakes, traditional services provided by MEGs and MESSs can be incorporated into the optimization problem. For examples, MEGs can provide backup capacity during planned maintenance of substations, or be used when a service territory is experiencing a temporary load increase [161]. Also, MESSs can store power during light loading and deliver power back when demand is high for load leveling [162]. In other words, if traditional services provided by MERs can be considered together with the emergency services, the utilization of MERs can be further improved. Advanced algorithms can be developed to improve the computational efficiency of the proposed planning strategy, while taking into account MEG and MESS coordination for cost-saving. In addition, the planning problem for resilient cyber-physical PDSs is still an open issue. However, disasters such as earthquakes can not only damage the physical system for power supply, but also interrupt the communication on the cyber layer. Thus, a planning solution can be more realistic if both cyber and physical conditions are included in the optimization problem.

- The application of the data-driven PDS resilience enhancement strategy against multi-shocks of earthquakes in unbalanced three-phase systems needs further investigation. Moreover, the study of the repair scheduling problem considering stochastic repair time requires future research. In this thesis, the repair time is considered to be deterministic. However, if stochastic repair time can be involved, the performance of the repair process can be potentially improved. In addition, the proposed RI metric is developed based on historical data. However, how to utilize the newly collected data of ongoing multi-shocks of earthquakes to adjust the RI in real time to improve the resilience evaluation performance needs further investigation. The robust anytime learning which allows continuous learning in a changing environment [163] may pave the way for addressing this issue. And we will leave this for future work.

- For the dynamic MG formation approach based on the proposed adaptive LinDistflow model, whether the MG formation based on the current damage information can incorporate the consideration of future potential damage information needs further investigation. To this end, the multi-period distributionally robust optimization in [164] can be employed to include the uncertain future damages using the ambiguity set. Then, the current MG formation solution can be robust to the future damage scenarios. However, this still needs further research. Besides, the application of the proposed dynamic MG formation approach on different natural disasters with randomness still needs to be studied. The proposed approach can be a foundation of MG formation in the resilient planning and operation problem with stochastic analysis. However, the efficiency of problem solving needs further evaluation and advanced algorithms needs to be developed.

- The sequential CPDS restoration scheme can be extended to address other types of natural disasters by incorporating different models. However, the unique damage impact of different natural disasters still needs further investigation. For example, how to consider the stochastic nature of wildfires including the shape of fire flame, wind speed and surface temperature of power lines in a UMDP is still an open issue. Also, the sequential CPDS restoration scheme can be further investigated when renewable energy sources are integrated. Due to the intermittent characteristic of renewable energy output, new strategies should be developed to address the challenges. For example, the uncertainties of wind and solar power can be incorporated into state transition functions. And the robust MDP can be utilized to address uncertainties in model parameters in MDPs. Also, the reinforcement learning can be employed to learn the optimal behavior in this stochastic environment. Another research direction exists in interdisciplinary research involves collaboration and integration of electric systems and transportation systems. Since traffic information may affect crew dispatching, how to incorporate crew routing into the proposed restoration scheme considering cyber-physical interdependent impacts requires further research.

Bibliography

[1] M. Panteli and P. Mancarella, "The grid: Stronger, bigger, smarter?: Presenting a conceptual framework of power system resilience," *IEEE Power and Energy Mag.*, vol. 13, pp. 58–66, Apr. 2015.

[2] J. C. Araneda, H. Rudnick, S. Mocarquer, and P. Miquel, "Lessons from the 2010 Chilean earthquake and its impact on electricity supply," in *Proc. IEEE Powercon'10*, pp. 1–7, 2010.

[3] "Hurricane harvey event analysis report," tech. rep., North American Electric Reliability Corporation, Mar. 2018.

[4] J. W. Busby, K. Baker, M. D. Bazilian, A. Q. Gilbert, E. Grubert, V. Rai, J. D. Rhodes, S. Shidore, C. A. Smith, and M. E. Webber, "Cascading risks: Understanding the 2021 winter blackout in texas," *Energy Res. Social Sci.*, vol. 77, p. 102106, Jul. 2021.

[5] P. Hines, J. Apt, and S. Talukdar, "Large blackouts in north america: Historical trends and policy implications," *Energy Policy*, vol. 37, pp. 5249–5259, Dec. 2009.

[6] H. Brown and S. Suryanarayanan, "A survey seeking a definition of a smart distribution system," in *Proc. IEEE NAPS'09*, pp. 1–7, 2009.

[7] L. Das, S. Munikoti, B. Natarajan, and B. Srinivasan, "Measuring smart grid resilience: Methods, challenges and opportunities," *Renewable Sustainable Energy Rev.*, vol. 130, p. 109918, Sep. 2020.

[8] H. Liang, A. K. Tamang, W. Zhuang, and X. S. Shen, "Stochastic information management in smart grid," *IEEE Commun. Surv. Tutorials*, vol. 16, pp. 1746–1770, Feb. 2014.

[9] G. Popa and C. R. UU, "Resilience and survivability for future networking: framework, mechanisms, and experimental evaluation," tech. rep., 2010.

[10] J. Rak, D. Hutchison, E. Calle, T. Gomes, M. Gunkel, P. Smith, J. Tapolcai, S. Verbrugge, and L. Wosinska, "Recodis: Resilient communication services protecting end-user applications from disaster-based failures," in *Proc. IEEE ICTON'16*, pp. 1–4, 2016.

[11] D. Hutchison and J. P. Sterbenz, "Resilinets: Resilient and survivable networks," *ERCIM NEWS*, no. 77, pp. 30–31, 2009.

[12] B. M. da Rocha Canizes, *Decision support for smart grid planning and operation considering reliability*. PhD thesis, Universidad de Salamanca, 2019.

[13] M. Panteli, D. N. Trakas, P. Mancarella, and N. D. Hatziargyriou, "Power systems resilience assessment: Hardening and smart operational enhancement strategies," *Proc. IEEE*, vol. 105, pp. 1202–1213, May 2017.

[14] Y. Wang, C. Chen, J. Wang, and R. Baldick, "Research on resilience of power systems under natural disasters—A review," *IEEE Trans. Power Syst.*, vol. 31, pp. 1604–1613, May 2015.

[15] B. Li, J. Wei, Y. Liang, and B. Chen, "Optimal placement of fault indicator and sectionalizing switch in distribution networks," *IEEE Access*, vol. 8, pp. 17619–17631, Jan. 2020.

[16] "CAT Natural Gas and Diesel Mobile Generators."

[17] "Generac Diesel and Gaseous Mobile Generators," tech. rep.

[18] "Tecloman mobile energy storage system."

[19] "Conedison transportable energy storage system."

[20] "Volvo 7900 electric bus."

[21] "Alumero mobile solar container."

[22] "Uprise energy portable wind turbine."

[23] J. Landstrom and J. Jewess, "Seismic preparedness strategy," tech. rep., 2019.

[24] A. Kwasinski and A. K. Tang, "Telecommunications performance in the M=9.0 off-shore east coast of Japan earthquake and tsunami, March 11, 2011," in *Proc. International symposium on engineering lessons learned from the 2011 Great East Japan Earthquake*, pp. 1514–1525, 2011.

[25] K. Hirose, J. Reilly, and H. Irie, "The Sendai microgrid operational experience in the aftermath of the Tohoku earthquake: a case study," tech. rep., 2013.

[26] T. Adachi, Y. Ishiyama, Y. Asakura, and K. Nakamura, "The restoration of telecom power damages by the great east japan earthquake," in *Proc. IEEE INTELEC'11*, pp. 1–5, IEEE, Oct. 2011.

[27] "Distribution fault location support tools, algorithms, and implementation approaches," tech. rep., Aug. 2013.

[28] Z. Rafique, H. M. Khalid, and S. Muyeen, "Communication systems in distributed generation: A bibliographical review and frameworks," *IEEE Access*, vol. 8, pp. 207226–207239, Oct. 2020.

[29] S. Espinoza, M. Panteli, P. Mancarella, and H. Rudnick, "Multi-phase assessment and adaptation of power systems resilience to natural hazards," *Electric Power Systems Research*, vol. 136, pp. 352–361, Jul. 2016.

[30] M. Mahzarnia, M. P. Moghaddam, P. T. Baboli, and P. Siano, "A review of the measures to enhance power systems resilience," *IEEE Systems Journal*, vol. 14, pp. 4059–4070, Jan. 2020.

[31] B. Chen, C. Chen, J. Wang, and K. L. Butler-Purry, "Multi-time step service restoration for advanced distribution systems and microgrids," *IEEE Trans. Smart Grid*, vol. 9, pp. 6793–6805, Jul. 2017.

[32] Z. Tan, R. Fan, Y. Liu, and L. Sun, "Microgrid black-start after natural disaster with load restoration using spanning tree search," in *Proc. IEEE PES GM'16*, pp. 1–5, Jul. 2016.

[33] G. N. Ericsson, "Cyber security and power system communication—essential parts of a smart grid infrastructure," *IEEE Trans. Power Delivery*, vol. 25, pp. 1501–1507, Apr. 2010.

[34] C. Konstantinou and O. M. Anubi, “Resilient cyber-physical energy systems using prior information based on gaussian process,” *IEEE Trans. Ind. Inf.*, vol. 18, pp. 2160–2168, Jul. 2021.

[35] “The Smart Grid: An Introduction,” tech. rep.

[36] M. Ahmadi, M. Bahrami, M. Vakilian, and M. Lehtonen, “Application of hardening strategies and dg placement to improve distribution network resilience against earthquakes,” in *Proc. IEEE T&D LA’20*, Nov. 2020.

[37] M. Nazemi, M. Moeini-Aghtaie, M. Fotuhi-Firuzabad, and P. Dehghanian, “Energy storage planning for enhanced resilience of power distribution networks against earthquakes,” *IEEE Trans. Sustainable Energy*, vol. 11, pp. 795–806, Apr. 2019.

[38] M. Rajabzadeh and M. Kalantar, “Improving the resilience of distribution network in coming across seismic damage using mobile battery energy storage system,” *J. Energy Storage*, vol. 52, p. 104891, Aug. 2022.

[39] W. Yuan, J. Wang, F. Qiu, C. Chen, C. Kang, and B. Zeng, “Robust optimization-based resilient distribution network planning against natural disasters,” *IEEE Trans. Smart Grid*, vol. 7, pp. 2817–2826, Jan. 2016.

[40] S. Ma, B. Chen, and Z. Wang, “Resilience enhancement strategy for distribution systems under extreme weather events,” *IEEE Trans. on Smart Grid*, vol. 9, pp. 1442–1451, Jul. 2016.

[41] S. Ma, L. Su, Z. Wang, F. Qiu, and G. Guo, “Resilience enhancement of distribution grids against extreme weather events,” *IEEE Trans. Power Syst.*, vol. 33, pp. 4842–4853, Apr. 2018.

[42] S. Ma, S. Li, Z. Wang, and F. Qiu, “Resilience-oriented design of distribution systems,” *IEEE Trans. Power Syst.*, vol. 34, pp. 2880–2891, Jan. 2019.

[43] G. Zhang, F. Zhang, X. Zhang, Z. Wang, K. Meng, and Z. Y. Dong, “Mobile emergency generator planning in resilient distribution systems: A three-stage stochastic model with nonanticipativity constraints,” *IEEE Trans. on Smart Grid*, vol. 11, pp. 4847–4859, Jun. 2020.

[44] M. Salimi, M.-A. Nasr, S. H. Hosseinian, G. B. Gharehpetian, and

M. Shahidehpour, “Information gap decision theory-based active distribution system planning for resilience enhancement,” *IEEE Trans. on Smart Grid*, vol. 11, pp. 4390–4402, May 2020.

[45] J. Dugan, S. Mohagheghi, and B. Kroposki, “Application of mobile energy storage for enhancing power grid resilience: A review,” *Energies*, vol. 14, p. 6476, Sep. 2021.

[46] D. N. Trakas and N. D. Hatziargyriou, “Optimal distribution system operation for enhancing resilience against wildfires,” *IEEE Trans. Power Syst.*, vol. 33, pp. 2260–2271, Mar. 2017.

[47] N. Bhusal, M. Gautam, and M. Benidris, “Sizing of movable energy resources for service restoration and reliability enhancement,” in *Proc. IEEE PESGM’20*, Aug. 2020.

[48] S. Yao, P. Wang, and T. Zhao, “Transportable energy storage for more resilient distribution systems with multiple microgrids,” *IEEE Trans. Smart Grid*, vol. 10, pp. 3331–3341, Apr. 2018.

[49] M. Nazemi, P. Dehghanian, X. Lu, and C. Chen, “Uncertainty-aware deployment of mobile energy storage systems for distribution grid resilience,” *IEEE Trans. Smart Grid*, vol. 12, pp. 3200–3214, Jul. 2021.

[50] Z. Yang, P. Dehghanian, and M. Nazemi, “Seismic-resilient electric power distribution systems: Harnessing the mobility of power sources,” *IEEE Trans. Ind. Appl.*, vol. 56, pp. 2304–2313, Feb. 2020.

[51] S. Lei, C. Chen, H. Zhou, and Y. Hou, “Routing and scheduling of mobile power sources for distribution system resilience enhancement,” *IEEE Trans. Smart Grid*, vol. 10, pp. 5650–5662, Dec. 2018.

[52] S. Lei, C. Chen, Y. Li, and Y. Hou, “Resilient disaster recovery logistics of distribution systems: Co-optimize service restoration with repair crew and mobile power source dispatch,” *IEEE Trans. Smart Grid*, vol. 10, pp. 6187–6202, Feb. 2019.

[53] Z. Ye, C. Chen, B. Chen, and K. Wu, “Resilient service restoration for unbalanced distribution systems with distributed energy resources by leverag-

ing mobile generators," *IEEE Trans. Ind. Inf.*, vol. 17, pp. 1386–1396, Feb. 2020.

[54] A. K. Erenoğlu and O. Erdinç, "Real-time allocation of multi-mobile resources in integrated distribution and transportation systems for resilient electrical grid," *IEEE Trans. Power Delivery*, vol. 38, pp. 1108–1119, Sep. 2022.

[55] H. Saboori, H. Mehrjerdi, and S. Jadid, "Mobile battery storage modeling and normal-emergency operation in coupled distribution-transportation networks," *IEEE Trans. Sustainable Energy*, vol. 13, pp. 2226–2238, Jul. 2022.

[56] S. Cai, Y. Xie, Q. Wu, X. Jin, M. Zhang, and Z. Xiang, "Two-stage mobile emergency generator dispatch for sequential service restoration of microgrids in extreme conditions," *Int. J. Electr. Power Energy Syst.*, vol. 153, p. 109312, Nov. 2023.

[57] M. Ghasemi, A. Kazemi, E. Bompard, and F. Aminifar, "A two-stage resilience improvement planning for power distribution systems against hurricanes," *Int. J. Electr. Power Energy Syst.*, vol. 132, p. 107214, Nov. 2021.

[58] S. Poudel and A. Dubey, "Critical load restoration using distributed energy resources for resilient power distribution system," *IEEE Trans. Power Syst.*, vol. 34, pp. 52–63, Jul. 2018.

[59] W. Shi, P. Zhuang, and H. Liang, "Mobile energy resource allocation for distribution system resilience against earthquakes," in *Proc. VTC'20-Fall*, pp. 1–5, 2020.

[60] L. Che and M. Shahidehpour, "Adaptive formation of microgrids with mobile emergency resources for critical service restoration in extreme conditions," *IEEE Trans. Power Syst.*, vol. 34, pp. 742–753, Aug. 2018.

[61] S. Yao, P. Wang, X. Liu, H. Zhang, and T. Zhao, "Rolling optimization of mobile energy storage fleets for resilient service restoration," *IEEE Trans. Smart Grid*, vol. 11, pp. 1030–1043, Jun. 2019.

[62] B. Chen, Z. Ye, C. Chen, and J. Wang, "Toward a milp modeling framework for distribution system restoration," *IEEE Trans. Power Syst.*, vol. 34,

pp. 1749–1760, Dec. 2018.

[63] Y. Wang, D. Qiu, F. Teng, and G. Strbac, "Towards microgrid resilience enhancement via mobile power sources and repair crews: A multi-agent reinforcement learning approach," *IEEE Trans. Power Syst.*, Jan. 2023.

[64] K. S. A. Sedzro, X. Shi, A. J. Lamadrid, and L. F. Zuluaga, "A heuristic approach to the post-disturbance and stochastic pre-disturbance microgrid formation problem," *IEEE Trans. Smart Grid*, vol. 10, pp. 5574–5586, Dec. 2018.

[65] M. Zadsar, M. R. Haghifam, and S. M. Miri Larimi, "Approach for self-healing resilient operation of active distribution network with microgrid," *IET Gener. Transm. Distrib.*, vol. 11, pp. 4633–4643, Nov. 2017.

[66] J. Zhao, F. Li, S. Mukherjee, and C. Sticht, "Deep reinforcement learning-based model-free on-line dynamic multi-microgrid formation to enhance resilience," *IEEE Trans. Smart Grid*, vol. 13, pp. 2557–2567, Mar. 2022.

[67] Y. Huang, G. Li, C. Chen, Y. Bian, T. Qian, and Z. Bie, "Resilient distribution networks by microgrid formation using deep reinforcement learning," *IEEE Trans. Smart Grid*, vol. 13, pp. 4918–4930, Jun. 2022.

[68] C. Chen, J. Wang, F. Qiu, and D. Zhao, "Resilient distribution system by microgrids formation after natural disasters," *IEEE Trans. Smart Grid*, vol. 7, pp. 958–966, Jun. 2015.

[69] S. Lei, J. Wang, C. Chen, and Y. Hou, "Mobile emergency generator pre-positioning and real-time allocation for resilient response to natural disasters," *IEEE Trans. Smart Grid*, vol. 9, pp. 2030–2041, Sep. 2016.

[70] S. Cai, Y. Xie, Q. Wu, M. Zhang, X. Jin, and Z. Xiang, "Distributionally robust microgrid formation approach for service restoration under random contingency," *IEEE Trans. Smart Grid*, vol. 12, pp. 4926–4937, Jul. 2021.

[71] M. A. Gilani, A. Kazemi, and M. Ghasemi, "Distribution system resilience enhancement by microgrid formation considering distributed energy resources," *Energy*, vol. 191, p. 116442, Jan. 2020.

[72] K. S. A. Sedzro, A. J. Lamadrid, and L. F. Zuluaga, "Allocation of re-

sources using a microgrid formation approach for resilient electric grids," *IEEE Trans. Power Syst.*, vol. 33, pp. 2633–2643, Aug. 2017.

[73] Y. Shen, T. Qian, W. Li, W. Zhao, W. Tang, X. Chen, and Z. Yu, "Mobile energy storage systems with spatial–temporal flexibility for post-disaster recovery of power distribution systems: A bilevel optimization approach," *Energy*, vol. 282, p. 128300, Nov. 2023.

[74] T. Ding, Y. Lin, G. Li, and Z. Bie, "A new model for resilient distribution systems by microgrids formation," *IEEE Trans. Power Syst.*, vol. 32, pp. 4145–4147, Jan. 2017.

[75] S. Lei, C. Chen, Y. Song, and Y. Hou, "Radiality constraints for resilient reconfiguration of distribution systems: Formulation and application to microgrid formation," *IEEE Trans. Smart Grid*, vol. 11, pp. 3944–3956, Apr. 2020.

[76] T. Ding, Y. Lin, Z. Bie, and C. Chen, "A resilient microgrid formation strategy for load restoration considering master-slave distributed generators and topology reconfiguration," *Appl. Energy*, vol. 199, pp. 205–216, Aug. 2017.

[77] J. Zhu, Y. Yuan, and W. Wang, "An exact microgrid formation model for load restoration in resilient distribution system," *International Journal of Electrical Power & Energy Systems*, vol. 116, p. 105568, Mar. 2020.

[78] L. H. Macedo, G. Muñoz-Delgado, J. Contreras, and R. Romero, "Optimal service restoration in active distribution networks considering microgrid formation and voltage control devices," *IEEE Trans. Ind. Appl.*, vol. 57, pp. 5758–5771, Sep. 2021.

[79] K. Pang, C. Wang, N. D. Hatziargyriou, F. Wen, and Y. Xue, "Formulation of radiality constraintsfor optimal microgrid formation," *IEEE Trans. Power Syst.*, vol. 38, pp. 5341–5355, Nov. 2022.

[80] K. Pang, C. Wang, N. D. Hatziargyriou, and F. Wen, "Microgrid formation and real-time scheduling of active distribution networks considering source-load stochasticity," *IEEE Trans. Power Syst.*, vol. 39, pp. 2801–2813, Nov. 2024.

[81] J. Jian, J. Zhao, H. Ji, L. Bai, J. Xu, P. Li, J. Wu, and C. Wang, “Supply restoration of data centers in flexible distribution networks with spatial-temporal regulation,” *IEEE Trans. on Smart Grid*, vol. 15, pp. 340–354, Jun. 2023.

[82] M. E. Baran and F. F. Wu, “Optimal capacitor placement on radial distribution systems,” *IEEE Trans. Power Delivery*, vol. 4, pp. 725–734, Jan. 1989.

[83] H. Gao, Y. Chen, Y. Xu, and C.-C. Liu, “Resilience-oriented critical load restoration using microgrids in distribution systems,” *IEEE Trans. Smart Grid*, vol. 7, pp. 2837–2848, Apr. 2016.

[84] A. Arif, B. Cui, and Z. Wang, “Switching device-cognizant sequential distribution system restoration,” *IEEE Trans. Power Syst.*, vol. 37, pp. 317–329, Jul. 2021.

[85] Q. Zhang, Z. Ma, Y. Zhu, and Z. Wang, “A two-level simulation-assisted sequential distribution system restoration model with frequency dynamics constraints,” *IEEE Trans. Smart Grid*, vol. 12, pp. 3835–3846, Jun. 2021.

[86] S. Cai, M. Zhang, Y. Xie, Q. Wu, X. Jin, and Z. Xiang, “Hybrid stochastic-robust service restoration for wind power penetrated distribution systems considering subsequent random contingencies,” *IEEE Trans. Smart Grid*, vol. 13, pp. 2859–2872, Mar. 2022.

[87] C. Wang, P. Ju, S. Lei, Z. Wang, F. Wu, and Y. Hou, “Markov decision process-based resilience enhancement for distribution systems: An approximate dynamic programming approach,” *IEEE Trans. Smart Grid*, vol. 11, pp. 2498–2510, Dec. 2019.

[88] E. A. Gol, B. G. Erkal, and M. Göl, “A novel mdp based decision support framework to restore earthquake damaged distribution systems,” in *Proc. ISGT-Europe’19*, pp. 1–5, IEEE, Nov. 2019.

[89] Z. Ye, C. Chen, R. Liu, K. Wu, Z. Bie, G. Lou, W. Gu, and Y. Yuan, “Boost distribution system restoration with emergency communication vehicles considering cyber-physical interdependence,” *IEEE Trans. Smart Grid*, Sep. 2022.

[90] G. Zhang, F. Zhang, X. Zhang, K. Meng, and Z. Y. Dong, "Sequential disaster recovery model for distribution systems with co-optimization of maintenance and restoration crew dispatch," *IEEE Trans. Smart Grid*, vol. 11, pp. 4700–4713, May 2020.

[91] H. Zhang, C. Chen, S. Lei, and Z. Bie, "Resilient distribution system restoration with communication recovery by drone small cells," *IEEE Trans. Smart Grid*, Sep. 2022.

[92] "IEEE 13 node test feeder,"

[93] M. Farivar and S. H. Low, "Branch flow model: Relaxations and convexification—Part I," *IEEE Trans. Power Syst.*, vol. 28, pp. 2554–2564, Apr. 2013.

[94] H.-G. Yeh, D. F. Gayme, and S. H. Low, "Adaptive VAR control for distribution circuits with photovoltaic generators," *IEEE Trans. Power Syst.*, vol. 27, pp. 1656–1663, Dec. 2012.

[95] A. Gholami, F. Aminifar, and M. Shahidehpour, "Front lines against the darkness: Enhancing the resilience of the electricity grid through microgrid facilities," *IEEE Electrif. Mag.*, vol. 4, pp. 18–24, Feb. 2016.

[96] Z. Wang, "Understanding seismic hazard and risk: a gap between engineers and seismologists," in *Proc. 14WCEE*, 2008.

[97] K. W. Campbell, "Near-source attenuation of peak horizontal acceleration," *Bull. Seismol. Soc. Am.*, vol. 71, pp. 2039–2070, Dec. 1981.

[98] C. A. Kircher, R. V. Whitman, and W. T. Holmes, "HAZUS earthquake loss estimation methods," *Nat Hazards Rev*, vol. 7, no. 2, pp. 45–59, 2006.

[99] S. Stein and M. Wysession, *An introduction to seismology, earthquakes, and earth structure*. John Wiley & Sons, 2009.

[100] P. Cui, X.-Q. Chen, Y.-Y. Zhu, F.-H. Su, F.-Q. Wei, Y.-S. Han, H.-J. Liu, and J.-Q. Zhuang, "The Wenchuan earthquake (May 12, 2008), Sichuan province, China, and resulting geohazards," *Nat. Hazard.*, vol. 56, pp. 19–36, Apr. 2011.

[101] D. Lallemant, A. Kiremidjian, and H. Burton, "Statistical procedures for developing earthquake damage fragility curves," *Earthquake Eng. Struct. Dyn.*,

vol. 44, pp. 1373–1389, Jan. 2015.

[102] A. G. Baghmisheh and M. Mahsuli, "Seismic performance and fragility analysis of power distribution concrete poles," *Soil Dyn. Earthquake Eng.*, vol. 150, p. 106909, Nov. 2021.

[103] T. A. Short, *Electric power distribution equipment and systems*. CRC press, 2018.

[104] A. Arab, A. Khodaei, S. K. Khator, K. Ding, V. A. Emesih, and Z. Han, "Stochastic pre-hurricane restoration planning for electric power systems infrastructure," *IEEE Trans. Smart Grid*, vol. 6, pp. 1046–1054, Jan. 2015.

[105] J. Burtscheidt, M. Claus, and S. Dempe, "Risk-averse models in bilevel stochastic linear programming," *SIAM J. Optim.*, vol. 30, pp. 377–406, Feb. 2020.

[106] A. Ruszczyński and A. Shapiro, *Optimization of risk measures*. Springer, 2006.

[107] D. R. Morrison, S. H. Jacobson, J. J. Sauppe, and E. C. Sewell, "Branch-and-bound algorithms: A survey of recent advances in searching, branching, and pruning," *Discrete Optim.*, vol. 19, pp. 79–102, Feb. 2016.

[108] V. D. Blondel, J.-L. Guillaume, R. Lambiotte, and E. Lefebvre, "Fast unfolding of communities in large networks," *J. Stat. Mech: Theory Exp.*, vol. 2008, p. P10008, Oct. 2008.

[109] M. Newman, *Networks*. Oxford University Press, 2018.

[110] L. Dai, C. Chen, and J. Birge, "Convergence properties of two-stage stochastic programming," *Journal of Optimization Theory and Applications*, vol. 106, pp. 489–509, Sep. 2000.

[111] S. Boyd, L. Xiao, A. Mutapcic, and J. Mattingley, *Notes on decomposition methods*. Stanford University, 2008.

[112] Z. Beheshti, S. M. Shamsuddin, and S. Hasan, "Memetic binary particle swarm optimization for discrete optimization problems," *Information Sciences*, vol. 299, pp. 58–84, Apr. 2015.

[113] "GUROBI Optimization,"

[114] R. Bolin and L. Stanford, *The Northridge earthquake: Vulnerability and disaster*. Routledge, 2006.

[115] P.-R. Mincu and T.-A. Boboc, "Load profiles in smart cities," in *Proc. IEEE CIEM'17*, pp. 480–484, Oct. 2017.

[116] "Hardening and resiliency: Us energy industry response to recent hurricane seasons,,"

[117] R. E. Brown, *Electric power distribution reliability*. CRC press, 2017.

[118] O. Schmidt, A. Hawkes, A. Gambhir, and I. Staffell, "The future cost of electrical energy storage based on experience rates," *Nat. Energy*, vol. 2, pp. 1–8, Jul. 2017.

[119] "Generac diesel and gaseous mobile generators,"

[120] M. Wolsink, "Co-production in distributed generation: renewable energy and creating space for fitting infrastructure within landscapes," *Landsc. Res*, vol. 43, pp. 542–561, Sep. 2018.

[121] L. Gan and S. H. Low, "Convex relaxations and linear approximation for optimal power flow in multiphase radial networks," in *IEEE Proc. PSCC'14*, pp. 1–9, IEEE, Aug. 2014.

[122] A. Hayashi, K. Iwata, and N. Suematsu, "Marginalized viterbi algorithm for hierarchical hidden Markov models," *Pattern Recognit*, vol. 46, pp. 3452–3459, Dec. 2013.

[123] "U.S. Geological Survey,"

[124] B. Basciftci, S. Ahmed, and N. Gebraeel, "Adaptive two-stage stochastic programming with an application to capacity expansion planning," *arXiv preprint arXiv:1906.03513*, Jun. 2019.

[125] G. C. Pflug and A. Pichler, *Multistage stochastic optimization*. Springer, 2014.

[126] L. A. Wolsey, "Heuristic analysis, linear programming and branch and bound," in *Combinatorial Optimization II*, pp. 121–134, Springer, 1980.

[127] T. Berthold, *Primal heuristics for mixed integer programs*. PhD thesis, 2006.

[128] L. Bobo, A. Venzke, and S. Chatzivasileiadis, “Second-order cone relaxations of the optimal power flow for active distribution grids: Comparison of methods,” *Int. J. Electr. Power Energy Syst.*, vol. 127, p. 106625, May 2021.

[129] Y. Chen, D. Qi, H. Dong, C. Li, Z. Li, and J. Zhang, “A fdi attack-resilient distributed secondary control strategy for islanded microgrids,” *IEEE Trans. Smart Grid*, vol. 12, pp. 1929–1938, Dec. 2020.

[130] A. Krämer, J. Green, J. Pollard Jr, and S. Tugendreich, “Causal analysis approaches in ingenuity pathway analysis,” *Bioinformatics*, vol. 30, pp. 523–530, Dec. 2013.

[131] Y. Xu, C.-C. Liu, Z. Wang, K. Mo, K. P. Schneider, F. K. Tuffner, and D. T. Ton, “Dgs for service restoration to critical loads in a secondary network,” *IEEE Trans. Smart Grid*, vol. 10, pp. 435–447, Aug. 2017.

[132] F. Zhou and S. H. Low, “A note on branch flow models with line shunts,” *IEEE Trans. Power Syst.*, vol. 36, pp. 537–540, Oct. 2020.

[133] “Chapter 9 optimal trees,” vol. 7, pp. 503–615, 1995.

[134] S. Even, A. Itai, and A. Shamir, “On the complexity of time table and multicommodity flow problems,” in *Proc. IEEE SFCS’75*, pp. 184–193, Jul. 1975.

[135] J. A. Taylor and F. S. Hover, “Convex models of distribution system reconfiguration,” *IEEE Trans. Power Syst.*, vol. 27, pp. 1407–1413, Feb. 2012.

[136] G. Liu, M. S. Chinthavali, N. Stenvig, X. Li, T. Jiang, Y. Zhang, and K. Tomsovic, “Resilient microgrid scheduling considering multi-level load priorities,” in *Proc. IEEE PESGM’20*, pp. 1–5, Aug. 2020.

[137] C. Wu, W. Gu, S. Zhou, and X. Chen, “Coordinated optimal power flow for integrated active distribution network and virtual power plants using decentralized algorithm,” *IEEE Trans. Power Syst.*, vol. 36, pp. 3541–3551, Jan. 2021.

[138] A. Arif, Z. Wang, J. Wang, and C. Chen, “Power distribution system outage management with co-optimization of repairs, reconfiguration, and DG dispatch,” *IEEE Trans. Smart Grid*, vol. 9, pp. 4109–4118, Jan. 2017.

[139] P. K. Polisetty and E. P. Gatzke, “Piecewise linear relaxation techniques for solution of nonconvex nonlinear programming problems,” *J Glob Optim.*, 2005.

[140] E. L. Lawler and D. E. Wood, “Branch-and-bound methods: A survey,” *Oper. Res.*, vol. 14, pp. 699–719, Aug. 1966.

[141] L. Gurobi Optimization, “Gurobi optimizer reference manual,” 2021.

[142] Y. Liu, J. Li, L. Wu, and T. Ortmeyer, “Chordal relaxation based acopf for unbalanced distribution systems with ders and voltage regulation devices,” *IEEE Trans. Power Syst.*, vol. 33, pp. 970–984, May 2017.

[143] M. Ouyang and L. Duenas-Osorio, “Multi-dimensional hurricane resilience assessment of electric power systems,” *Struct. Saf.*, vol. 48, pp. 15–24, May 2014.

[144] A. M. Salman, Y. Li, and M. G. Stewart, “Evaluating system reliability and targeted hardening strategies of power distribution systems subjected to hurricanes,” *Reliab. Eng. Syst. Saf.*, vol. 144, pp. 319–333, Dec. 2015.

[145] Q. Lu and W. Zhang, “An integrated damage modeling and assessment framework for overhead power distribution systems considering tree-failure risks,” *Struct. Infrastruct. Eng.*, pp. 1–16, Mar. 2022.

[146] C. D. Canham, M. J. Papaik, and E. F. Latty, “Interspecific variation in susceptibility to windthrow as a function of tree size and storm severity for northern temperate tree species,” *Can. J. For. Res.*, vol. 31, pp. 1–10, Jan. 2001.

[147] “Diameter at breast height.”

[148] K. Sterenczak, M. Mielcarek, B. Wertz, K. Bronisz, G. Zajkaczkowski, A. M. Jagodzinski, W. Ochal, and M. Skorupski, “Factors influencing the accuracy of ground-based tree-height measurements for major european tree species,” *J. Environ. Manage.*, vol. 231, pp. 1284–1292, Feb. 2019.

[149] M. H. Kapourchali, M. Sepehry, and V. Aravinthan, “Fault detector and switch placement in cyber-enabled power distribution network,” *IEEE Trans. Smart Grid*, vol. 9, pp. 980–992, May 2016.

[150] S. Hunsche, M. T. Zonin, A. P. de Morais, O. C. B. de Araújo, G. C. Junior, A. C. Marchesan, K. T. Martin, E. F. Schneider, and A. S. Bretas, "Service restoration in distribution systems based on multi-objective genetic algorithm considering repair and switching time," in *Proc. ISGT Latin America'19*, pp. 1–6, IEEE, 2019.

[151] Z. Feng and Z. Yuexia, "Study on smart grid communications system based on new generation wireless technology," in *Proc. ICECC'11*, pp. 1673–1678, IEEE, 2011.

[152] A. Ahmed, P. Varakantham, M. Lowalekar, Y. Adulyasak, and P. Jaillet, "Sampling based approaches for minimizing regret in uncertain markov decision processes (mdps)," *JAIR*, vol. 59, pp. 229–264, Jul. 2017.

[153] M. Rigter, B. Lacerda, and N. Hawes, "Minimax regret optimisation for robust planning in uncertain markov decision processes," in *Proc. AAAI'21*, vol. 35, pp. 11930–11938, May 2021.

[154] H. Xu and S. Mannor, "Parametric regret in uncertain markov decision processes," in *Proc. IEEE CDC'09*, pp. 3606–3613, Dec. 2009.

[155] J. L. Schroeder and D. A. Smith, "Hurricane bonnie wind flow characteristics as determined from wemite," *J. Wind Eng. Ind. Aerodyn.*, vol. 91, pp. 767–789, MAY 2003.

[156] P. J. Vickery and L. A. Twisdale, "Wind-field and filling models for hurricane wind-speed predictions," *J. Struct. Eng.*, vol. 121, pp. 1700–1709, Nov. 1995.

[157] A. Ahmed, P. Varakantham, Y. Adulyasak, and P. Jaillet, "Regret based robust solutions for uncertain markov decision processes," *Proc. NeurIPS'13*, vol. 26, 2013.

[158] G. N. Iyengar, "Robust dynamic programming," *Math. Oper. Res.*, vol. 30, pp. 257–280, May 2005.

[159] W. Wiesemann, D. Kuhn, and B. Rustem, "Robust markov decision processes," *Math. Oper. Res.*, vol. 38, pp. 153–183, Nov. 2013.

[160] M. Panteli, P. Mancarella, D. N. Trakas, E. Kyriakides, and N. D. Hatziargyriou, "Metrics and quantification of operational and infrastructure re-

silience in power systems," *IEEE Trans. Power Syst.*, vol. 32, pp. 4732–4742, Feb. 2017.

[161] "Benefits of using mobile transformers and mobile substations for rapidly restoring electrical service," tech. rep., U.S. Department of Energy, 2006.

[162] H. Abdeltawab and Y. A.-R. I. Mohamed, "Mobile energy storage sizing and allocation for multi-services in power distribution systems," *IEEE Access*, vol. 7, pp. 176613–176623, Dec. 2019.

[163] M. Suilen, T. D. Simão, D. Parker, and N. Jansen, "Robust anytime learning of markov decision processes," *Proc. NeurIPS'22*, vol. 35, pp. 28790–28802, Nov. 2022.

[164] Z. Wu and K. Sun, "Distributionally robust optimization with wasserstein metric for multi-period portfolio selection under uncertainty," *Appl. Math. Modell.*, vol. 117, pp. 513–528, May 2023.